https://ntrs.nasa.gov/search.jsp?R=19950016500 2020-06-16T08:05:24+00:00Z

NASA Contractor Report 4649

Euler Technology Assessment Program for Preliminary Aircraft Design Employing SPLITFLOW Code With Cartesian Unstructured Grid Method

Dennis B. Finley
Lockheed Fort Worth Company • Fort Worth, Texas

National Aeronautics and Space Administration
Langley Research Center • Hampton, Virginia 23681-0001

Prepared for Langley Research Center
under Contract NAS1-19000

March 1995

This publication is available from the following sources:

NASA Center for AeroSpace Information
800 Elkridge Landing Road
Linthicum Heights, MD 21090-2934
(301) 621-0390

National Technical Information Service (NTIS)
5285 Port Royal Road
Springfield, VA 22161-2171
(703) 487-4650

Table of Contents

Summary 1

1. Introduction 3

2. General Algorithm Attributes 4
   Code formulation 4
   Surface Representation 4
   Grid Generation 4
   Initial Grid Refinement 5
   Grid Adaption 6
   Numerical Formulation 7
   User Work-load and SPLITFLOW Domain Definition 8

3. Attributes of Grids for Euler Technology Assessment 9

4. Pathfinder Study 11
   Effect of Grid Resolution 11
   Solution timing 12
   Effect of Wind Tunnel Walls 14
   Assessment of Vortex Burst Location 15

5. Solutions from Run Matrix 16
   Baseline Configuration Results 16
   Results for Undeflected Leading Edge 16
   Effect of Tail Placement 17
   Effect of Body Chine Shape 19
   Effect of Sideslip for Twin Tail 19
   Effect of Sideslip for Centerline Tail 21
   Repeatability and 'Accuracy' 21

6. Conclusions 23

7. Acknowledgments 24

References 25

List of Figures

Figure 2.1. SPLITFLOW Grid Topology 28
Figure 2.2. Cell Cutting Process 29
Figure 2.3. SPLITFLOW Adaptive Refinement / Derefinement 30
Figure 2.4. Statistical Grid Adaption Procedure 31
Figure 2.5. SPLITFLOW Grid Generation Sequence 32
Figure 3.1. Surface Grid for SPLITFLOW is Generated using LFWC CAD 33
Figure 3.2 SPLITFLOW Grid Statistics for Cell Size versus Grid Levels 34
Figure 4.1. Grid Refinement Effects at Aoa=10 35
Figure 4.2. Grid Refinement Effects at Aoa=35 36
Figure 4.3. Grid Generation and Adaption Results for Pathfinder Study 37
Figure 4.4. Convergence of Forces 38
Figure 4.5. Convergence of Moments 39
Figure 4.6. Cell Buildup over Course of Run 40
Figure 4.7. CPU Time Requirements During Run 41
Figure 4.8. Pathfinder Grid Resolution 42
Figure 4.9. Use of Total Pressure Defined from X-Crossflow to Define Flowfield 43
Figure 4.10. MTVI Fuselage Cut Geometry at Pressure Stations 44
Figure 4.11. Pathfinder X-Crossflow Total Pressure Comparison 45
Figure 4.12. Pathfinder Vortex Comparison 46
Figure 4.13. Upper-Surface Pattern at Aoa=10 47
Figure 4.14. Upper-Surface Pattern at Aoa=35 48
Figure 4.15. Effect of Grid Resolution on Forebody Pressures for MTVI#1 49
Figure 4.16. Effect of Grid Resolution on Wing Pressures for MTVI#1 50
Figure 4.17. Aerodynamic Coefficients vs Test Data for MTVI#1 51
Figure 4.18. Volume Grid for Free-air and Tunnel Cases 52
Figure 4.19. Effect of Tunnel Walls on Vortical Pattern 53
Figure 4.20. Forebody Pressures for MTVI#1 for Tunnel Wall and Free-Air 54
Figure 4.21. Wing Pressures for MTVI#1 for Tunnel Wall and Free-Air 55
Figure 4.22. Vortex Burst Location for Several Steps of Solution, Aoa=35 56
Figure 4.23. Lift and Pitching Moment for Vortex Burst Case, Aoa=35 57
Figure 5.1. Effect of High AOA on Off-Body Pressure Coefficient 58
Figure 5.2. Forebody Pressures for MTVI#1 With Zero-LEF, Aoa=10 59
Figure 5.3. Wing Pressures for MTVI#1 With Zero-LEF, Aoa=10 60
Figure 5.4. Forebody Pressures for MTVI#1 With Zero-LEF, Aoa=35 61
Figure 5.5. Wing Pressures for MTVI#1 With Zero-LEF, Aoa=35 62
Figure 5.6. Aerodynamic Coefficients vs Test data for Zero-LEF 63
Figure 5.7. Effect of Tail Arrangement on X-Crossflow Total Pressure, Aoa=22.5 64
Figure 5.8. Effect of Tail Arrangement on Flowfield, Aoa=22.5 65
Figure 5.9. Forebody Pressures for Tail Placement, Aoa=10 66
Figure 5.10. Wing Pressures for Tail Placement, Aoa=10 67
Figure 5.11. Forebody Pressures for Tail Placement, Aoa=22.5 68
Figure 5.12. Wing Pressures for Tail Placement, Aoa=22.5 69
Figure 5.13. Effect of Tail Arrangement on Flowfield, Aoa=35 70
Figure 5.14. Forebody Pressures for Tail Placement, Aoa=35 71

Figure 5.15. Wing Pressures for Tail Placement, Aoa=35 72
Figure 5.16. Aerodynamic Coefficients vs Test data for MTVI#2 73
Figure 5.17. Effect of Chine on X-Crossflow Total Pressure, Aoa=22.5 74
Figure 5.18. Effect of Chine on Flowfield, Aoa=22.5 75
Figure 5.19. Forebody Pressures for Chine Shaping, Aoa=22.5 76
Figure 5.20. Wing Pressures for Chine Shaping, Aoa=22.5 77
Figure 5.21. Forebody Pressures for Chine Shaping, Aoa=35 78
Figure 5.22. Wing Pressures for Chine Shaping, Aoa=35 79
Figure 5.23. Aerodynamic Coefficients vs Test data for Sharp 30-Degree Chine 80
Figure 5.24. Effect of Sideslip on X-Crossflow Total Pressure, Twin Tail 81
Figure 5.25. Effect of Sideslip on Vortex Position, Twin Tail 82
Figure 5.26. Forebody Pressures for Twin Tail in Sideslip 83
Figure 5.27. Wing Pressures for Twin Tail in Sideslip 84
Figure 5.28. Comparison of Lateral/Directional Data for Twin Tail, Aoa=22.5 85
Figure 5.29. Comparison of Lateral/Directional Data for Twin Tail, Aoa=30 86
Figure 5.30. Effect of Sideslip on X-Crossflow Total Pressure, Centerline Tail 87
Figure 5.31. Effect of Sideslip on Vortex Position, Centerline Tail 88
Figure 5.32. Forebody Pressures for Centerline Tail in Sideslip 89
Figure 5.33. Wing Pressures for Centerline Tail in Sideslip 90
Figure 5.34. Comparison of Lateral/Directional Data for Centerline Tail, Aoa=30 91
Figure 5.35. Uncertainty in Surface Pressures for Test and CFD 92
Figure 5.36. Uncertainty in Forces for Test and CFD 93

List of Tables

Table 1. Run Matrix for Euler Technology Assessment 26

Euler Technology Assessment Program for Preliminary Aircraft Design Employing SPLITFLOW Code with Cartesian Unstructured Grid Method

Dennis B. Finley
Lockheed Fort Worth Company

Summary

This report documents results from the Euler Technology Assessment program. The objective was to evaluate the efficacy of Euler computational-fluid dynamics codes for use in preliminary design. Both the accuracy of the predictions and the rapidity of calculation were to be assessed. This portion of the study was conducted by Lockheed Fort Worth Company, using a recently-developed in-house Cartesian-grid code called SPLITFLOW (Ref. 1). The Cartesian grid technique offers several advantages for this study, including ease of volume grid generation and reduced number of cells compared to other grid schemes. SPLITFLOW also includes grid adaption of the volume grid during the solution, to resolve high-gradient regions. This proved beneficial in resolving the large vortical structures in the flow for several of the configuration cases. The SPLITFLOW code predictions of configuration forces and moments are shown to be adequate for preliminary design, including predictions of sideslip effects and the effects of geometry variations at low and high angles of attack. The time required to generate the results from initial surface data is on the order of several hours, including grid generation, which is compatible with the needs of the design environment.

1. Introduction

In preliminary aircraft evaluation, a predicted result is valued both for its accuracy and for its timeliness. In order to impact the design process, aerodynamic data must be produced within the constraints of configuration decisions. Recently, the use of computational fluid dynamics codes (CFD) for use in preliminary aircraft external shape evaluation has become practical. CFD calculations provide improved resolution of configuration features over lower-order methods, and the speed of computational hardware has put these codes within reach of the short design cycles typical of advanced aircraft development.

The use of the Euler formulation provides a substantial simplification of the numerical partial differential equations, reduces the size of the grid, and also avoids significant issues regarding turbulence modeling of viscous layers. However, the Euler formulation contains non-physical generation of vorticity (through numerical dissipation) and generally will not capture secondary vortices (Ref. 2). Use of Euler codes on wings and forebodies having rounded leading edges is difficult due to uncertainty in the 'separation' point (Ref. 2).

The creation of the computational grid plays a substantial role in determining the timeliness with which CFD can be used within design evaluations. Grid generation on complex vehicles can take literally months, rendering CFD no more timely than conventional wind tunnel testing. Innovative grid generation techniques are critical to creating time-valued CFD predictions.

The current study was designed to assess the value of Euler analyses and grid generation techniques for configuration predictions, in flow regions both below and above vortex burst. The configurations were all sharp-edge, eliminating the concern for Reynolds number effects on leading edge separation. The use of the Euler equations simplified the grid generation, and provided ease in conducting grid density studies since no special provision had to be made to maintain a certain number of grid points within the boundary layer. High angle of attack predictions did require grid adaption to capture off-body flow structures such as high-vorticity regions. Without grid adaption, the off-body flowfield would be poorly resolved, due to the dissipation in regions where the cell size is high. Several codes were used in the study, and several organizations conducted parallel evaluations. The TEAM code (evaluated by LASC), Ref. 3, is a structured-grid Euler/Navier-Stokes code. The OVERFLOW code (evaluated by Boeing Aerospace), Ref. 4, is a Chimera overset structured-grid Euler/Navier-Stokes code. The USM3D code (evaluated by NASA-Langley), Ref. 5, is an unstructured-grid Euler/Navier-Stokes code which uses tetrahedral cells. The results of these codes for the study are reported in separate documents.

PRECEDING PAGE BLANK NOT FILMED

2. General Algorithm Attributes

Code formulation

Cartesian grid techniques have been developed as a means of fast automatic grid generation (Ref. 6,7). The methods generally utilize recursive cell subdivision to generate the computational mesh around geometries. The grid generation is generally automatic and can handle extremely complex geometries. SPLITFLOW is a finite-volume Euler/Navier-Stokes code which utilizes cubical cells. Attributes of SPLITFLOW include automatic cell division and domain boundary decomposition from a computer-aided design (CAD) surface definition. The code is upwind in the inviscid regions, and flux limiters are available to reduce oscillations near shocks. Inviscid regions utilize Cartesian grid topology, while a prismatic grid generator is used for viscous regions. As shown in Figure 2.1, the Cartesian grid method produces rapid subdivision of root cells, and a known cell aspect ratio for ease of reconstruction of face information. Solution grid adaption is included within the code, using several user-selected functions. The code offers extremely fast user setup times, on the order of 20 to 40 minutes.

Surface Representation

The surface geometry is input as a triangulated surface mesh. This mesh is provided by the engineering computer aided design (CAD) package used to define the configuration. By interfacing with the CAD package directly, conversion of geometry to CFD surface definitions is eliminated. The surface in the CAD file is defined as a list of X, Y, and Z coordinates and a connectivity in the form of three node numbers corresponding to the indices of the forming points of each triangle making up the surface. The geometry facets are oriented such that the surface normal point into the computational domain. Subsets of the facets can be grouped together in a series of ASCII files, so that in the assembly of the faces of the grid described below, each can be associated with a particular boundary condition type such as no-slip, symmetry, characteristic slip wall, etc.

Grid Generation

The construction of the Cartesian grids within SPLITFLOW begins with a boundary face file consisting of triangular facets describing all 6 faces of the grid, including the body surface. For viscous analysis (not included in this report) the prismatic grid generator would be employed to build an initial grid suitable for viscous analysis. The Cartesian grid would then use the outer layer of the prismatic grid as its boundary surface. As shown in Figure 2.2, SPLITFLOW finds the intersection between the Cartesian cells at the boundary and the sur-

face faces, and constructs smaller facets in the intersection plane which are used to reconstruct each cut boundary cell. Thus, the boundary cells contain portions of the surface boundary and inherently capture the surface resolution provided by the user in the boundary face file. The number of subtriangles constructed within each surface facet range on the order of 5 to 10, but all the subtriangles are coplanar with the original facet provided in the face file. Each boundary subtriangle is connected to a unique Cartesian boundary cell. The size of the Cartesian cells, and resulting number of grid levels, is determined by the size of the facets provided in the face file. Some control is provided by setting a scale factor (bndscale) for the facets on each face, and a minimum Cartesian cell length term (dxyzmin), in the input deck.

An octree data structure is used to store information for each Cartesian cell during the recursive grid generation process. A subdivided cell produces eight new offspring cells, as shown in Figure 2.1. The parent is retained in the grid after the subdivision. The information stored for each cell consists of the global index of the parent cell, the global indices of the eight children that may exist and the grid level of the cell. The grid 'level' refers to the number of times the root cell has been recursively subdivided to create this particular child. Since the position of each offspring cell (in relation to its parent) is predetermined in the subdivision process (due to the Cartesian topology) the neighboring cell indices can quickly be determined. In addition many of the search procedures are made efficient using the octree data structure.

Initial Grid Refinement

The initial Cartesian grid is generated based on the resolution of the surface triangulation of each of the 6 faces of the boundary face file. Generally, the surface of the vehicle of interest will contain a much denser mesh of triangular facets than outer boundary face regions. The root cell defined by the boundary face file is termed grid level 1, and is subdivided in the X, Y, and Z directions resulting in eight offspring cells at grid level 2. Each offspring cell is recursively subdivided based on a cell length-scale criterion. The length scale of each cell is compared with the length scale of all the geometry facets that are contained within the cell or are touched by the cell. The cell length scale is defined as the length of the sides of the cell. The length scale of the geometry facet can be defined as the average length of the three sides of the facet. If a particular cell is larger than the facet length scale multiplied by a user-specified scale factor, the cell is subdivided. This process continues down each branch of the octree data structure until all cells without offspring satisfy the length scale criterion

During the subdivision process, grid smoothing constraints are enforced. No cell can have more than four neighbors on any side. This is equivalent to limiting the differences in grid levels between adjacent cells to one. This constraint is enforced so that the octree data structure can be used to rapidly determine the neighbor information of the cells on all grid levels. Any refinement resulting from this constraint quickly propagates through the grid. The

ORIGINAL PAGE IS
OF POOR QUALITY

resulting grid has fine resolution cells near the bodies, and coarse resolution cells in the far field.

The robustness of the grid is checked. Cartesian grid generation may result in cells that are divided into multiple distinct volumes near thin sharp regions, which are invalid. SPLIT-FLOW uses an area summing approach to sum the X, Y, and Z area components of the boundary facets in each cell that lies along the boundary. First, if any of the area components sum to zero while the maximum magnitude of the area component is non-zero, then the cell may be an invalid cell. Second, if large negative and positive summations occur then the cell may be invalid. These checks assure that invalid cells are eliminated.

Grid Adaption

Once the volume grid has been created based on the face geometry, cells within the volume grid are subdivided additionally during the solution to various levels, depending on the local flowfield gradients. SPLITFLOW contains gradient computations of several functions such as static pressure or Mach number. These functions are selected by the user, and are used to refine or derefine the grid. Example results of the volume grid are shown at the top of Figure 2.3. The flowfield gradients around the leading edge, and the burst vortex, are clearly seen in the figure. At the bottom of Figure 2.3, the equation for the grid adaption parameter is shown. The gradient of each chosen adaption function is computed across the cell and multiplied by a length scale. This length scale is calculated from the cell volume and is then adjusted by an exponent based on a user selected term. This gives some control for supersonic flows in which the adaption function gradient across shocks is so high that the cells near the shock tend to dominate the adaption function statistics.

The statistical approach used for assessing the need for grid adaption is shown in Figure 2.4. This approach dramatically reduces the requirement for user decision about grid adaption. Unlike other Cartesian grid schemes, no min/max cell size or tolerance needs to be defined, and no user-defined 'sequence' of adaption (such as a number of cycles each having several grid levels within each cycle). Rather, the actual gradient information is computed across every cell in the entire domain. Physically-based adaption functions (selected by the user) such as pressure or velocity are calculated using these gradients. The user simply defines the thresholds of the values on the adaption function at which cells will be marked for refinement or derefinement. These thresholds (called gradmn and gradmx) are applied to the statistics of the adaption function(s), and are defined in Figure 2.4 as percentage of the standard deviation or (max-median) of each adaption function. Refinement occurs automatically for cells which exceed the threshold. Cells which fall below the lower threshold of the adaption function are marked for derefinement. Derefinement occurs for cells in which all 8 children have been marked. The objective is to create a uniform value of the adaption function across

all the cells and avoid either 'hot spots' in which large gradients exist, or regions of minimal gradient where cells could be removed without disturbing the solution.

Grid adaption occurs when the value of the adaption function as shown in Figure 2.4 exceeds the statistical threshold. The grid cell is subdivided. After all refinement has been completed (or the target number of cells is reached) then grid smoothing is employed to assure that only one level changes between adjacent cells.

The user input file contains the grid generation cell resolution terms (bndscale and dxyzmin) which allow control of the minimum Cartesian cell size. The adaption of the volume grid to flowfield gradients is controlled by the terms gradmx and gradmn in the input file.

As the solution proceeds, refinement events occur periodically. Cells are added or deleted, and the residual spikes then falls. The general trend for the residual is to progressively drop, and generally 3-4 orders of magnitude of convergence of the L2 norm of the residual are achieved.

Numerical Formulation

The governing equations solved are the Reynold's averaged, compressible Navier-Stokes equations. The discrete-integral form of the equations for an arbitrarily-shaped cell with *ns* sides is given as:

$$\frac{\Omega}{\Delta t}\Delta Q + \sum_{m=1}^{ns} (F_i - F_v)_m \bullet (n_m \sigma_m)$$

where *ns* is the number of sides of the cell (to accommodate boundary cut cells), n is the current time level, and s is the current sub-iteration. The flux F and conserved vector Q are from the conventional conservation-law formulation. The cell volume is represented by Ω and Δt is the time step. The outward-pointing unit normal vector for face m is n_m and the surface area is given by σ_m. The inviscid flux for face m is denoted F_i, and the viscous flux as F_v.

A steady-state solution to the governing equations is obtained by using an implicit time marching scheme. Upwind fluxes are used for the inviscid terms, and central differences are used for the viscous terms. A consistent set of flux functions are used in the solution procedure on both the Cartesian grid and the prismatic grid. A point-wise implicit time integration scheme with sub-iterations is used to advance the solution. The numerical form of the implicit equation is:

$$\left[\frac{\Omega}{\Delta t}I + \sum_{m}^{ns}\left(\frac{\delta F}{\delta Q_c}\right)_m\right](\Delta Q_c^s) = \left(-\left[\sum_{m}^{ns}\left(\frac{\delta F}{\delta Q_n}\right)_m\right]\right)\Delta Q_n^{s-1} - (Res)^{n-1}$$

The given cell is c, while each neighbor on the right-hand side is n. Res is the residual vector computed as the sum of the fluxes over the cell. I is the identity matrix.

The flux Jacobians are the inviscid Jacobians consistent with Roe's scheme, computed using first-order extrapolated data. By using the δQ's from the previous subiteration for the neighbor cells and adding the influence to the right-hand side, the equations require a block inversion of a 5X5 matrix for each cell. The inverted matrix is computed during the first subiteration and stored for use in subsequent sub-iterations. Typically, 10 to 20 sub-iterations are used to converge the implicit equation at each time level. Sub-iteration convergence is monitored by the code.

The Courant-Friedrichs-Lewy (CFL) number is automatically adjusted by the code, depending on the subiteration convergence characteristics. CFL numbers on the order of 5 or more are possible for most problems.

The inviscid fluxes are computed using Roe's approximate Riemann solver. A minmod limiter is used to reduce the order of accuracy near discontinuities and prevent overshoots, and the entropy fix of Harten (Ref. 8) is used to prevent non-physical expansion shocks.

User Work-load and SPLITFLOW Domain Definition

The steps of user involvement in creation of a SPLITFLOW grid are shown in Figure 2.5. The user determines the level of surface resolution using the computer-aided design (CAD) system. This surface definition is made up of a number of triangular facets. The outer boundaries of the domain are defined, and a symmetry plane is constructed by running LFWC software tools which read the outer boundary points and the centerline of the CAD surface file to generate a faceted triangulated symmetry plane. The user also makes simple ascii files of the outer boundary faces (consisting of large triangles containing the corner points of the domain) and assembles the faces into a total file using an LFWC software tool, 'spfbnd'. This boundary file is the input to SPLITFLOW, along with a namelist file containing flow conditions, grid adaption parameters, surface integration reference terms and requested print data such as surface pressures. The time required to set up a problem is generally 20 to 40 minutes. The avoidance of volume grid generation and the simplicity of construction of face grids are seminal features of SPLITFLOW. Also, the addition of new surface geometry is easily accomplished, such as a new tail or modified body shape.

3. Attributes of Grids for Euler Technology Assessment

Specific results of the surface and volume grid generation for the Euler Technology Assessment study are shown in this section. The configuration used for the computations was the NASA-Langley Modular Transonic Vortex Interaction (MTVI) model (Ref. 9). The MTVI configuration features a 60-degree clipped delta wing and a large fuselage which extends ahead of the wing. A significant feature of this configuration is the sharp leading and trailing edges on the wing, fuselage and tail. This promotes flow separation and roll-up into upper-surface vortices, and reduces the sensitivity of test and predicted results to Reynolds number effects associated with the onset of vortical flow. The geometry variations used in the study included the position of the vertical tails (centerline vs. wing-mounted), body cross-section chine shape (100-degree included angle vs. 30-degree), and leading-edge flap deflection. The baseline geometry, termed MTVI#1, included twin wing-mounted tails, a 100-degree chine, and a 30-degree leading-edge flap deflection over the inner 60% of the wing span.

The various configurations used for the predictions are shown in Figure 3.1. A sting was added as shown in Figure 3.1, consisting of a reduced-area cross-section extending approximately one body length aft of the body. A tapered region closed the gap between the end of the model and the beginning of the sting. The overall surface grid of each configuration had about 30,000 facets.

The development of a faceted surface file from the CAD definition of each vehicle required that the bodies be closed (with no gaps or mismatches), such that a solid volume could be made. The CAD defined geometries contained the trimmed surfaces for the components (such as upper fuselage, wing, flap etc.) Small mismatches occurred between some of these surfaces. Connecting patches and extensions to surfaces were generated in order to create a solid facet file of each geometry.

Preparation of the face grids was conducted on Silicon Graphics Personal IRIS and IRIS Indigo Extreme workstations. The construction of the Cartesian grids within SPLITFLOW begins with the boundary face file provided by the user. This file, described in the previous section, contains a cubical root cell of the domain. Each face of this file consists of points and connectivity information defining two or more triangular facets. One of the faces is the surface definition of the geometry of interest (from the CAD development discussed above). The maximum cell size for volume grid cells near the outer boundaries was selected to be approximately 12 inches. The domain is subdivided recursively, and each subdivision is termed a level. The progression for MTVI was 0.5^n X 12 inches, to reach the minimum size. A target size for the smallest cells is selected by the user. The nominal minimum cell sizing for several SPLITFLOW runs is shown versus a 'y-plus' parameter in Figure 3.2. These runs were made

using variations in the selected minimum target cell size. Y-plus is typically a measure of the radial spacing required for a viscous grid, but it gives an indication of the relationship between the SPLITFLOW levels for MTVI and radial spacing near the wall. The smallest element in each MTVI facet file had edges of approximately 0.0005 inches. If the target size is on this same order, the resulting 'n' value of 15 (which subdivides the 12-inch largest cells 15 times) corresponds to a y^+ of about 40. In general, this level of near-wall resolution has been adequate for Euler calculations.

4. Pathfinder Study

The first portion of the Euler Technology Assessment study included systematic evaluation of several issues confronting the use of CFD for aerodynamic predictions. This first phase was called the 'Pathfinder' study, since it was in this phase that the basis was established for proper grid techniques and convergence assessment for both low and high angle of attack flows. Two angles of attack were used, a relatively low angle representing a 'benign' vortex condition having a mixture of attached and vortical flow, and a higher angle creating a 'burst' flowfield. The requirements for grid resolution at low and high angle of attack were determined by performing solutions on several grids for each of the flow cases. Another objective was to computationally assess the effect of wind tunnel walls on the configuration aerodynamics. These calculations were made using the 'medium' grid as determined from the grid sensitivity study.

The computational strategy and run plan for the pathfinder study were developed by NASA-Langley, and were provided to all participants. A number of calculations were made during the course of the study, and these are summarized in Table 1. The pathfinder runs are labeled Runs 1-8 in the table. The configurations are listed in the table, along with the corresponding arrangement of flap and tail components, outer boundary geometry and grid resolution. The nominal Mach number used for all calculations was 0.4.

Effect of Grid Resolution

Several grids were generated using SPLITFLOW over the range of cell count from 350,000 to 850,000, and the resulting integrated forces were compared to determine when no significant change occurred with increasing grid resolution. Since flows were to be predicted in which either mixed (attached and separated) flow or fully-separated flow would exist, the grid density studies were conducted at both low and high angles of attack. An example for the angle of attack of 10 degrees is shown in Figure 4.1. Each solution was assumed to converge when the force coefficients reached a steady value with succeeding iterations of the code. Also, the L2 norm of the residual was monitored, and a value of 1.0×10^{-5} or lower was generally selected as a target for convergence of each solution. As shown in Figure 4.1, these converged solutions had different integrated forces depending on the grid resolution selected. The force coefficients reach nominal levels at about 500,000 cells of grid resolution.

At an angle of attack of 35 degrees, shown in Figure 4.2, the forces also converged at about 500,000 cells, but the pitching moment was still showing variation. It was decided to use a target of 600,000 cells for the pitch runs, in order to adequately resolve the flowfield especially at the higher angles of attack. This target was used for all angles of attack, although one

could vary the target cell count for each run as desired to improve efficiency for low angle cases. The ability to set resolution without costly and tedious modification of the volume grid is a distinct advantage of this grid approach.

Solution timing

The time required to generate the volume grids within SPLITFLOW are shown in Figure 4.3 for a Pathfinder run series. The grid boundary cutting process required about 30 to 40 minutes, and the subsequent grid refinement and adaption during the course of the solution required an additional 20 to 40 minutes. These results depend on the number of refinement sweeps requested by the user. Generally for the Pathfinder runs the grid updating and refining was requested frequently (every 10 steps) since the objective was to determine accuracy requirements and not timing. Subsequent 'production' runs of the code have brought down the grid generation and refinement times. As SPLITFLOW has matured, it has been found that the number of iterations and the amount of grid refinement activity can reduced without affecting the solution quality. The convergence and timing for a subsequent solution of Run 2 is shown in Figure 4.4 through 4.7. The solution was run for 300 steps, and convergence appears to have occurred within 250 steps. The overall solution time was 3.3 hours on the C-90. The grid generation took about 700 seconds, and the adaption and refinement was 500 seconds. The cell count, Figure 4.6, shows the developing number of cells which are added during the solution. Three lines are shown on the plot. The top line is the total number of cells. The middle line shows the number of 'active cells', or cells within the domain. The lower line indicates the number of cells without children, which is generally the smallest-sized cells.

The grids for three levels of resolution from the 35-degree flow condition are shown in Figure 4.8. The addition of cells in the vortical region over the wing can be seen for the denser grids. Plots of off-body quantities were made to find the vortex characteristics. An important consideration in off-body flowfield display is the parameter to be used to visualize the flow. The use of total pressure, x-crossflow total pressure and static pressure were compared as shown in Figure 4.9. Cuts were made through the flowfield grid at the six fuselage stations for which surface pressure data were provided, shown in a geometry plot in Figure 4.10. The vortex core can be seen in Figure 4.9 for all three parameters. Total pressure shows a loss near the vortex 'burst' location (in the next-to-last station cut in this figure), but the resolution of the vortical features was poor when total pressure was used. Static pressure coefficient shows a reduced level of suction in the wing cuts, but it is difficult to find the course of the forebody vortex as it trails aft. When the x-crossflow total pressure is computed (using crossflow Mach number to define the isentropic relation) the results on the right-side of the figure show a much better definition of the core of the vortices. The x-crossflow term has the advantage of showing more details of the burst vortex region as seen in the last pressure plane cut in the

ORIGINAL PAGE IS
OF POOR QUALITY

figure. The low values of the x-crossflow term on the forebody suggest that most of the velocity is axial in the forebody 'vortex', such that the computed total pressure using crossflow velocity is low. On the wing, the loss of total pressure due to entropy losses is compensated for by an increase in the crossflow velocity in these regions, such that the total x-crossflow term has a good range of values for plot display. Therefore, the x-crossflow total pressure formulation was used for subsequent plots of off-body flow features.

The comparison of off-body data for the grid resolution study at 35-degrees angle of attack is shown in Figure 4.11. The additional cells provide better resolution of the interaction region between the forebody vortex and the wing vortex at the fifth station cut (just ahead of the vertical tail). Also, the large rotating structures at the last station are better resolved with the grid adaption. Vortex traces were made of the three grid solutions as shown in Figure 4.12. The high grid resolution showed the best tracing of the large mixing region ahead of the vertical tail.

A denser particle trace was made of the solution on the medium grid to show in more detail the flow features. The results for aoa=10 are shown in Figure 4.13 (Run 2), and show a strong tip vortex. The dense-trace results for an angle of attack of 35 degrees are shown in Figure 4.14 (Run 5), and indicate that the wing vortex has encountered adverse conditions near the wing-mounted vertical tail and is lifted off the configuration.

Surface pressures are compared between SPLITFLOW predictions and test results (Ref. 10) in Figure 4.15 on the first three forebody stations that were defined in Figure 4.10. The results indicate the medium grid, Run 5, produced essentially the same prediction of the peak suction in the forebody vortex and its location spanwise as the fine grid, Run 6. Both of these runs showed an under-prediction of the amount of peak suction in the vortex. This is unusual in that in general Euler codes tend to over-predict the level of suction for these flows. The pressure results for the three wing stations is shown in Figure 4.16. Here the effect of increasing grid resolution was to increase the amount of peak suction. The Run 5 results were very close to Run 6, indicating that the size of this 'medium' grid was sufficient. Further refinement in the grid to the level of Run 6 did not improve the degree of correlation with the test data. The code tended to under-predict the amount of suction in the wing leading-edge vortex at the second station, but predicted the continuation of the forebody vortex (the peak seen near the centerline). The general shape of the suction peaks is well predicted.

The integrated force results from all the runs made on the MTVI#1 configuration are shown in Figure 4.17. A drag increment of 0.02 has been added to the predicted results, to estimate the viscous effects. The free-air calculations (Runs 2, 5, and 9 through 13) show good definition of the trends from the test data, including the non-linear pitching moment break at a lift coefficient of 1.0. The predictions made using the tunnel walls (Runs 7 and 8) show an effect

of the walls, including somewhat better agreement with the value of lift at 35 degrees angle of attack. More investigation was made of the tunnel wall case, and is discussed in the next section.

Effect of Wind Tunnel Walls

One of the objectives of the pathfinder study was to assess the effect of wind tunnel walls on the flowfield surrounding the model, and estimate the effect on configuration forces. The symmetry plane of the volume grid for the tunnel wall case (Run 8) is shown in Figure 4.18. The walls are in fairly close proximity to the model at this angle of attack. The far-field grid used for the free-air cases (Run 6) is shown for comparison, and illustrates the large domain used in the free-air computations which should have minimized propagation of solution errors from the far-field boundaries. The adapted grid in the wake regions of the symmetry plane appear somewhat different between the two calculations. Particle traces were made in both solutions as seen in Figure 4.19. These particles were released at the same locations in the flowfield for both the free-air case (Run 5) and the tunnel wall case (Run 8). The streamlines are originated at the same release points for both views. A dramatic difference is seen in the trajectory of the vortex (upper part of the figure). Also, the pattern of the flow region above and behind the wing in the free-air run is significantly different in the tunnel-wall case. These differences suggest that the presence of tunnel walls does have an effect on the flowfield around the configuration. Plots were made of surface static pressures for free-air and wall cases, as seen in Figures 4.20 and 4.21. The tunnel wall results have higher static pressures, which seem to better match the forebody pressures on the lower surface, as well as better matching the trends in the wing upper surface pressures. The effect of tunnel walls on the longitudinal forces and moment are included in Figure 4.17. The predictions for the walls in place are shown as diamond symbols in the figure. At a nominal angle of attack of 35 degrees, two runs were made to show the effect of variation in angle from the 'blockage-corrected' value to the 'uncorrected' value. The lift, drag and pitching moment predictions' agreement with the test data at an angle of attack of 35 degrees were improved with the walls in place. A noticeable effect of the tunnel walls on the forces and moments is indicated by the code. The wake blockage corrections to the wind tunnel data for wall interference effects are known to be very small. Either the code predictions indicate an overestimation of the wall effects, or there may be other influences of the walls on the test data that are not included in the blockage correction terms. Additional studies would be required to more fully investigate the effect of the tunnel walls. The effect of inflow and outflow boundaries, the sting, and grid resolution could be made. Also, predicted blockage effects on exit dynamic pressure could be estimated from surveys of the predicted flowfield at the exit plane.

Assessment of Vortex Burst Location

The location of vortex 'burst' was estimated from the free-air 35-degree solution (Run 5). Several surveys were made of the upper surface as seen in Figure 4.22 at several iterations during the convergence of the run. The U-velocity was surveyed in cross-plane cuts above the wing. Values of U-velocity between -100 and 0 feet/sec were displayed at these planes. It was observed that the vortex emanating from the forebody had significant regions of negative-velocity flow at fuselage stations starting at 20 inches. The formation of negative velocity in ring-shaped structures appeared to grow as the solution sequence proceeded to convergence. The upper-surface vortex over the wing also appeared to develop negative-velocity regions, and the streamlines developed more disorganized behavior as the solution converged. The forces and moments varied during the convergence sequence as seen in Figure 4.23. The movement of the vortex burst position fore and aft corresponded only weakly to variations in lift and pitching moment. The nominal converged position of vortex 'burst' from this data would be around 19.5 inches in the forebody vortex, and 23.5 inches in the wing vortex. Evaluation of other flowfield criteria, and comparison with viscous calculations, is recommended to further evaluate the applicability of Euler results to the determination of vortex burst.

5. Solutions from Run Matrix

The MTVI configurations used in this study were shown in Figure 3.1. After the pathfinder studies were completed, calculations of a series of configurations were made. These runs are listed in the run matrix in Table 1. The baseline configuration was the MTVI#1, having twin wing-mounted tails and a thick 100-degree body chine. The objective of this portion of the study was to assess the timeliness and accuracy of Euler predictions for variations in angle of attack, sideslip and configuration shape.

Baseline Configuration Results

The force results for angle-of-attack variation of the baseline geometry were shown in Figure 4.17. These series of runs are denoted Runs 9-13 in Table 1. The effect of angle of attack on the flowfield is shown in Figure 5.1 with static pressure displayed at several fuselage stations. The forebody vortex is seen to lift up and away from the configuration as angle of attack is increased, while the wing vortex loses suction. More details of the surface pressure were presented for the forebody in Figure 4.15, and for the wing in Figure 4.16. Generally, the code tended to under-predict the peak in suction pressure on the forebody, but performed well in predicting the wing pressures.

Results for Undeflected Leading Edge

The twin-tail configuration with flap undeflected was run at angles of attack of 10 and 35 degrees. These are found as Runs 31 and 32 in Table 1. The pressure data on the forebody at 10 degrees are shown in Figure 5.2. The upper-surface suction pressures at Fuselage Station (FS) 10.45 were over-predicted, but the shape of the curve was well-matched. The code did not predict the onset of vortex flow at the third fuselage station, FS 14.5. The pressure data on the wing at 10 degrees are shown in Figure 5.3. The Euler predictions capture the significant upper-surface flow features, but miss the secondary separation. The magnitude of the peak suction and its location spanwise are also mispredicted.

At an angle of attack of 35 degrees (Figure 5.4 and 5.5), the predicted pressures on the forebody are generally under the peak suction in the data, but the suction peaks on the wing are well predicted except for Station 23.56. The low-energy region on the outer wing panel outboard of the vertical tails is well predicted as seen for Station 28 in Figure 5.5.

The force results for zero-flap deflection is shown in Figure 5.6. The predictions are shown as diamond symbols, and the test data is circles. All longitudinal data for zero flap deflection appears to be well predicted at both 10 and 35 degrees.

Effect of Tail Placement

A centerline-tail version of the MTVI configuration was run in SPLITFLOW and is found as Runs 14 through 17 and Run 33 in Table 1. The effect of moving the tail to the centerline was dramatic. The wing vortex may have 'burst' as it approached the wing-mounted twin tails, as evidenced by a nearly-constant pressure coefficient at FS 28.05 as was presented in Figure 4.21, at an angle of attack of 35 degrees. The effects of the change to a centerline tail will be shown at several angles of attack in the following figures. A comparison of x-crossflow total pressure is shown in Figure 5.7 between the twin-tail configuration and the centerline vertical (CVT) configuration for an angle of attack of 22.5 degrees. The centerline tail causes a large improvement in the upper wing vortical pattern as seen in the increase in intensity of the vortical features near the wing trailing edge. The trace of the vortices in Figure 5.8 shows a significant increase in wing vortex activity with the centerline tail.

In order to examine the effects of tail placement for attached-flow conditions, the pressure data was plotted for an angle of attack 10 degrees and is shown in Figure 5.9 on the forebody. The predicted pressure is above the test levels at the second station, FS 10.45, a consistently-observed difference. The indication of vortex flow at the third station (FS 14.50) was not predicted. An onset in leading-edge separation may have occurred in the test data between FS 6.1 and FS 10.45. The code appeared to predict fully-attached flow in this region. The comparisons of surface pressures on the wing is seen in Figure 5.10. The code predicts the slight drop in suction due to moving the tails to the centerline that is seen in the test data. The peak suction at the hingeline of the deflected leading edge is over-predicted, so it is possible that the code over-predicts expansion regions in fully-attached flow.

The effects of tail position at higher angles is next presented. The forebody pressure data at 22.5 degrees is seen in Figure 5.11. The effect of the change in tail position on the forebody pressures is small. The forebody pressure levels in the underbody regions and near the centerline of the upper surface are predicted well, but the test data shows indications of vortical flow over the forebody. The code appears to predict attached flow on the majority of the upper surface. The pressures on the wing are shown in Figure 5.12. The outer panel of the wing at the last station (FS 28.06) exhibits test pressures that suggest that the wing vortex with the CVT is creating higher suction pressure than the twin--tail configuration with the position of peak suction at approximately the same span station. The flow-reattachment portion of the wing flow (inboard) also shows higher suction for the centerline tail configuration. The code tends to predict the increase in peak suction, but mis-predicts the amount of suction. At the second station (FS 23.56) the code predicts less peak suction than the test results.

The x-crossflow total pressure at 35 degrees, Figure 5.13, shows that the centerline tail causes a large increase in the rotational intensity of the upper-surface vortical structures in the aft

ORIGINAL PAGE IS
OF POOR QUALITY

portion of the wing. This is seen as the darker coloration of the center of the planar cut at FS 28 (the last cut on the wing). The x-crossflow total pressure tends to show a reduction in regions where the axial core velocity is high (and therefore crossflow velocity is lower). The forebody pressure data at 35 degrees is seen in Figure 5.14, and indicates that the tail position did not significantly affect the forebody pressures. The SPLITFLOW predictions show a delay in prediction of the onset of significant vortex peak pressures, since at FS 6.1 the suction levels from the code are flatter and do not have the definite peak of the test data. At the second station, FS 10.45, the code predicts less suction peak, although the position of peak suction is predicted to be farther inboard than seen in the test data. This is somewhat unusual for Euler results, which tend to show an outboard movement of the suction peak versus test data. The level of suction pressure near the centerline at FS 10.45 is slightly over-predicted, a consistent effect seen at this station in all cases. At the third station (FS 14.5) the SPLITFLOW prediction is slightly below the suction level of the test data, although the rest of the pressure data around the fuselage is predicted reasonably well.

The pressures on the wing are shown in Figure 5.15. The effect of moving the tail to the centerline is seen much more clearly at this angle of attack than at 22.5 degrees. As indicated in the flowfield visualization (Figure 5.13) the wing vortex is more robust over the aft two stations than the twin-tail flowfield. The wing vortex peak suction is substantially higher for the CVT arrangement. The SPLITFLOW code predicts the pressure distribution well at the first station, but the prediction does not capture the dramatic rise in suction for the centerline tail at the last two stations. The outer panel of the twin-tail configuration near the wing tip has a low-pressure flat region due to vortex burst. The code predicts this flat region, but the magnitude of the pressure level is not predicted. Examination of the predicted flowfield outboard of the twin vertical tails indicates a low-energy, low-velocity flow. It could be stated that the predicted behavior is analogous to a large-scale separated zone. The test-measured level of pressure in this outer panel region was predicted more closely with SPLITFLOW when the tunnel walls were introduced, as was shown in Figure 4.21.

A comparison of the test and predicted forces and moments for both the twin-tail and centerline tail (MTVI#1 and MTVI#2) are shown in Figure 5.16. The force data for the centerline tail vehicle shows good agreement between SPLITFLOW forces and the test data, up into the nonlinear region. The test data for this configuration has a severe non-linearity above 35 degrees (with a drop in lift and a large unstable pitching moment shift) which is not captured by the code. An additional code prediction was made at an angle of attack of 40 degrees (shown as Run 33 in the test matrix). The code lift, drag and moment predictions above 30 degrees appear to capture the trends of the test data, but not the magnitude. Below this point, the code predictions appear very close to the test results.

Effect of Body Chine Shape

The effect of body cross-section chine shape is shown in the following data. Two chines were used in the current study, with included angles of 100 degrees for the baseline (MTVI#1) and 30 degrees included angle for the 'sharp' chine (MTVI#3). This 'sharp' geometry was used in SPLIT-FLOW Runs 18 through 21 in Table 1. The crossflow total pressure at an angle of attack of 22.5 degrees shows a definite increase in vortex activity for the sharper chine (Figure 5.17). Traces of the vortex core trajectory (Figure 5.18) show that the sharp 30-degree chine has a definitive vortex shed from the forebody which moves aft to the rear. The blunt chine baseline configuration has minimal evidence of vortical flow. The pressure coefficients on the forebody are shown in Figure 5.19. The sharper chine exhibits an inward movement of the peak suction, and an increase in the static pressure on the undersurface at each station. The SPLITFLOW prediction does not capture the suction peak value, and does not indicate the significance of vortical activity on the upper surface of the fuselage. The code predictions do capture the increase in compression on the lower fuselage. The sharp chine causes only a slight increase in suction pressure on the forebody. The wing pressures are shown in Figure 5.20. The predictions show more attached-flow behavior in the wing upper-surface pressures for the baseline than is indicated by the test data. The predictions for the sharp chine show more indication of vortex activity. At 35 degrees, the chine effects on the forebody are more pronounced as shown in Figure 5.21. The prediction shows the trend of inward movement of the suction peak, but has less magnitude of suction than the data except for the last station, FS 14.5. The pressures on the wing, Figure 5.22, indicate good agreement between SPLITFLOW and the test data for the first two wing stations. The last station shows that SPLITFLOW under-predicts the suction in the outer panel, where the pressures are very flat. The forebody vortex at this station creates a suction peak inboard of BL 2 inches. In the test data, this vortex appeared to have less suction for the sharp 30-degree chine case than for the baseline. This is a surprising result. The code correctly predicts this trend, but over-predicts the suction level in the attached flow region between BL 2 and BL 4 inches.

The force and moment results for the different chine shapes are shown in Figure 5.23. The sharp chine has a slight increase in lift, and a nose-up pitching moment compared to the baseline. SPLITFLOW provides good agreement with the force coefficients for this sharp chine vehicle, including the pitching moment break above a lift coefficient of 1.0.

Effect of Sideslip for Twin Tail Configuration

The baseline twin-tail vehicle was run in sideslip at angles of attack of 22.5 degrees and 30 degrees. These runs are noted as Runs 22 through 27 in Table 1. The flowfield was solved for three sideslip angles up to -6 degrees. Surveys of x-crossflow total pressure were made from the zero-sideslip case and the β=-6 degree case at an angle of attack of 30 degrees, and are shown in

Figure 5.24. The windward vortex is closer to the forebody, while the leeward vortex has lifted off. The wing vortex is stronger (tighter and higher suction levels) on the leeward wing. Particle traces (Figure 5.25) show that the windward vortex on the forebody is displaced outboard.

The pressures on the forebody are shown in Figure 5.26 at an angle of attack of 30 degrees and for sideslip of zero and +6 degrees. The data has been 'reversed' to indicate positive sideslip. In this and subsequent pressure figures, the positive-y coordinate points to the windward side of the configuration. The station cuts are therefore oriented as a view looking forward toward the nose of the configuration, with the relative wind coming from right to left. SPLITFLOW predicts the trend of increased suction on the windward side of the upper forebody with sideslip, but mis-predicted the drop in peak leeward-side suction at the first two stations. The wing pressures are shown in Figure 5.27. The effect of 6 degrees of sideslip is to decrease the suction on the leeward wing, and increase the suction on the windward wing, at the first two stations (FS 19.06 and FS 23.56). SPLITFLOW predicted the trend of sideslip, but mis-predicted the amount of peak suction in the upper-surface vortex. At the last wing station (FS 28.06) the surface pressures are very flat on both the windward and leeward wings. The predictions indicate a sizeable vortex on the leeward wing at sideslip. The code does predict the attached flow region and the center-body pressures from BL -5 to BL 5 inches very well.

The predicted forces and lateral-directional moments at an angle of attack of 22.5 degrees are shown in Figure 5.28. Test data was not available for comparison at this condition. The force results at α=30 degrees are shown in Figure 5.29, and indicate that the SPLITFLOW predictions are remarkably accurate in predicting both the non-linear trends in the lateral-directional data and their magnitude. The longitudinal forces (not shown) tended to not change as the configuration was moved into sideslip, except for an increase in drag.

The sideslip results for this configuration indicated that the yawing moment (a restoring moment) was generated by a positive side force. At lower angles of attack, a restoring yawing moment typically occurs due to the negative side forces contributed from the tail, with its moment arm behind the c.g. At α=30 degrees, this configuration has a significant contribution to the yawing moment from the forebody. The flowfield visualization shown in Figure 5.25 indicated that the leeward vortex pulled away from the upper surface, corresponding to the hypothesis that the amount of suction generated on the leeward forebody was less than the suction on the windward side.

A study of these directional stability results was made. SPLITFLOW has numerous plot options that have been developed at LFWC. A comparison was made of the contribution to the yawing, pitching and rolling moments from surface pressures. The data for the yaw moment (not shown) revealed that the net forebody moment is indeed a restoring moment, and that the contribution

from the tails is small. Thus, SPLITFLOW predictions could be used to explain an observed test data effect.

Effect of Sideslip for Centerline Tail

The centerline tail vehicle was run in sideslip at an angle of attack of 30 degrees. These runs are found as Runs 28 through 30 in Table 1. The flowfield was solved using a sideslip angles up to -6 degrees. The x-crossflow total pressure (Figure 5.30) shows that the windward vortex on both the wing and forebody is closer to the body, while the leeward vortex has lifted off. The wing vortex is stronger (tighter and higher suction levels) on the leeward wing. Particle traces (Figure 5.31) show that the leeward vortex on the forebody is lifting off the vehicle, while the windward vortex on the wing is exhibiting unsteady behavior. The pressure data comparison is seen in Figure 5.32 for the forebody. The results are similar to those for the twin-tail configuration; the code credits the trend of suction increase on the windward side of the nose, but not the magnitude of the peak. The wing pressures are shown in Figure 5.33. The SPLITFLOW pressure levels underpredict the peak suction for the zero-β case, and overpredict the vortex activity for the configuration at β=6. At the fifth station (FS 23.5 inch), the test data shows a very flat pressure distribution all across the windward wing. The force results (Figure 5.34) show that the SPLITFLOW predictions capture both the trends and the magnitude of the lateral-directional data reasonably well up to β=4, where a large non-linearity occurs in the test data. This non-linearity could correspond to the flat pressure distribution on the wing, and may indicate a burst vortex condition in sideslip.

The integrated forces from the centerline tail case indicate that more negative side force is generated on the centerline tail configuration than the twin tail configuration. In fact, the predicted change in side force to move from the twin tail to the centerline tail, when multiplied by the moment arm of the centerline tail, agrees with the incremental increase in yawing moment seen for the centerline tail. Therefore, SPLITFLOW accurately predicts the configuration change effects on stability for this change in tail arrangement.

Repeatability and 'Accuracy'

An assessment was made of data repeatability in both predictions and test data. The pressure data comparison is shown for forebody pressures in Figure 5.35. Two wind tunnel data sets are shown, indicating a measure of repeatability in the test pressures. This repeatability appears to be good. The SPLITFLOW predictions are shown for three converged solutions of the free-air case. These solutions were made at different times during the course of the investigation and have different grid densities. Several parameters were changed which influenced the grid resolution near the body and the amount and location of grid adaption. The initial calculation of Run 5 had no cap on cell addition. The repeat run had a limit of 40,000 cells placed on the number of

grid cells added per refinement sweep, which should result in a 'better' answer since the grid is prevented from developing too fast. Also, the CFL stability number was increased from approximately 5 to 20, in order to speed the rate of solution convergence. This may have had a negative effect on the results, since the solution had less-stringent requirements for convergence in each subiteration. The difference in the CFD results suggests that some 'scatter' can be assigned to CFD results depending on a variation in the input parameters. A more complete investigation which varies input Mach number, velocity gradients across the test section etc. would provide a more complete assessment of CFD 'uncertainty'.

A comparison was made of the force coefficient repeatability. The repeat data is shown in Figure 5.36. In this figure, repeat test data at α=30 degrees are shown for the twin-tail vehicle. These results show that the test data was very repeatable. Predictions using SPLITFLOW are shown for several repeat runs at 35 degrees angle of attack. Input variables contributed to changes in the force results. The first Run 6 prediction had a small minimum cell size criterion of 10^{-5}. For the Run 6 repeat calculation, the criterion was increased in size to put a floor on the Cartesian grid generation near the body. The difference in repeat data was slightly more than that seen in the test data, with differences in lift and drag on the order of 1% to 2%. For the Run 5 predictions, the parameters that were varied were the CFL and cell addition per step parameters that were used for the pressure comparison. The overall comparison shows that the CFD solution has somewhat more 'uncertainty' than the test data.

It was observed over all the configurations run in this study that the SPLITFLOW Euler predictions provided a good prediction of the trend in surface pressure resulting from a configuration change, but the magnitude and the location of suction peaks was generally missed. SPLITFLOW generally produced under-prediction of suction peaks. Increased resolution near the body surface would improve the prediction of local flow expansion around the leading edge. Since the current study utilized the surface facet geometry as the determining parameter on cell size near the wall, it is possible that improvements could be made by allowing the code to refine to one or more additional 'levels' in order to subdivide the near-surface cells further. This would drive up the overall size of the grid, and was not done in this study since in the Pathfinder evaluation the convergence of integrated forces was used as the criterion for assessing the level of resolution needed to achieve a grid-independent solution.

The fact that integrated forces appeared to be better predicted than surface pressures may indicate that force data alone is not a reliable assessment of the accuracy of these methods. However for preliminary design evaluations, the remarkable resolution of forces and moments shown in this study is a substantial indication that Euler codes can be used with confidence for design evaluation of configuration shaping variations.

6. Conclusions

Results of this study verified the accuracy of Euler results for predicting configuration shaping effects on sharp-edged vehicles at subsonic speeds. In addition, the ability of CFD to produce results within hours was demonstrated. Force and moment comparisons with wind tunnel data on the MTVI configuration demonstrated that Euler calculations can provide meaningful force and moment predictions for configuration shape changes, including prediction of low- and high-angle of attack forces and the effects of sideslip. The use of the residual L2 norm and monitoring of force and moment data during convergence of each solution provided adequate ability to track convergence to a satisfactory result.

The SPLITFLOW code performed the grid generation tasks for all the configuration perturbations, including leading-edge flap deflection effects. This capability allows much more rapid evaluations in the design environment, since complex grid generation by the user is avoided. Solution times for SPLITFLOW are being reduced with evolution of the code, and are approaching the 3-hour level including grid generation.

Several useful conclusions can be made from the pathfinder study. The predicted results indicated that wind tunnel wall effects were predicted to be significant on pressures and integrated forces. The blockage corrections applied to the data did not reflect this effect. The results also show the sensitivity of forces and moments to grid resolution. This is an important aspect of the 'uncertainty' of CFD predictions, along with other sources of uncertainty in the code input parameters. A third significant observation was that the surface pressure predictions were generally in good agreement with test data in attached flow regions, but the development and magnitude of suction peaks associated with upper-surface vortex structures was underpredicted by the code. Several calculations were repeated using different grid densities, and different grid adaption parameters, but these results were not altered.

The second phase of the investigation showed that SPLITFLOW provided reliable trends for force and moment effects of configuration shaping at both low and high angles of attack. Predicted forces and pressures were compared to test data on the MTVI configuration. The predictions achieved good comparison with forces and moments. Surface pressures were generally well-predicted in attached-flow regions such as the underside of the forebody and inner portion of the wing. The peak suction values were generally underpredicted.

An illustration of the accuracy of the prediction was in the effect of a change in vertical tail position on yawing moments in sideslip. SPLITFLOW predictions of the side force and yawing moment were exemplary of the test data up to 6 degrees of sideslip at a relatively high angle of attack, 30 degrees. SPLITFLOW analysis revealed that for the twin-tailed configuration (MTVI#1) the yawing moment was generated on the forebody, not the wing-mounted tails. Movement of

the tail to a centerline position created side force and yawing moment increments which matched the test data. This degree of analysis depth can be very helpful in diagnosis of configuration shaping issues.

Specific recommendations are made for future studies. These include the evaluation of SPLITFLOW for transonic predictions. Reliable prediction of transonic drag rise and wave drag, lift and moment at supersonic speeds are valuable for shape optimization. Multi-disciplinary studies of transonic cruise and supersonic cruise vehicles generally include the aerodynamic impacts of shape changes. If MTVI data is available at Mach numbers for which transonic flow occurred, this would be an excellent candidate for evaluating the suitability of Euler codes in these regions. Also, the need exists to rapidly and accurately predict the control effectiveness of control surfaces, and the hinge moments for leading-edge flaps. It is suggested that additional comparisons be made using force and pressure data for deflected flaps and control surfaces. The high-angle-of-attack arena is a possible area for investigation. Since the MTVI forebody has a sharp leading edge, cross-section effects can be studied without the uncertainty of predicting the crossflow separation point. Finally, the grid generator in SPLITFLOW includes prismatic grids for viscous analysis. Investigations could be made of viscous vs inviscid vortical strength, core location, and formation of secondary separation. Also, the location and character of vortical bursting at higher angles of attack could be investigated. SPLITFLOW has the capability to resolve the off-body flow structures by grid adaption to flowfield gradients, resulting in better prediction of these structures.

7. Acknowledgments

This effort was sponsored by NASA-Langley Research Center under Contract NAS-1-19000. Significant technical guidance was provided by Farhad Ghaffari of the Transonic/Supersonic Aerodynamics Branch of NASA-Langley Research Center. His assistance is gratefully acknowledged. Computer time on the C-90 machine 'vonneumann' of the National Aerodynamic Simulator was provided by NASA-Ames Research Center.

References

1. Karman, S.L., "SPLITFLOW: A 3D Unstructured Cartesian/Prismatic Grid CFD Code for Complex Geometries," AIAA-95-0343.

2. Hicks, R., etal, "Euler and Potential Computational Results for Selected Aerodynamic Configurations," *Progress in Astronautics and Aeronautics: Applied Computational Aerodynamics*, P.A. Henne, Editor, Vol. 125, AIAA, Washington, D.C., 1990, pp. 263-290.

3. Raj, P., Olling, C. R., Sikora, J. S., Keen, J. M., Singer, S. W., and Brennan, J. E., "Three-Dimensional Euler/Navier-Stokes Aerodynamic Method (TEAM), Vol. I: Computational Method and Verifications," WRDC-TR-87-3074 (Revised), June 1989.

4. Buning, P. G., Chan, W. M., Renze, K. J., Sondak, D. L., Chiu, I. T., and Slotnick, J. P., "OVERFLOW User's Manual, Version 1.6ab," NASA Ames Research Center, Moffett Field, CA, January 1993.

5. Frink, N. T., "Upwind Scheme for Solving the Euler Equations on Unstructured Tetrahedral Meshes," AIAA Journal, Vol. 30, No. 1, 1992, pp. 70-77.

6. DeZeeuw, D., Powell, K.G., "An Adaptively-Refined Cartesian Mesh Solver for the Euler Equations," AIAA-91-1542-CP.

7. Melton, J.E., Enomoto, F.Y., Berger, M.J., "3D Automatic Cartesian Grid Generation for Euler Flows," AIAA-93-3386-CP.

8. Harten, A., "High-Resolution Schemes for Hyperbolic Conservation Laws,", Journal of Computational Physics,. vol. 49, pp. 357-393, 1983.

9. Farhad Ghaffari, private communications, NASA Langley Research Center.

10. Farhad Ghaffari, private communications, NASA Langley Research Center, data courtesy Dr. Robert M. Hall, NASA Langley Research Center.

Table 1: RUN MATRIX FOR EULER TECHNOLOGY ASSESSMENT

Run	Configuration	α	β	Chine	Tail	LEF, deg	Grid	Remarks
1	MTVI#1	10	0	100	Twin	30	coarse	Pathfinder grid resolution
2		10					medium	Pathfinder grid resolution
3		10					fine	Pathfinder grid resolution
4		35					coarse	Pathfinder grid resolution
5		35					medium	Pathfinder grid resolution
6		35					fine	Pathfinder grid resolution
7		10					medium	Pathfinder tunnel walls
8		35					medium	Pathfinder tunnel walls
9		22.5					medium	Additional aoa on bsln
10		30						
11		40						
12		45						
13		50						
14	MTVI#2	10	0	100	CVT	30	medium	Effect of centerline tail
15		22.5						
16		30						
17		35						
18	MTVI#3	22.5	0	30	Twin	30	medium	Effect of sharper chine
19		30						
20		35						
21		40						
22	MTVI#1	22.5	2	100	Twin	30	medium	Sideslip, Twin tail
23			4					
24			6					
25		30	2					

Table 1: RUN MATRIX FOR EULER TECHNOLOGY ASSESSMENT

Run	Configuration	α	β	Chine	Tail	LEF, deg	Grid	Remarks
26			4					
27			6					
28	MTVI#2	30	2		CVT	30	medium	Sideslip, Centerline Tail
29			4					
30			6					
31	MTVI#1	10	0	100	Twin	0	medium	Effect of zero LEF
32		35						
33	MTVI#2	40			CVT	30	medium	High-aoa case

Definition of Terms:

CVT: centerline vertical tail
Twin: twin tails mounted on wing upper surface
LEF: leading-edge flap
Chine: forebody cross-section angle between lower and upper surface

SPLITFLOW Grid Topology

Approach: Use hybrid grid scheme, combining a prismatic grid for efficient resolution of the boundary layers with the flexibility of the Cartesian grid in the remainder of the domain.

Grid is automatically generated externally from user's supplied geometry file with minimal input from user.

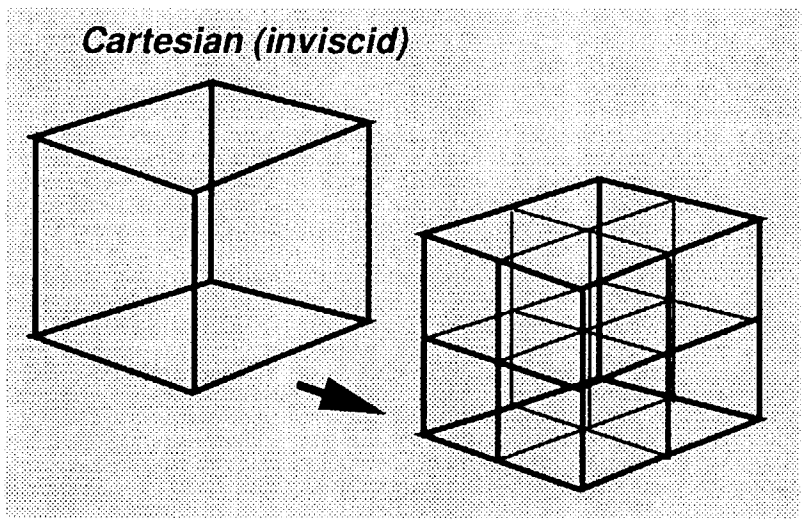

Cartesian grid subdivided from root cell

Eight offspring at each grid level

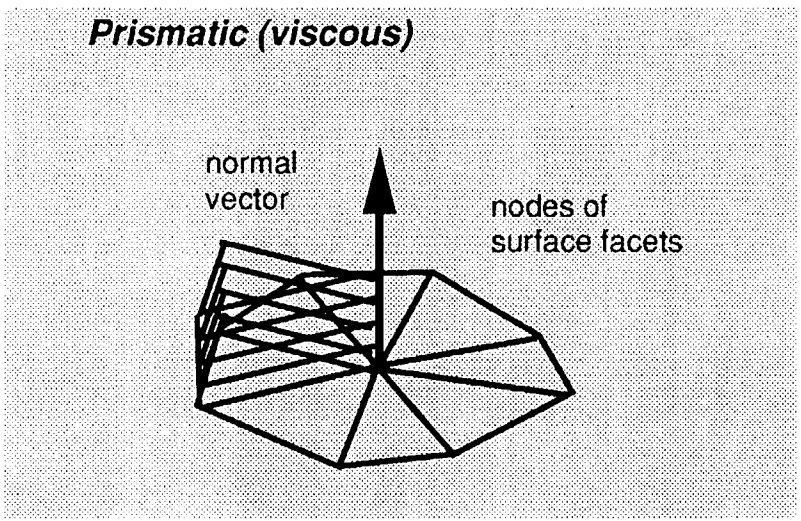

Normal vector is constructed by averaging of common–face normals to eliminate grid crossing

Prismatic grid is "structured" in the direction normal to the body and "unstructured" in the tangential direction.

- **Upwind Flux Difference Split scheme for inviscid terms and central differences for the viscous terms.**
- **Same implicit solver for the prismatic grid and the Cartesian grid.**

Figure 2.1. SPLITFLOW Grid Topology

ORIGINAL PAGE IS OF POOR QUALITY

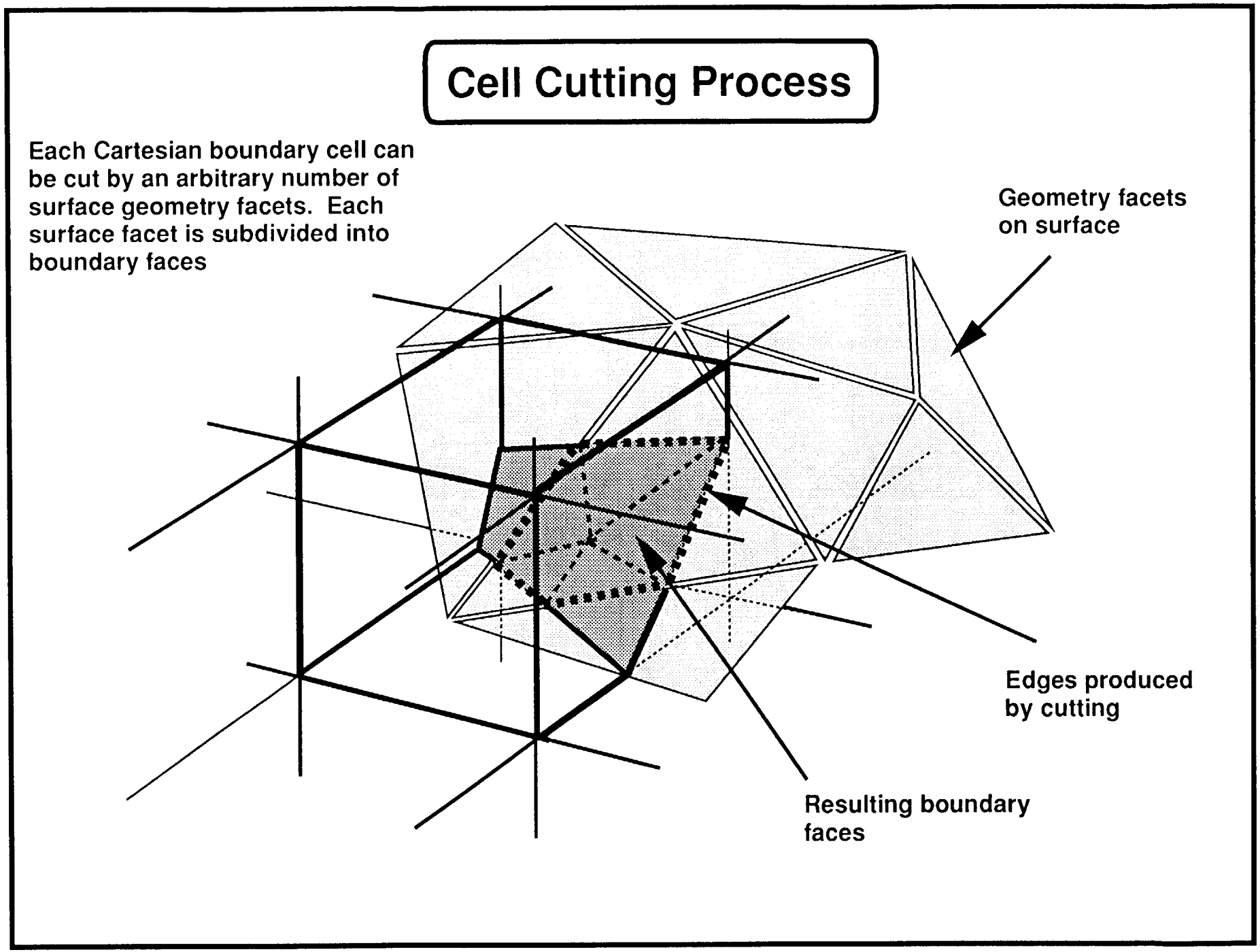

Figure 2.2. Cell Cutting Process

Grid Adaption is Provided within SPLITFLOW

Euler solution, Mach=0.4, $\alpha = 35$ deg. $\delta = 30$ deg.

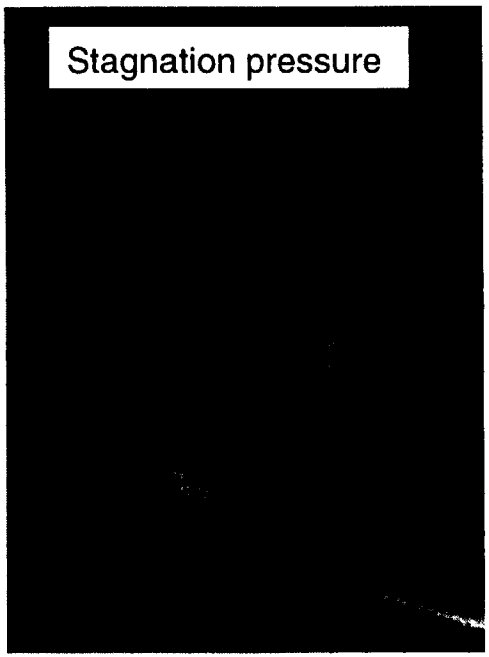

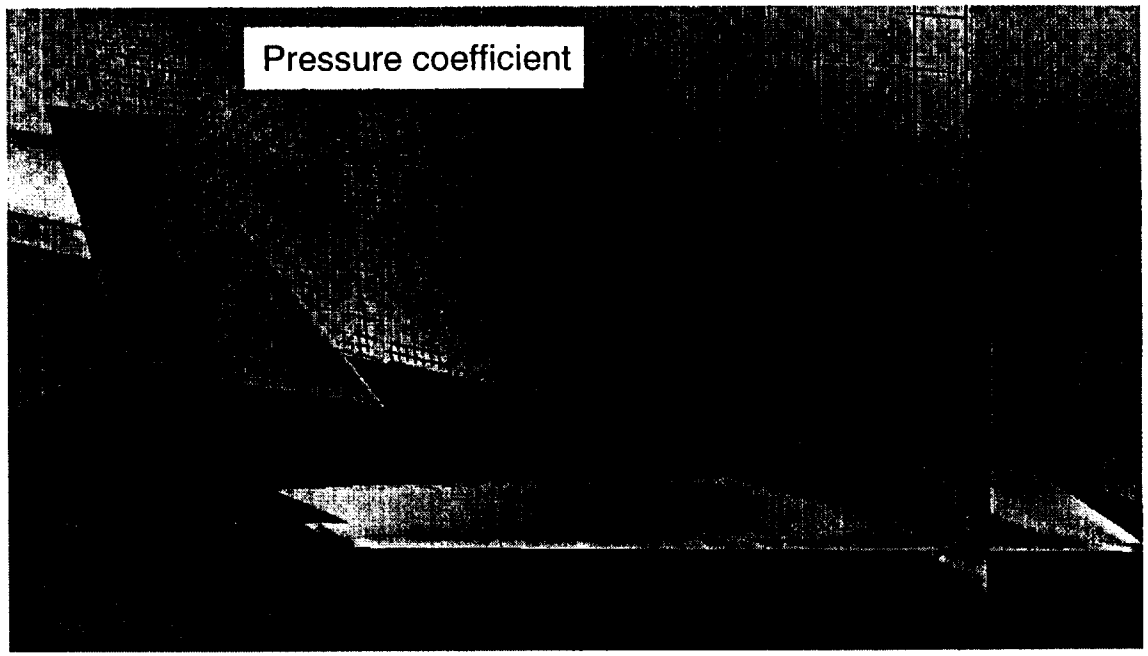

Adaption functions include gradients of: stagnation pressure, local static pressure, local velocity, Mach number, and helicity

Gradient across cell is computed in x, y, z direction

For each adaption function i:

$$fx = | \text{gradient}_i (x) * tx^{(1. + \text{grdpow}(i))} |$$

Similar for y,z

Length scale tx (cell n) = vol(n)/max(area(n,1) + area(n,2))
Scaling term grdpow is used to provide increased control for small cells

Figure 2.3. SPLITFLOW Adaptive Refinement / Derefinement

Typical adaption function --
*Gradient of stagnation pressure across cell in computational space * length scale.*
Compute in each direction (x,y,z) and find rms value.

For gradmx > 0
boundary is set as a % of all cells
median+ (max−median)*gradmx

For gradmx < 0
boundary is set as a % of σ
mean+ σ *|gradmx|

Gradmn uses similar relationships

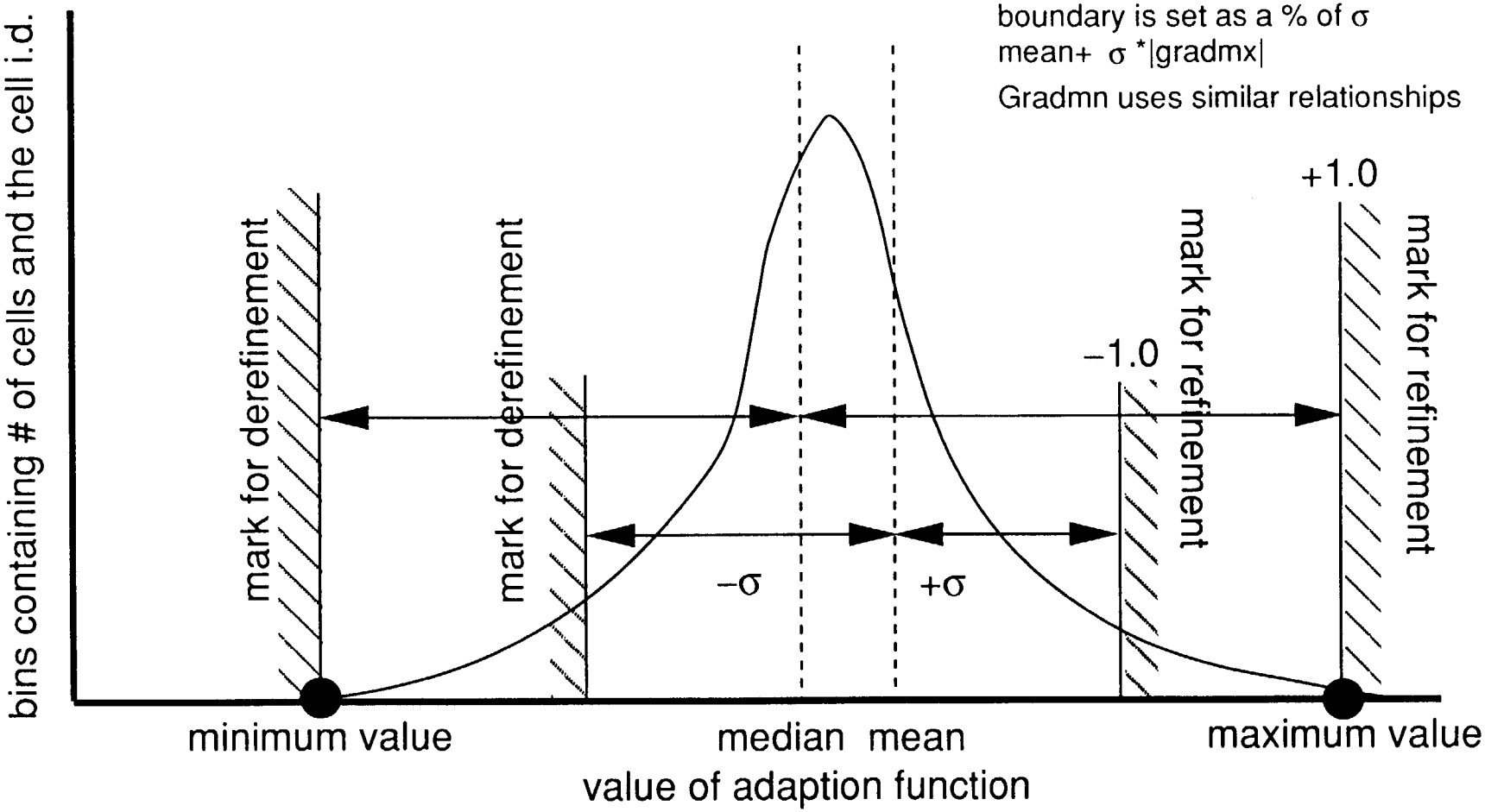

Derefine: Marked cells that have all 8 children marked are derefined.
Refine: Marked cells are checked for dxyzmin before refinement.

Figure 2.4. Statistical Grid Adaption Procedure

Splitflow Grid Generation Sequence

Receive Facet file of configuration from CAD

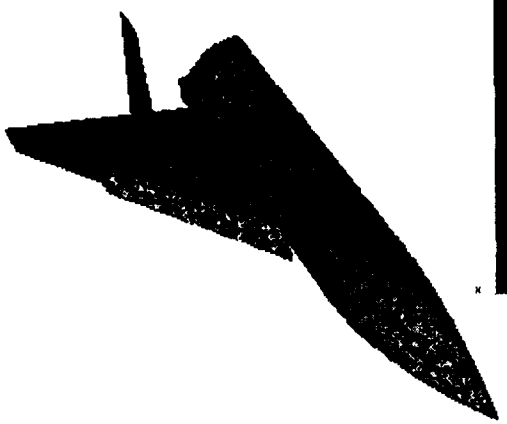

Generate facet file for symmetry plane

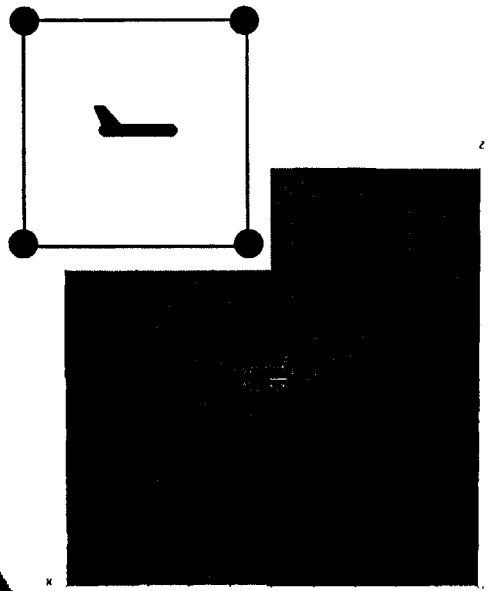

sym_cut.c
qnode.c
sweep.c

Assemble faces of volume grid

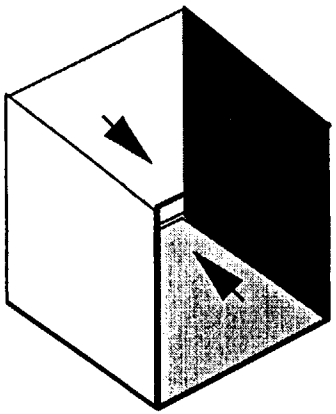

spfbnd.c

Begin flow solution, generate volume grid within code during solution

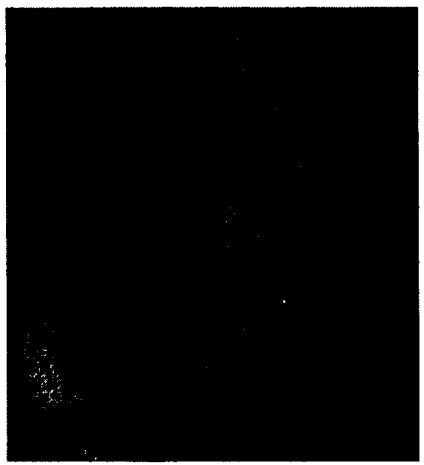

spf3d.inp

user grid refinement decisions

select refinement of body surface facets, which results in code's refinement near surface

select extent of domain

none

select maximum number of cells,
select adaption function(s)
select range of cells to be refined or derefined

Figure 2.5. SPLITFLOW Grid Generation Sequence

Surface Grid for SPLITFLOW is Generated using LFWC CAD

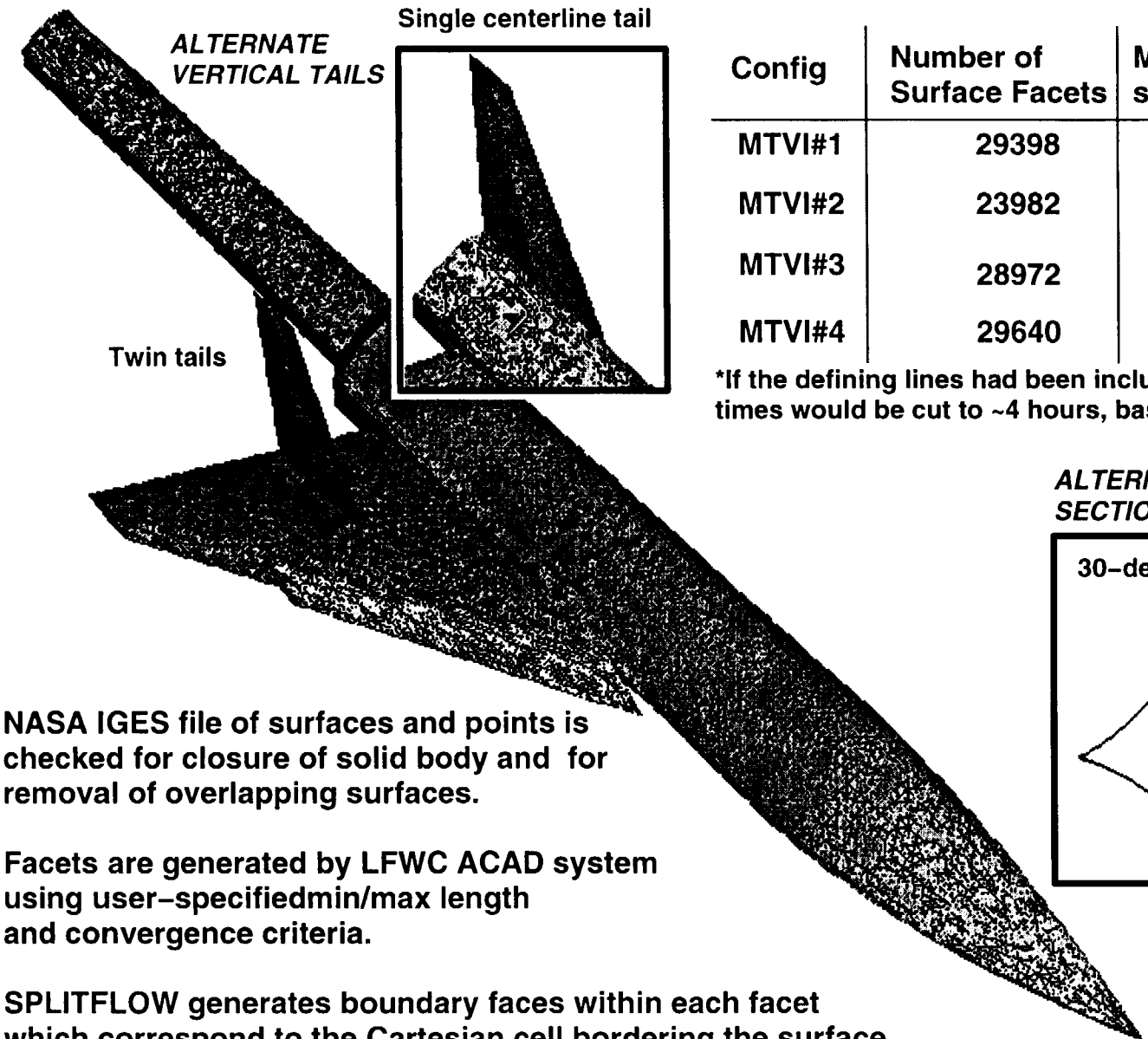

Config	Number of Surface Facets	Manhours for surface preparation*
MTVI#1	29398	24
MTVI#2	23982	24
MTVI#3	28972	16
MTVI#4	29640	8

*If the defining lines had been included in the IGES file, these times would be cut to ~4 hours, based on other LFWC studies

ALTERNATE FUSELAGE CROSS-SECTION SHAPES

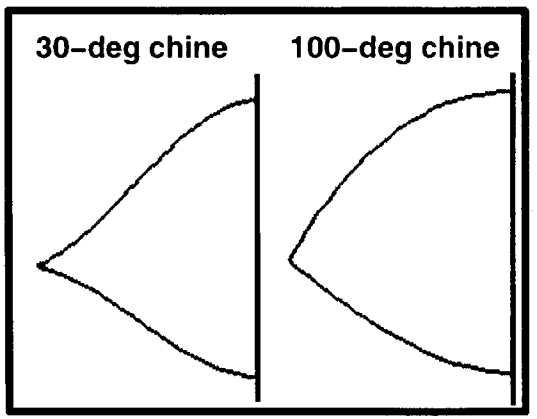

NASA IGES file of surfaces and points is checked for closure of solid body and for removal of overlapping surfaces.

Facets are generated by LFWC ACAD system using user-specifiedmin/max length and convergence criteria.

SPLITFLOW generates boundary faces within each facet which correspond to the Cartesian cell bordering the surface.

Figure 3.1. Surface Grid for SPLITFLOW is Generated using LFWC CAD

For max cell size of 12.5 to 12.8 inches:

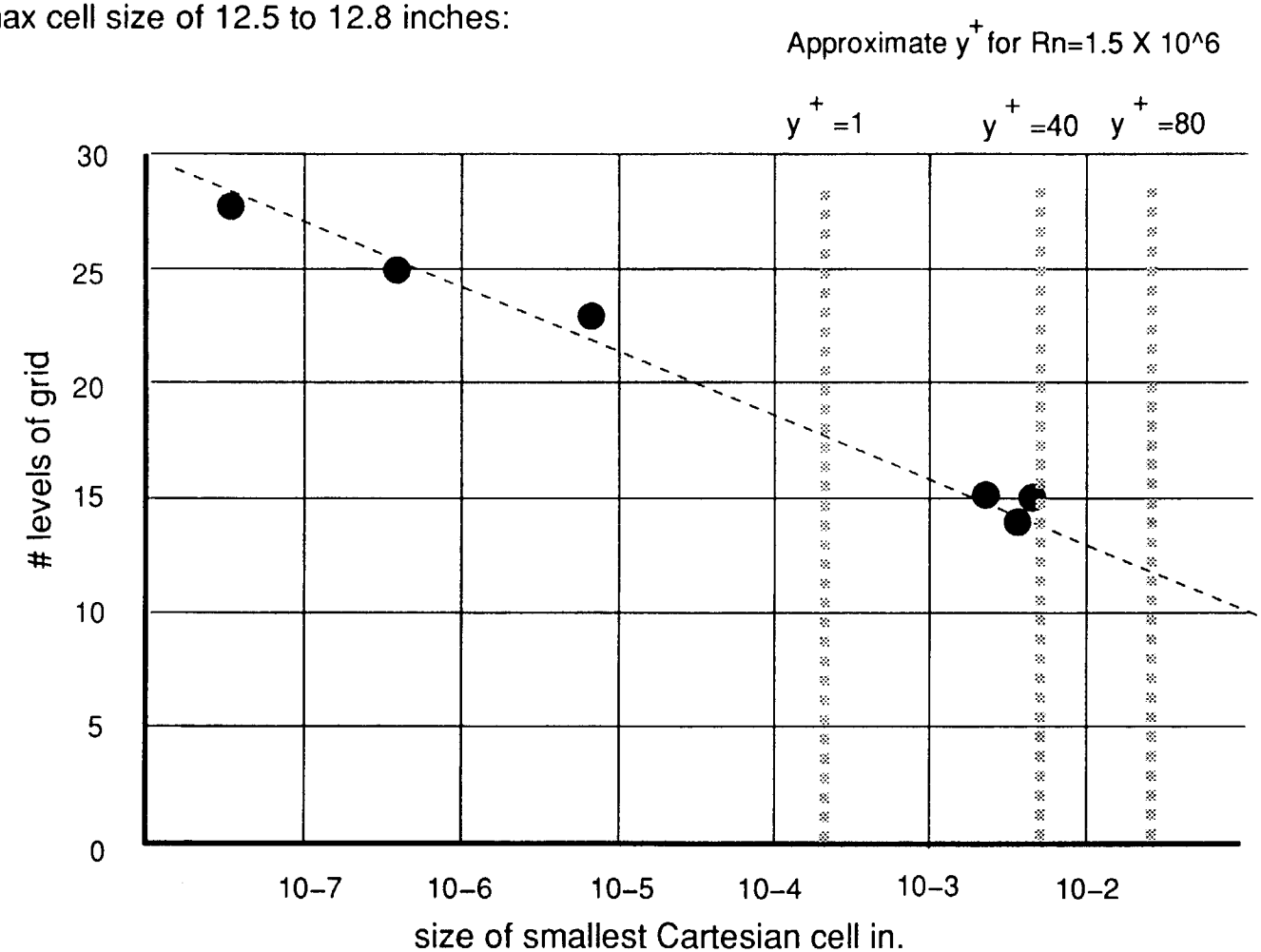

Figure 3.2 SPLITFLOW Grid Statistics for Cell Size versus Grid Levels

MTVI#1: M=0.4, Alpha=10, LE Flap Defl.=30

Sref=1.4458 ft^2, Xcg=20.355 inch, c-bar=12.97 inch

SYM	Data
—O—	SPLITFLOW free-air

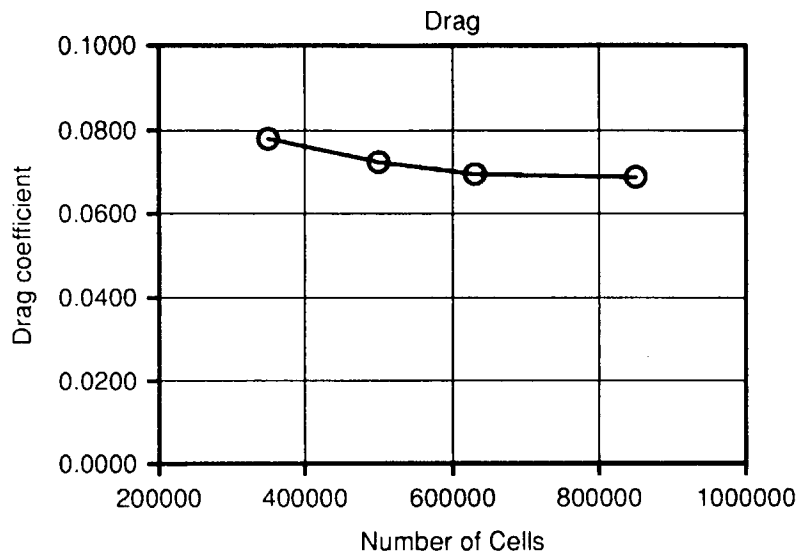

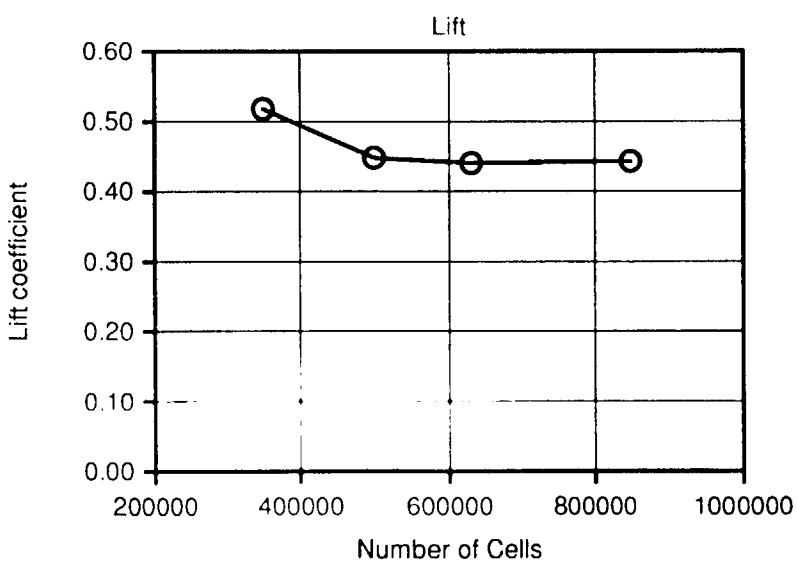

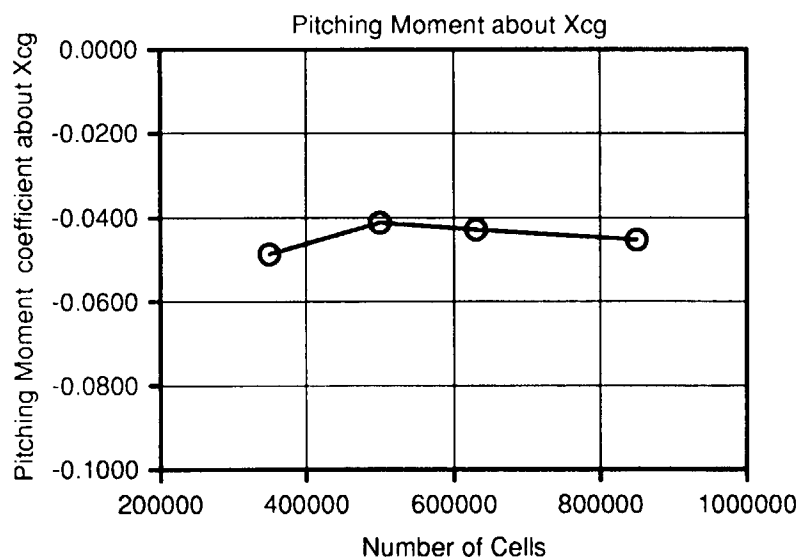

Figure 4.1. Grid Refinement Effects at Aoa=10

MTVI#1: M=0.4, Alpha=35, LE Flap Defl.=30

Sref=1.4458 ft^2, Xcg=20.355 inch, c-bar=12.968 inch

SYM	Data
—O—	SPLITFLOW free-air

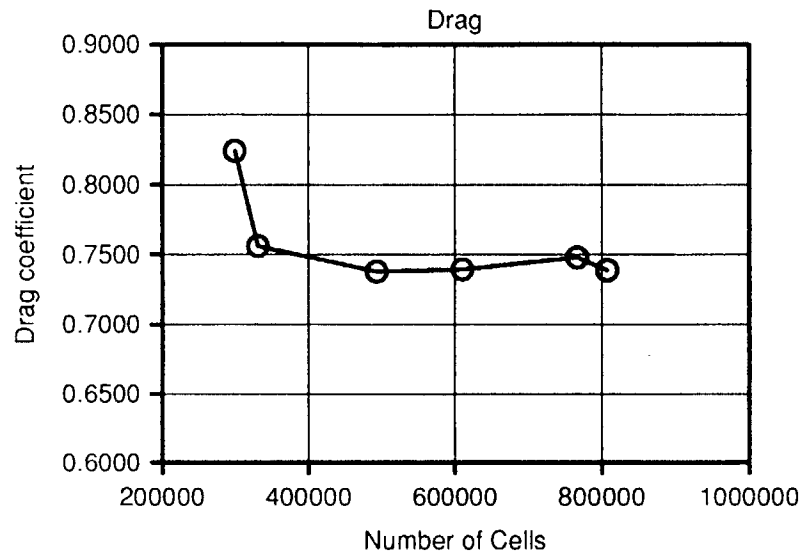

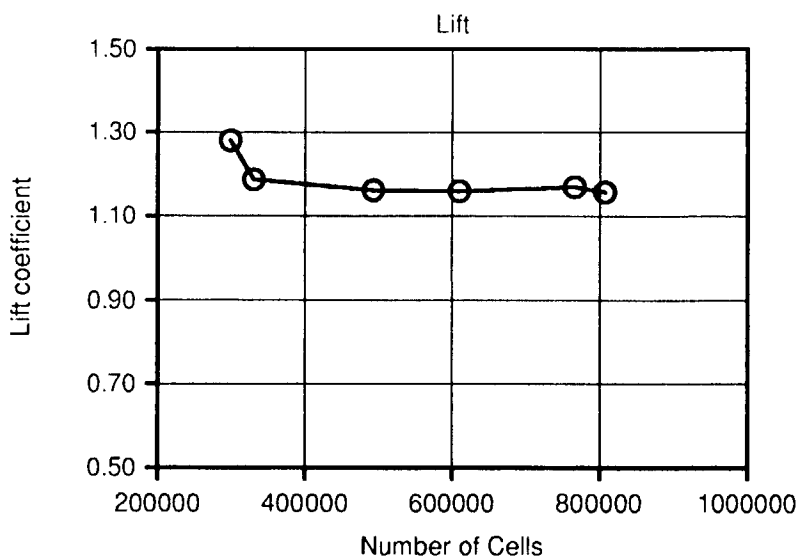

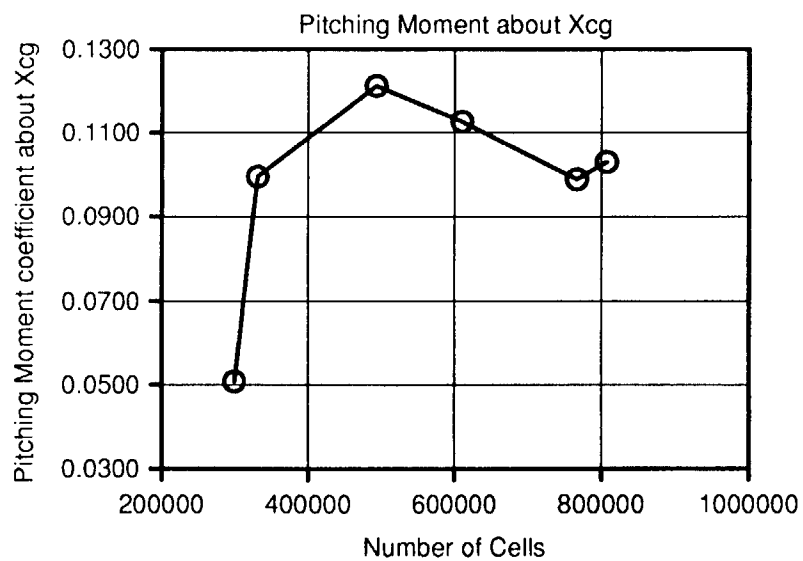

Figure 4.2. Grid Refinement Effects at Aoa=35

Euler solution, Mach=0.4, $\alpha = 35$ deg. $\delta_{lef} = 30$ deg.

Flowfield grid using adaption to gradients of stagnation pressure, local static pressure and local velocity

Run number	Grid resolution	total cells	near-wall spacing, in	Grid Generation man-hours	C-90 CPU (sec) Surface	Refine-ment
4	coarse	350K	1.2×10^{-2}	30 min	1400	1290
5	medium	600K	6×10^{-3}	0	1800	1600
6	fine	850K	1.2×10^{-5}	0	2000	1700
8	tunnel wall	600K	3×10^{-3}	1 hr	2000	1900

Man-hours are required only to define the extent of the outer boundaries, create the symmetry plane facet file using LFWC software tools, and assemble the boundary facet file. Runs 5 and 6 utilized the same boundary definition as Run 4, so no efforts were required.

Surface grid generation time includes automatic generation of all Cartesian cells near the boundaries, as well as generation of 'cut' cells containing actual boundary surfaces. Recursive subdivision to resolve surface features occurs within SPLITFLOW to the user-specified target resolution.

Typical 'production' runs required less grid generation time, on the order of 1000-1500 CPU seconds for the entire grid generation and refinement process.

Figure 4.3. Grid Generation and Adaption Results for Pathfinder Study

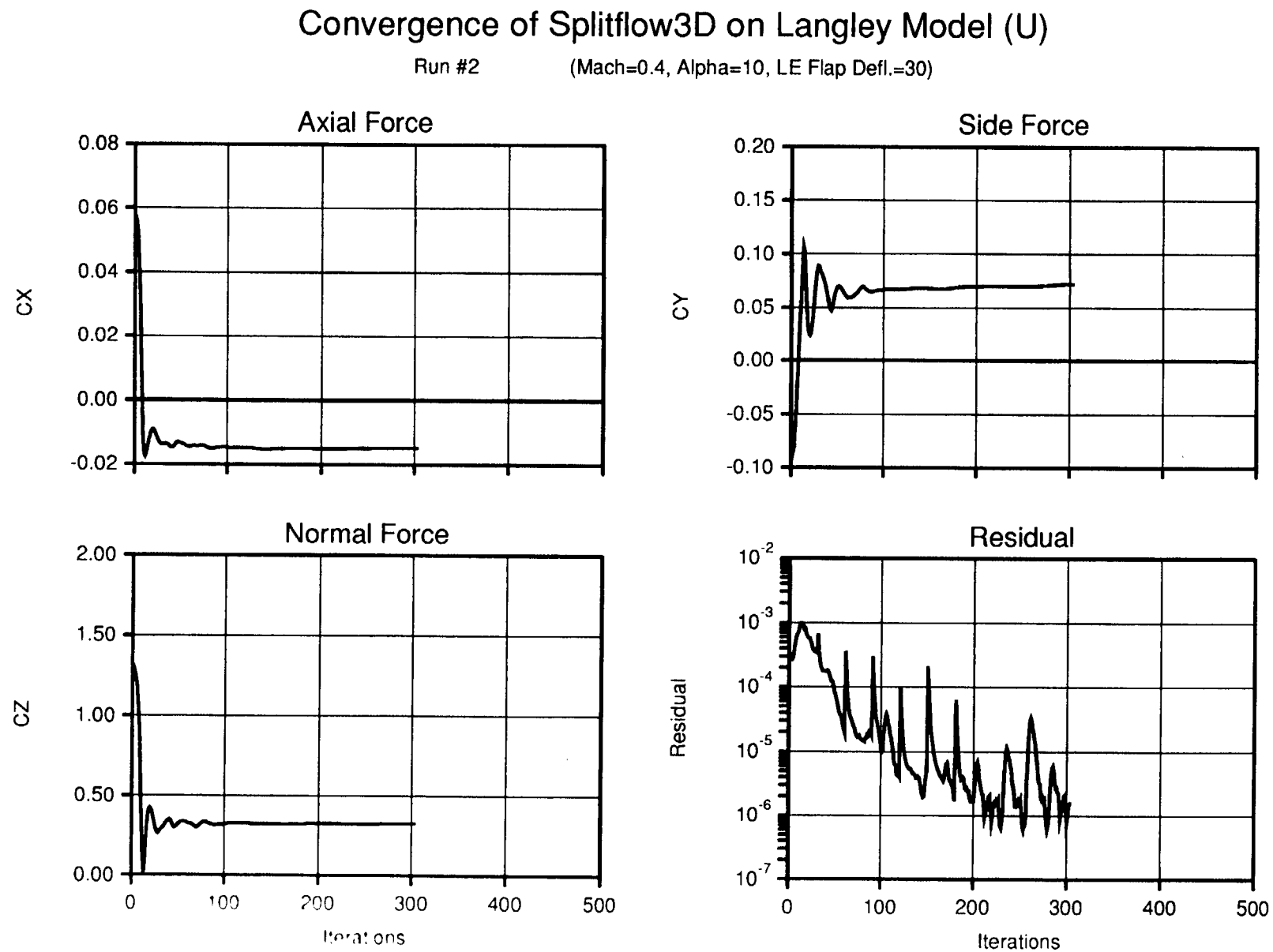

Figure 4.4. Convergence of Forces

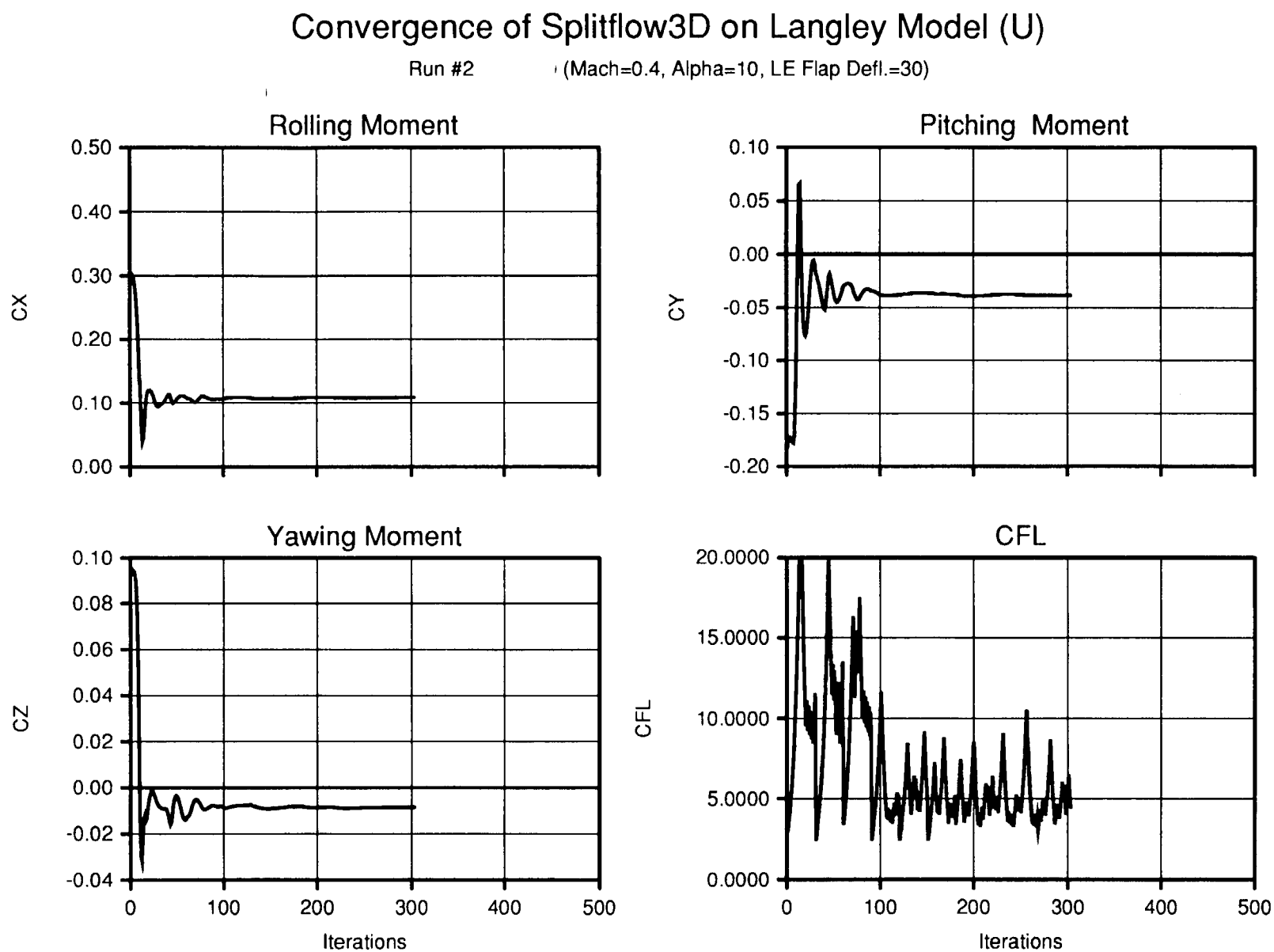

Figure 4.5. Convergence of Moments

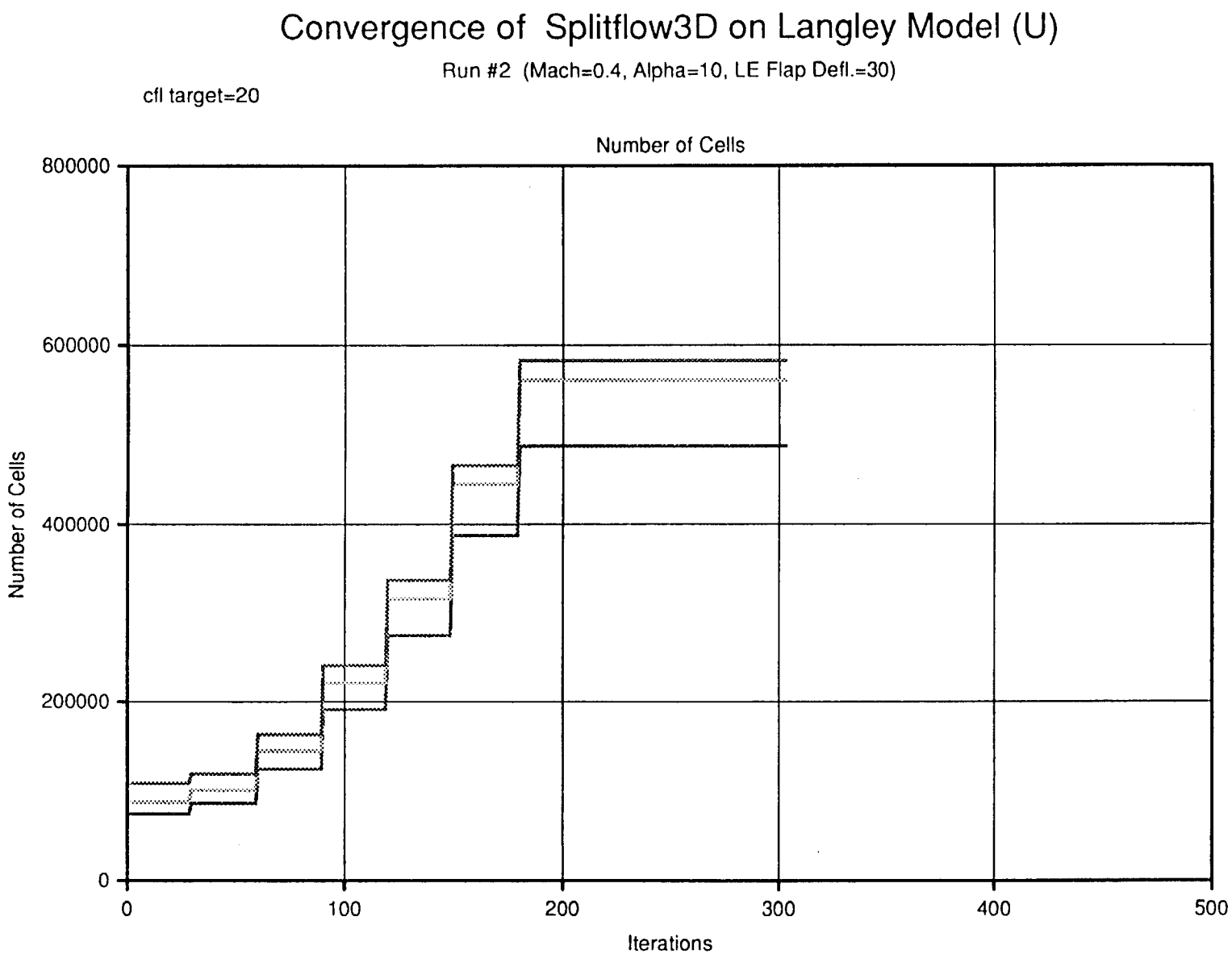

Figure 4.6. Cell Buildup over Course of Run

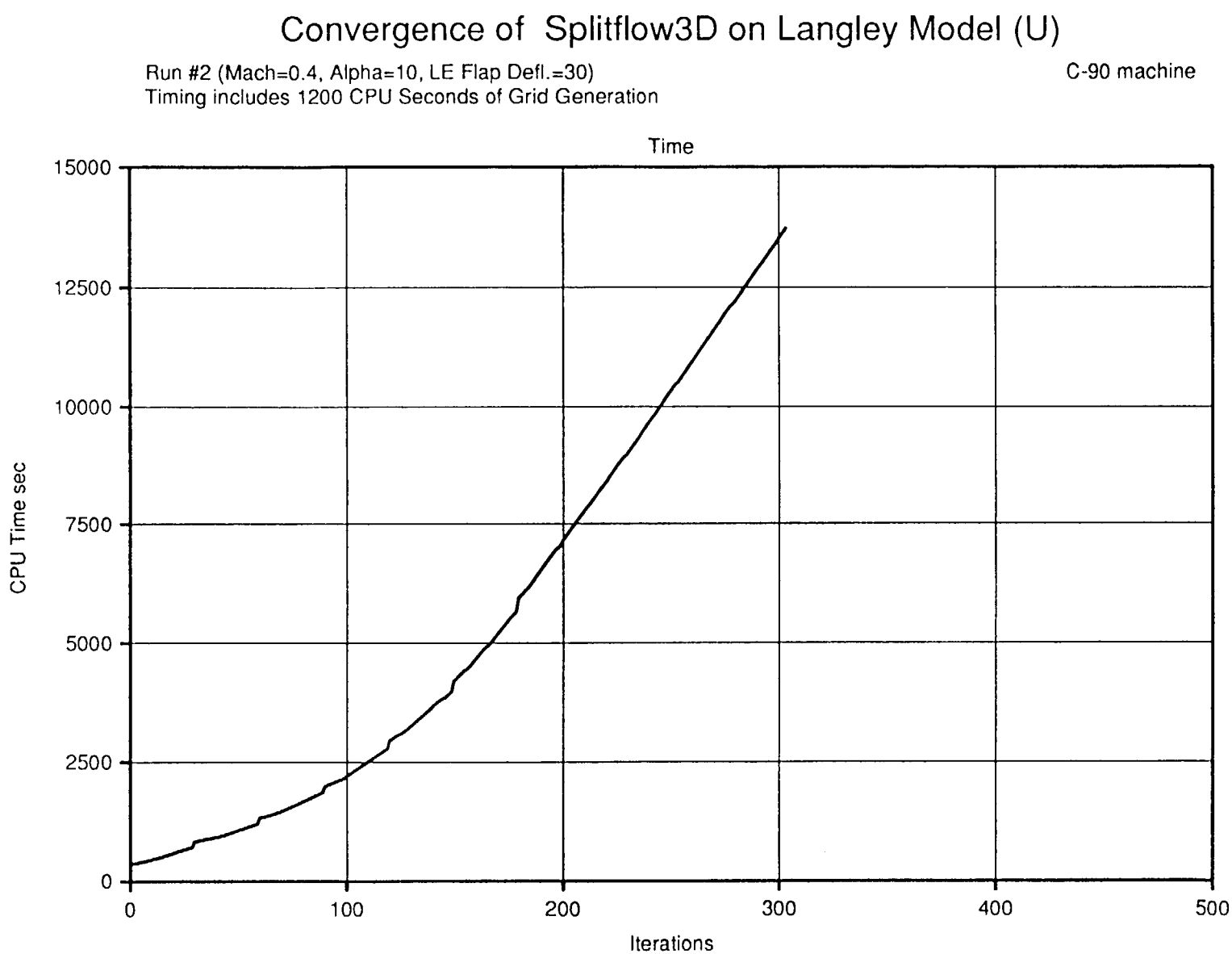

Figure 4.7. CPU Time Requirements During Run

Pathfinder Grid Resolution

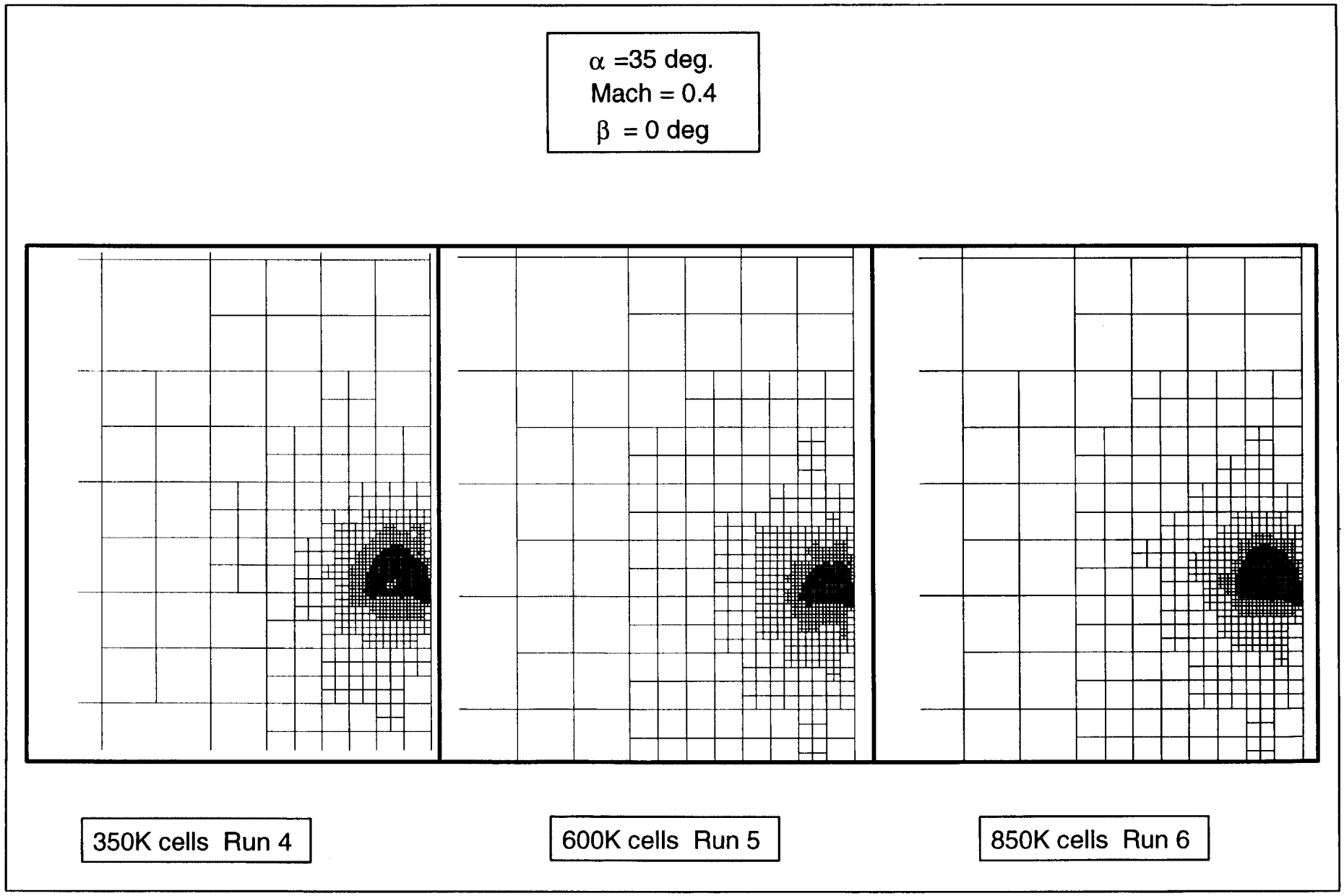

Figure 4.8. Pathfinder Grid Resolution

Use of Ptot Defined from X–Crossflow to Define Flowfield

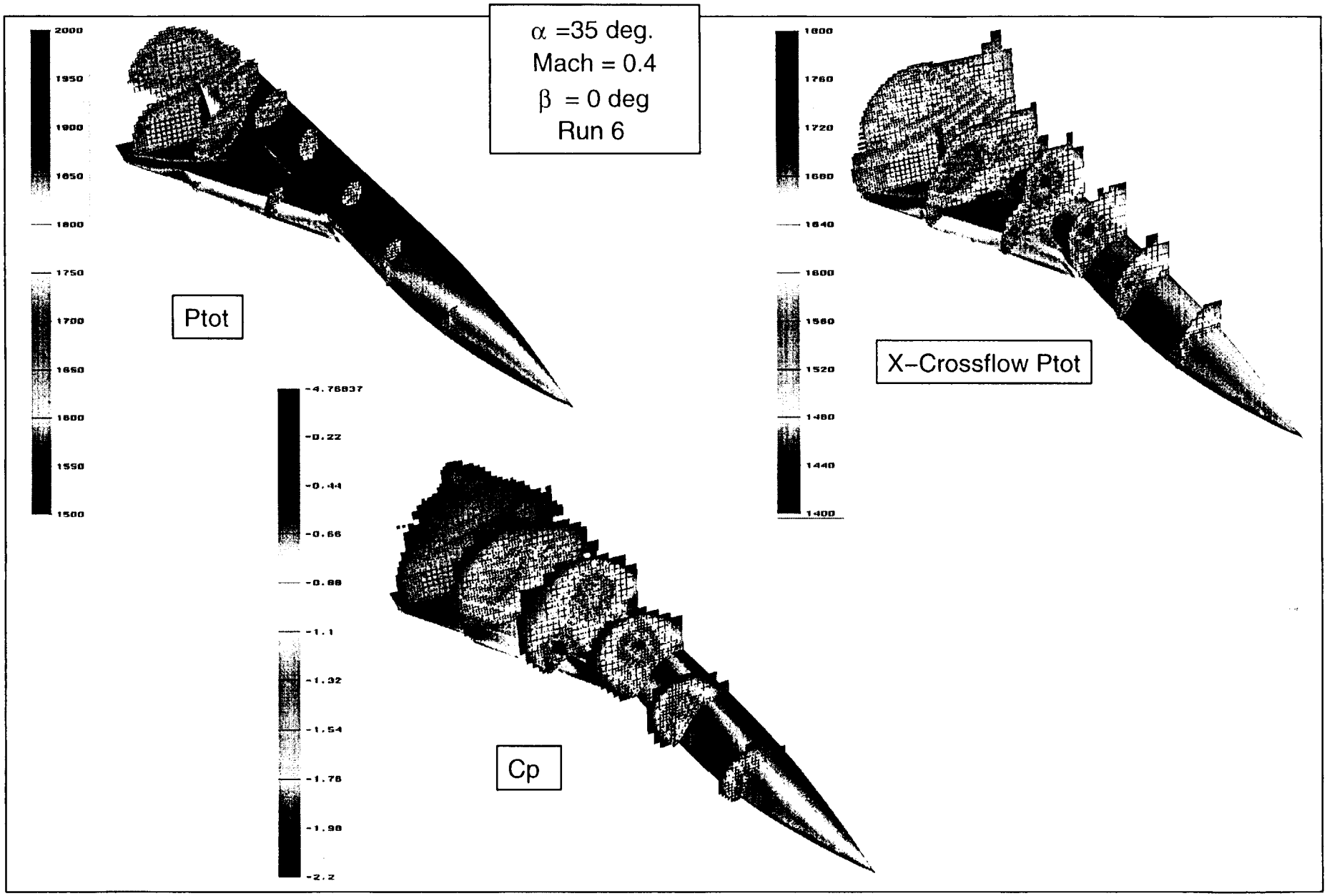

Figure 4.9. Use of Total Pressure Defined from X-Crossflow to Define Flowfield

ORIGINAL PAGE IS
OF POOR QUALITY

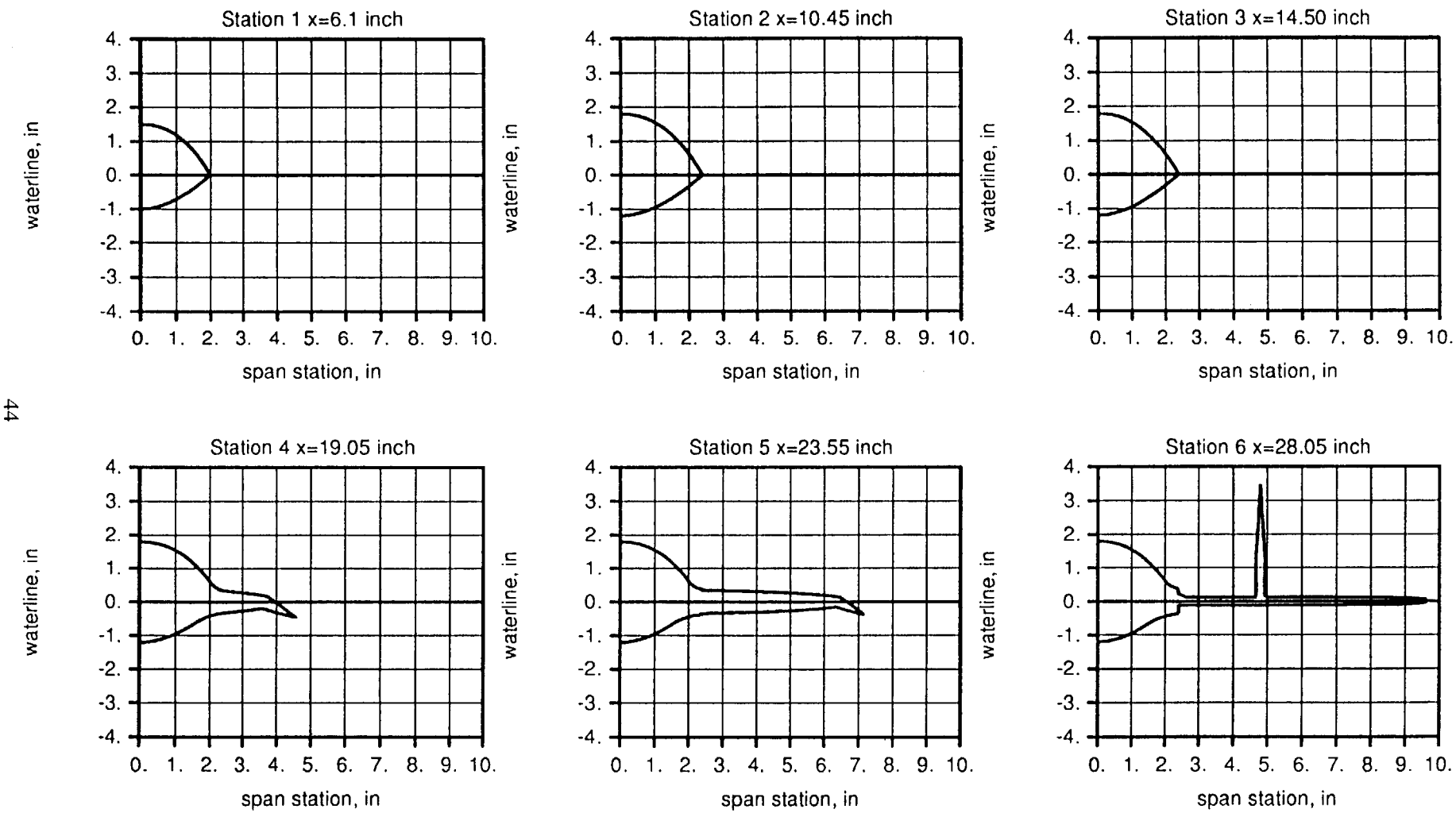

Figure 4.10. MTVI Fuselage Cut Geometry at Pressure Stations

Pathfinder X–Crossflow Total Pressure Comparison

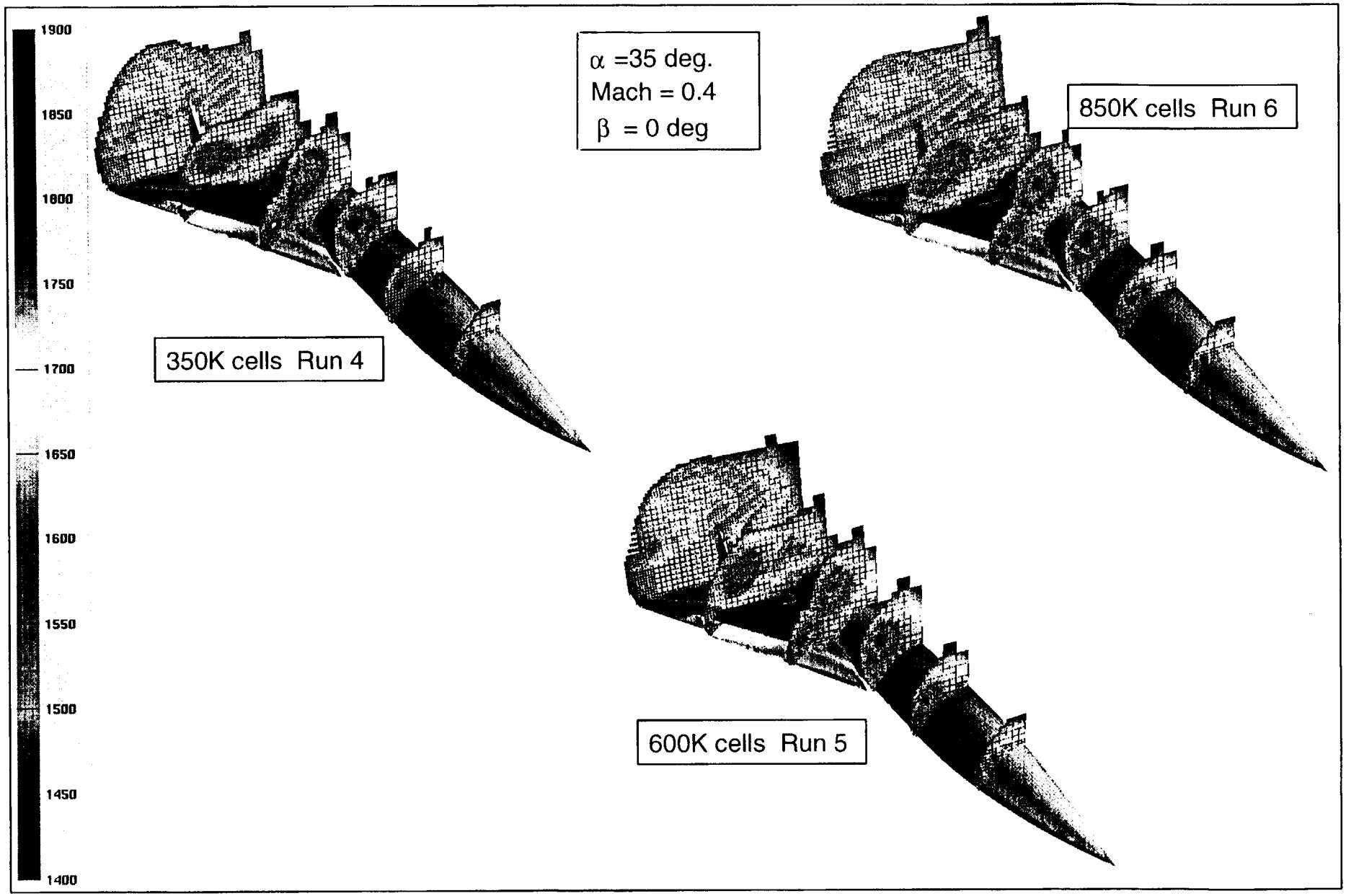

Figure 4.11. Pathfinder X-Crossflow Total Pressure Comparison

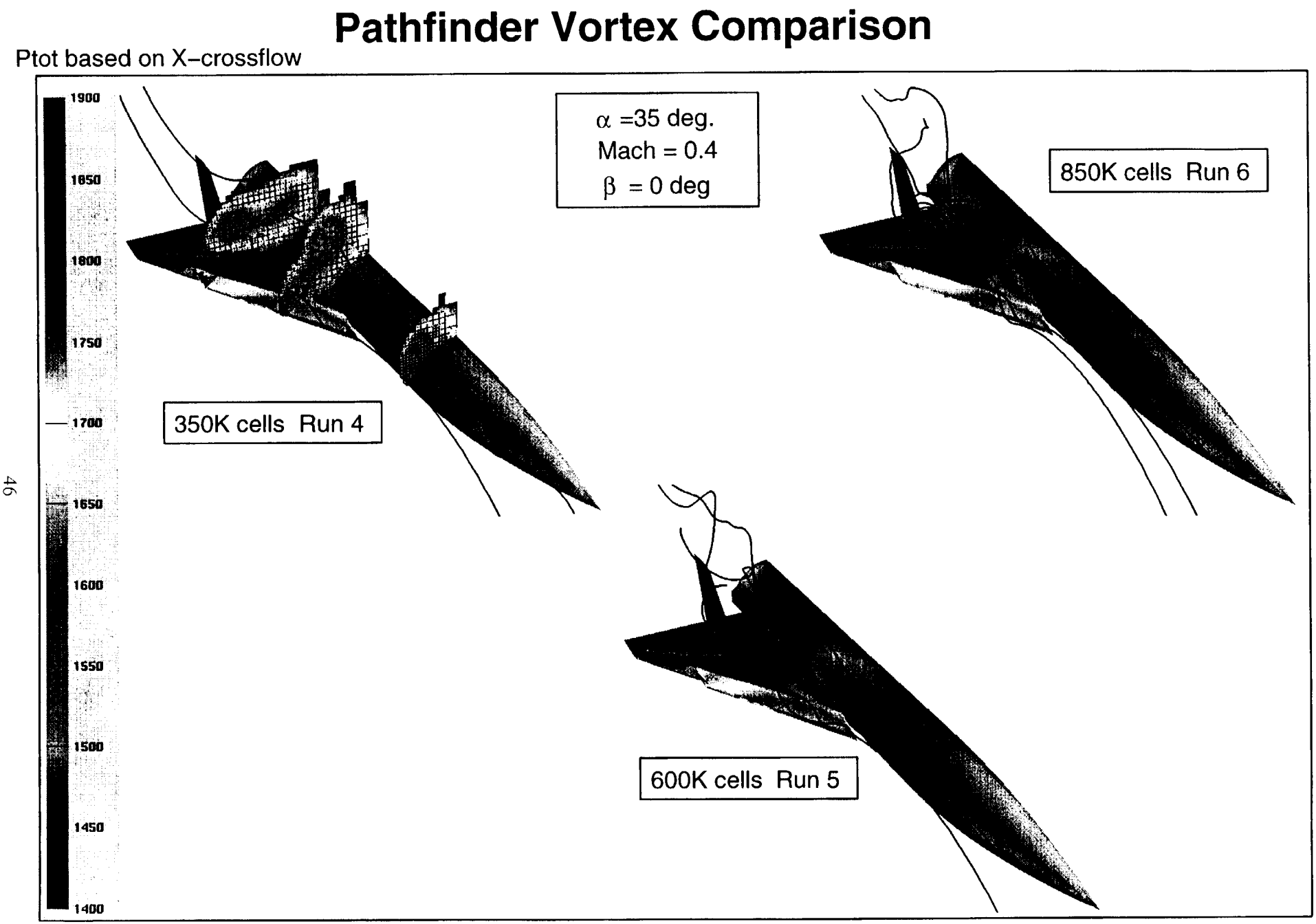

Figure 4.12. Pathfinder Vortex Comparison

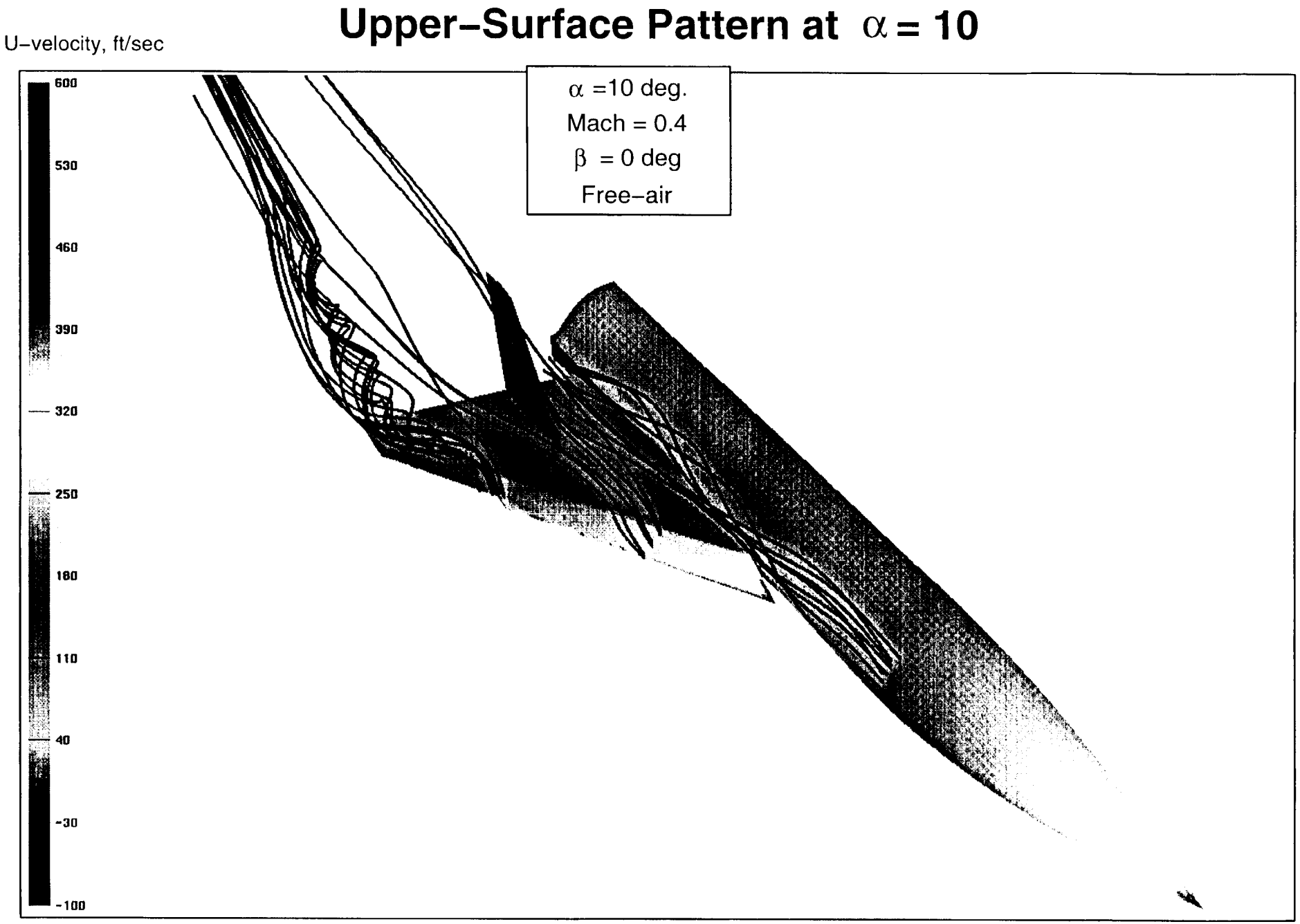

Figure 4.13. Upper-Surface Pattern at Aoa=10

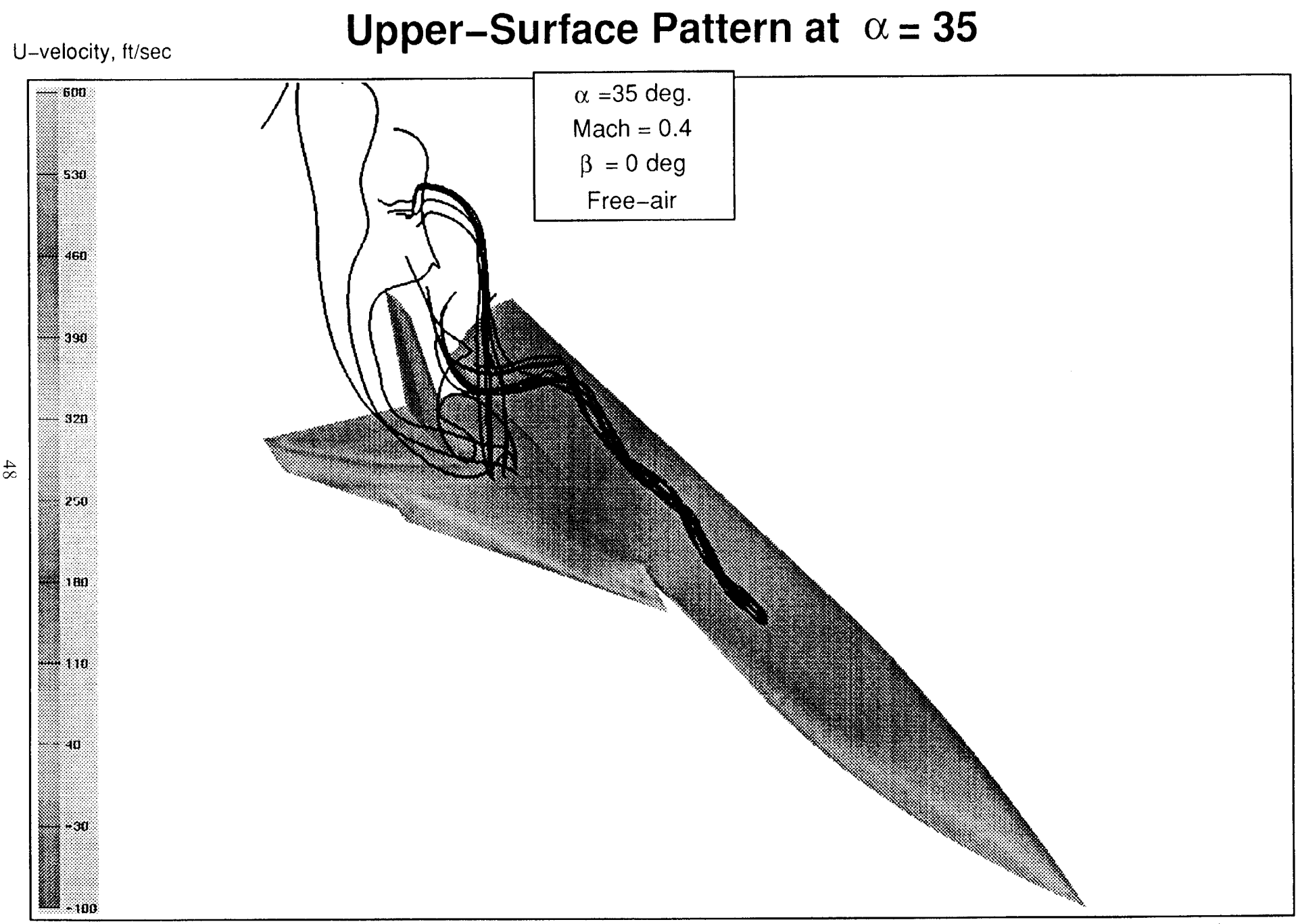

Figure 4.14. Upper-Surface Pattern at Aoa=35

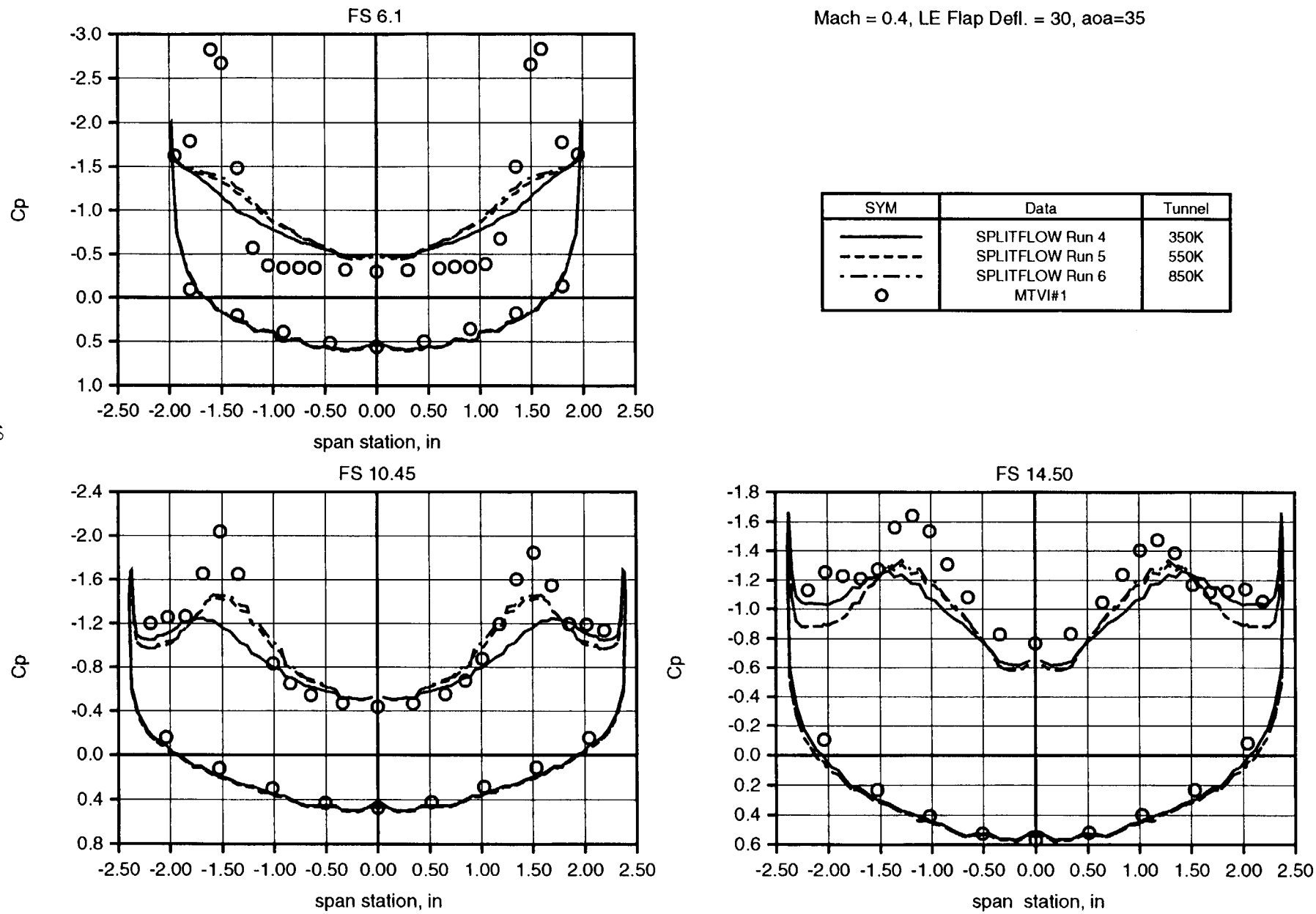

Figure 4.15. Effect of Grid Resolution on Forebody Pressures for MTVI#1

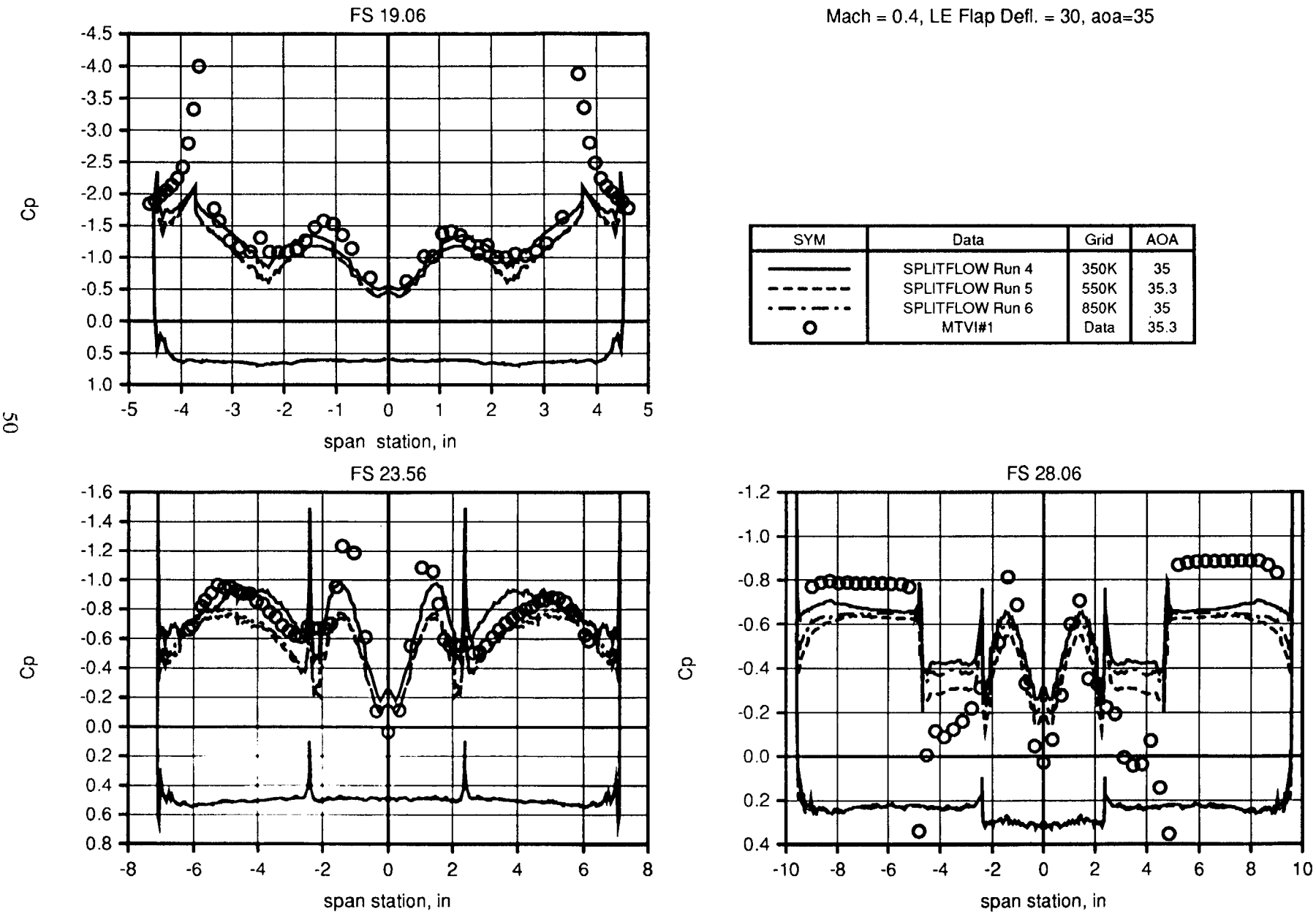

Figure 4.16. Effect of Grid Resolution on Wing Pressures for MTVI#1

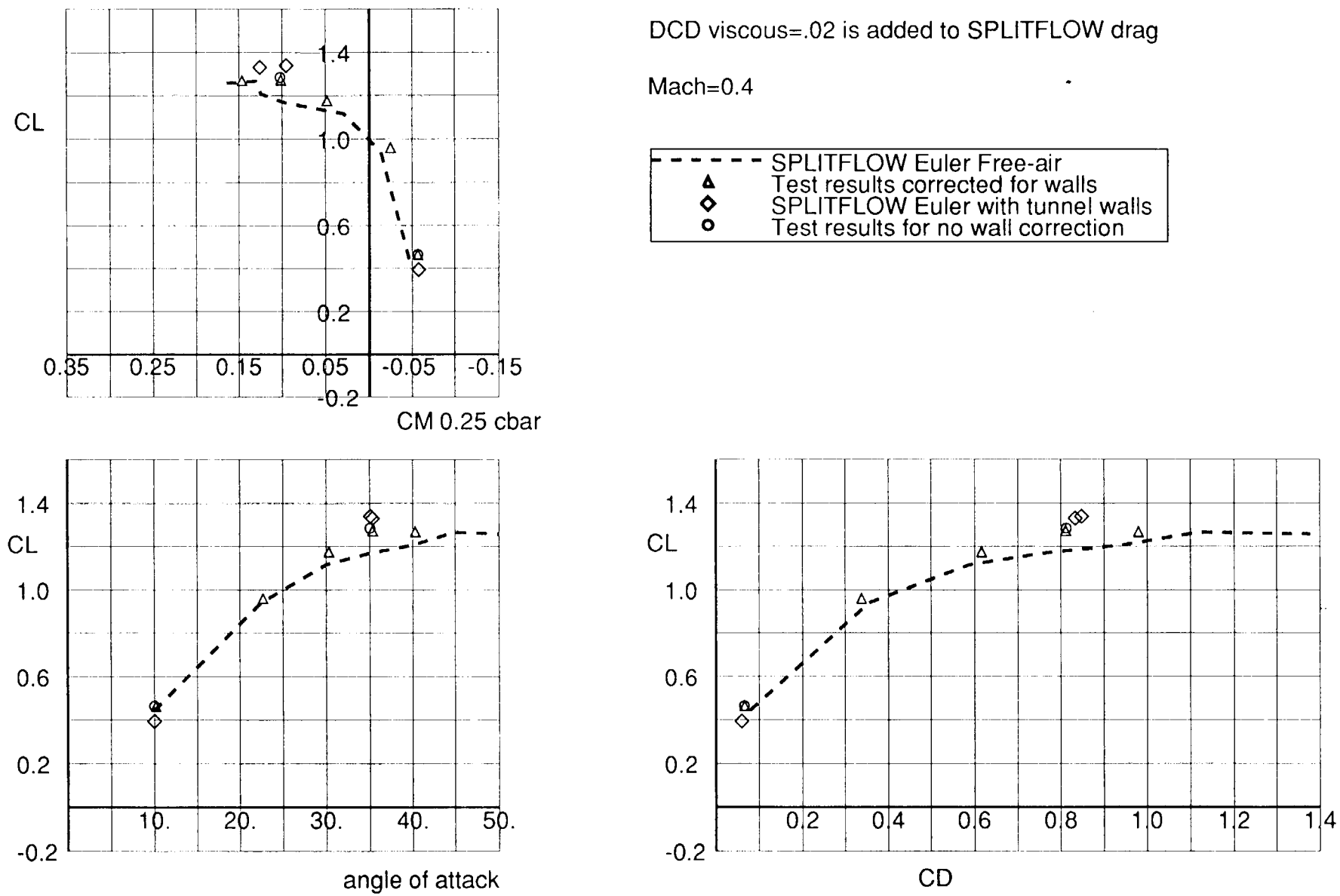

Figure 4.17. Aerodynamic Coefficients vs Test Data for MTVI#1

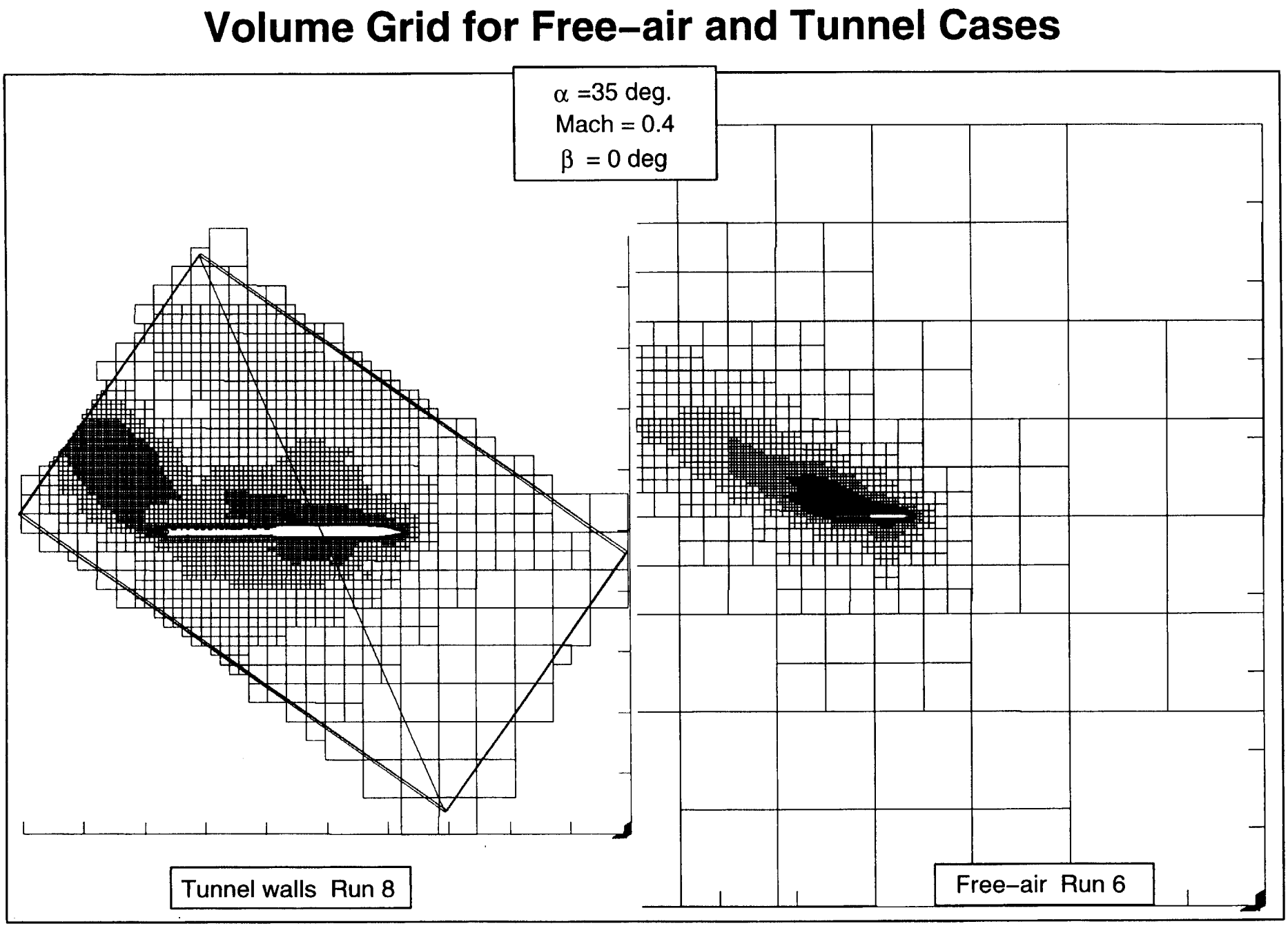

Figure 4.18. Volume Grid for Free-air and Tunnel Cases

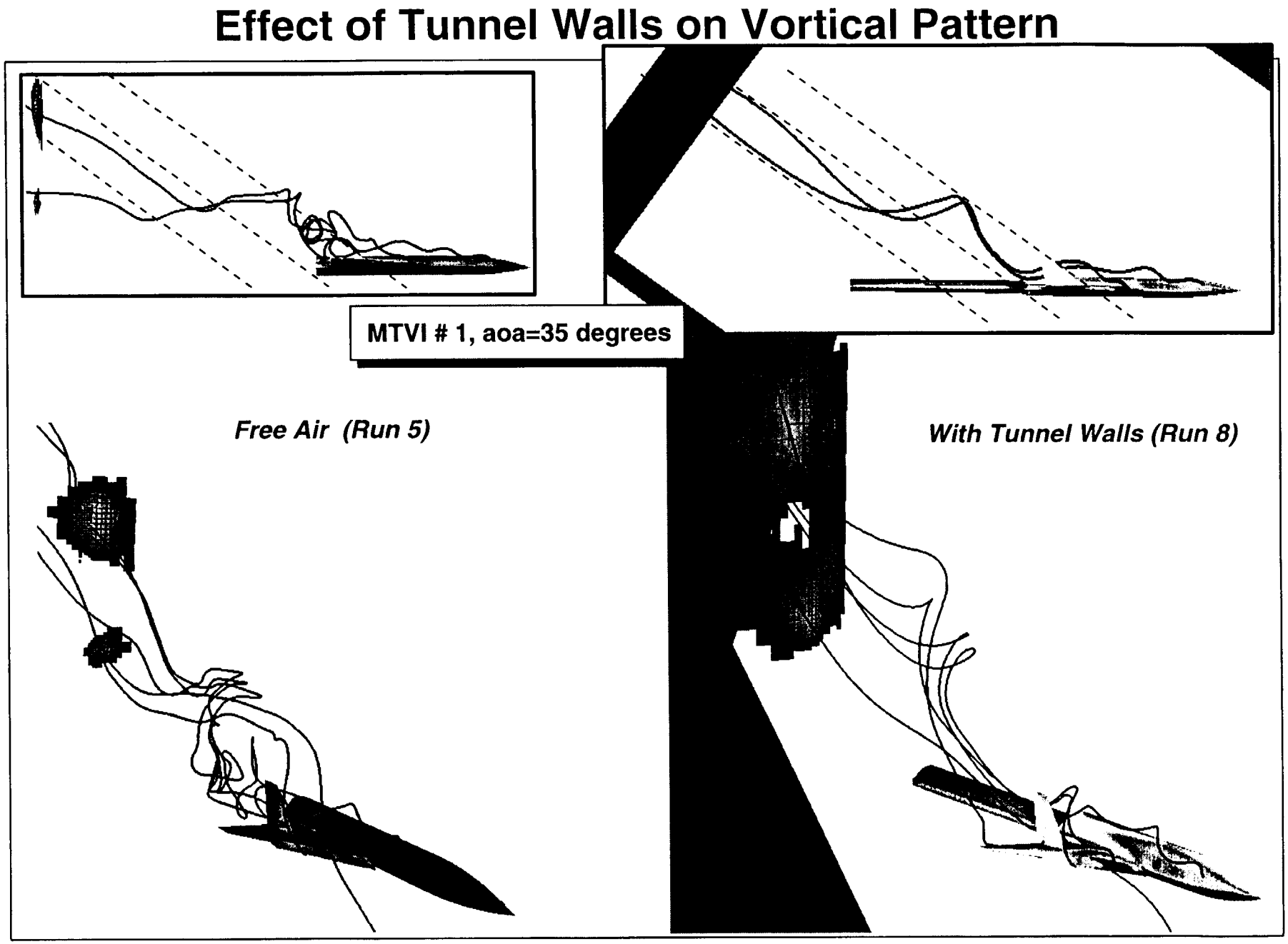

Figure 4.19. Effect of Tunnel Walls on Vortical Pattern

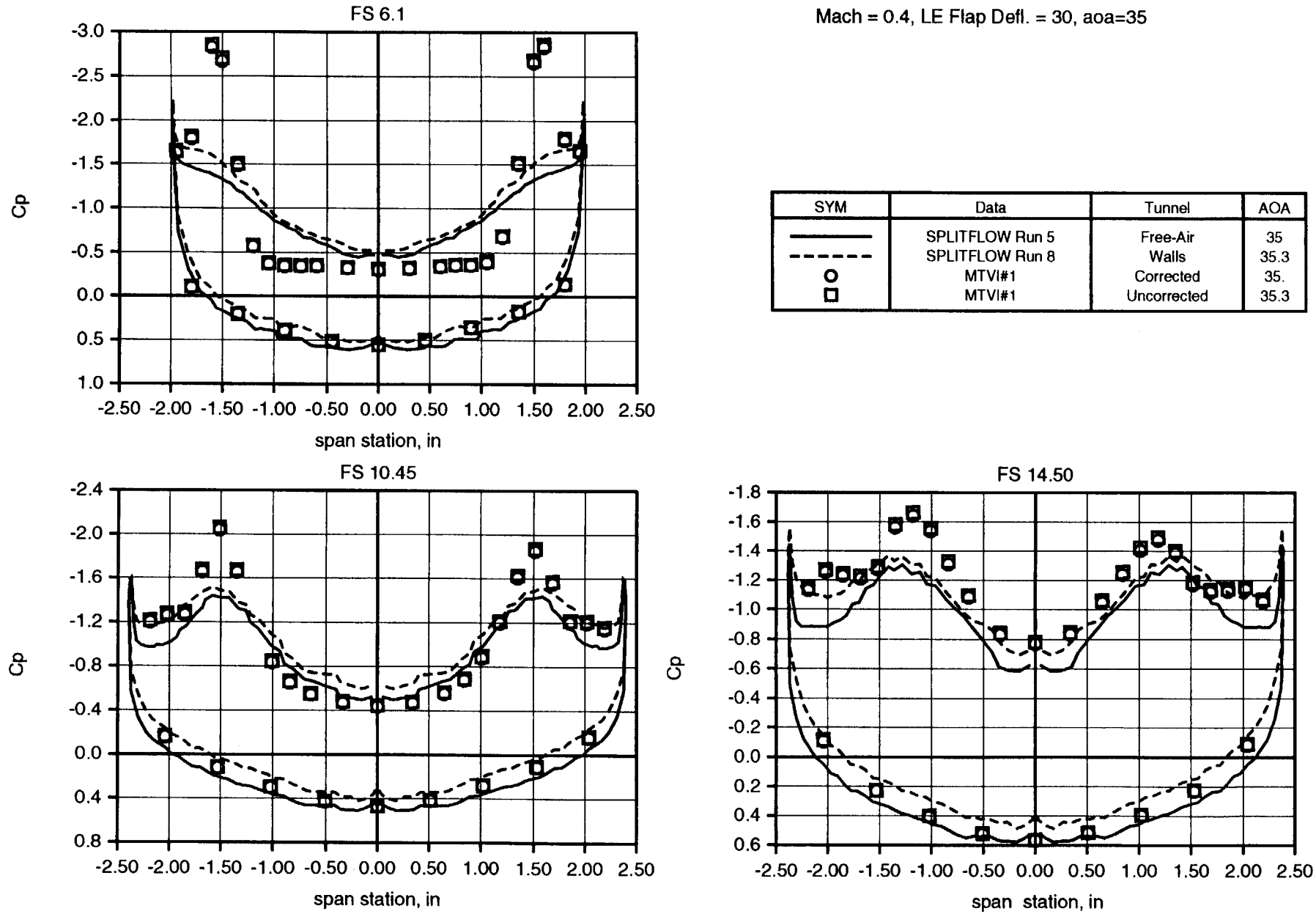

Figure 4.20. Forebody Pressures for MTVI#1 Tunnel and Free-Air

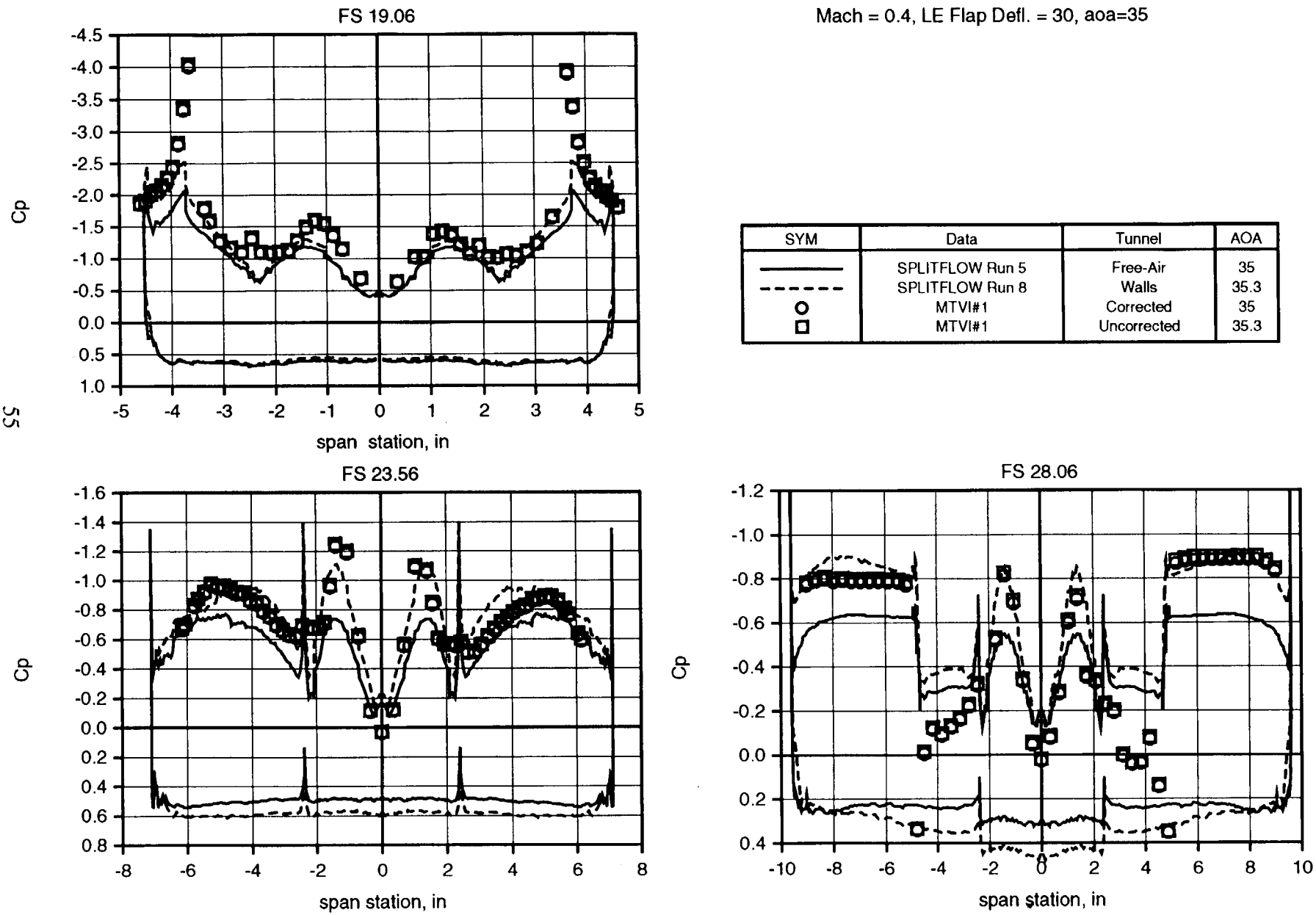

Figure 4.21. Wing Pressures for MTVI#1 Tunnel and Free-Air

Vortex Burst Movement versus Iteration at $\alpha = 35$

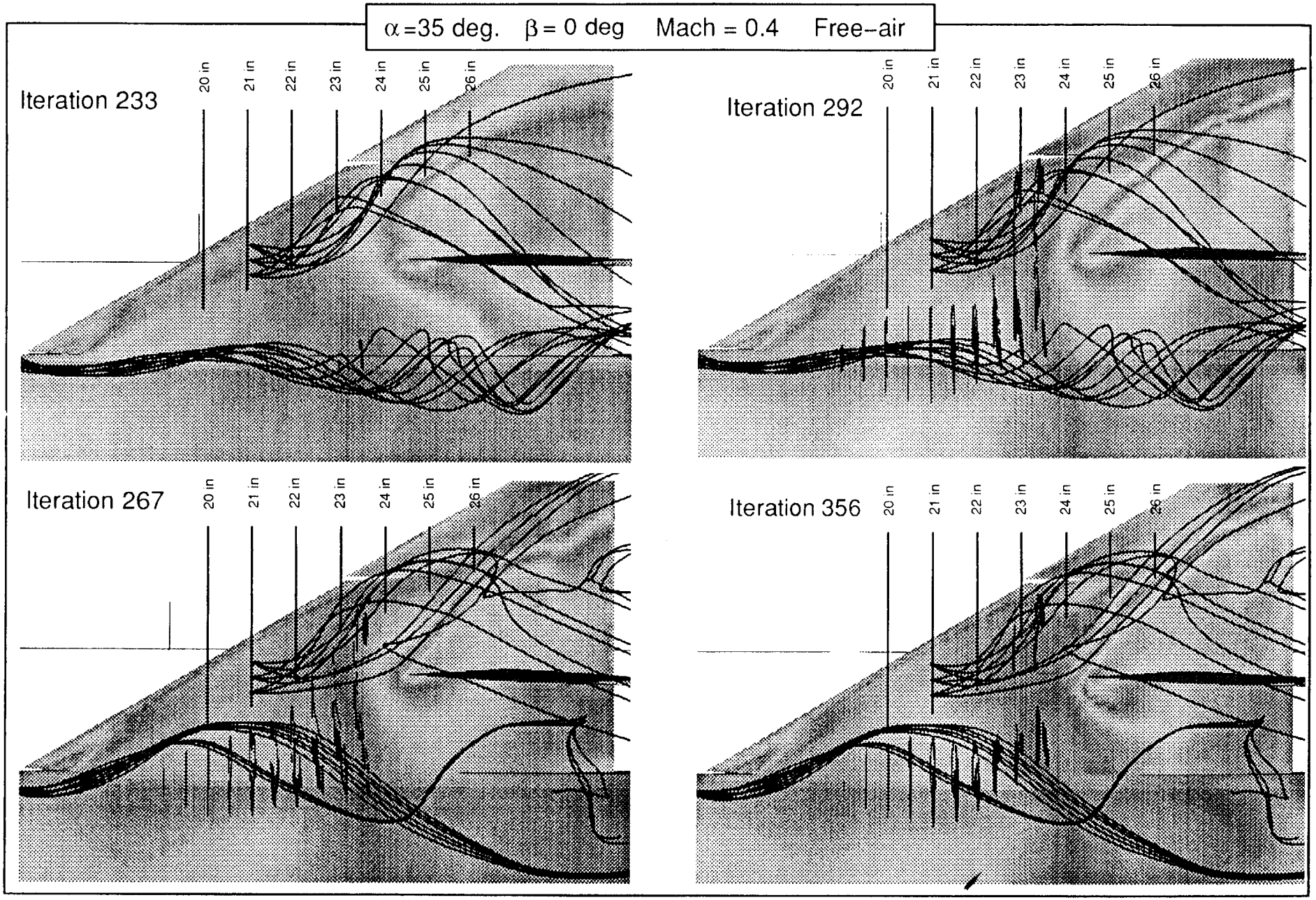

Figure 4.22. Vortex Burst Location for Several Steps of Solution, Aoa=35

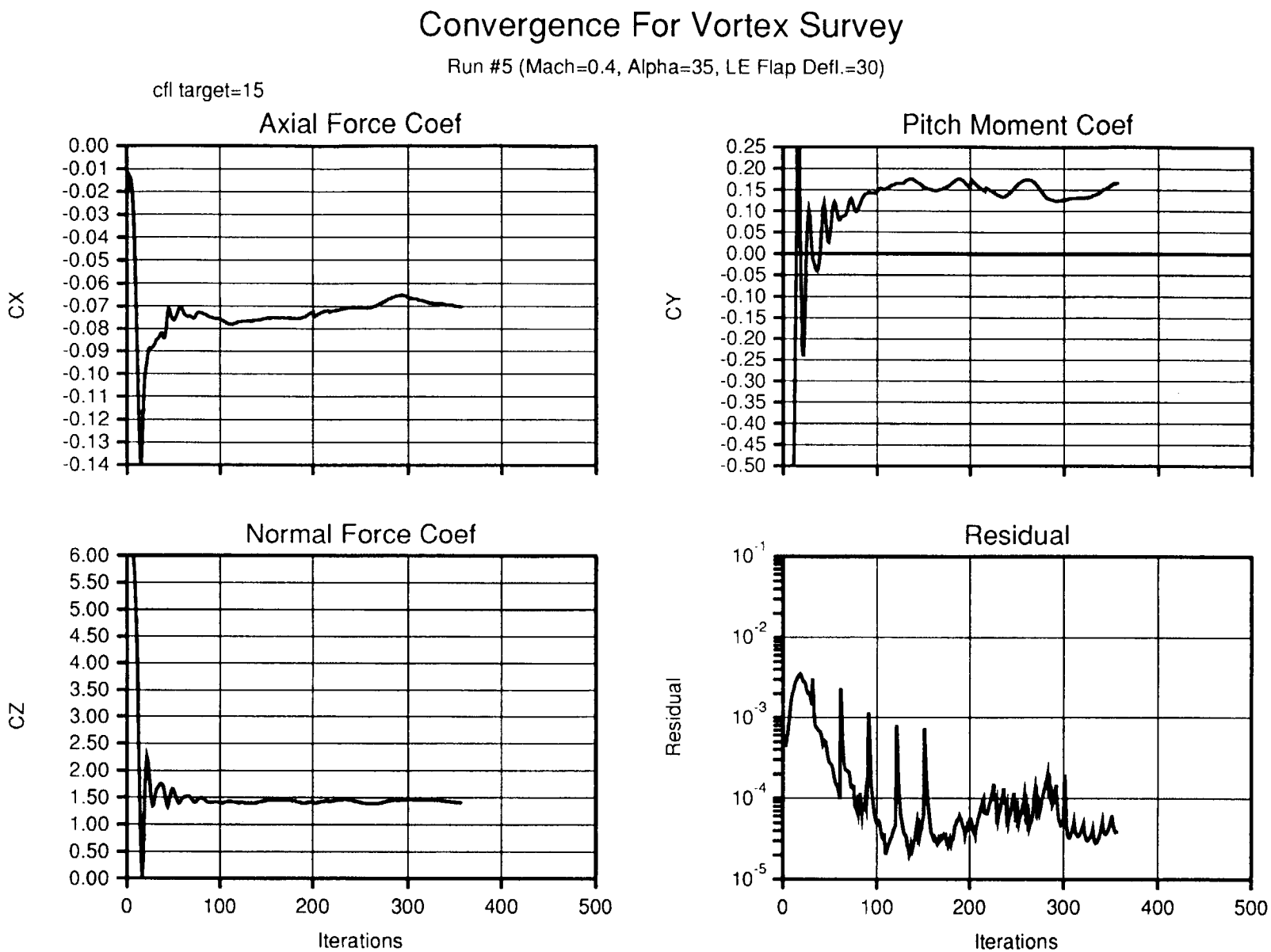

Figure 4.23. Lift and Pitching Moment for Vortex Burst Case, Aoa=35

Effect of Angle of Attack on Pressure Coefficient

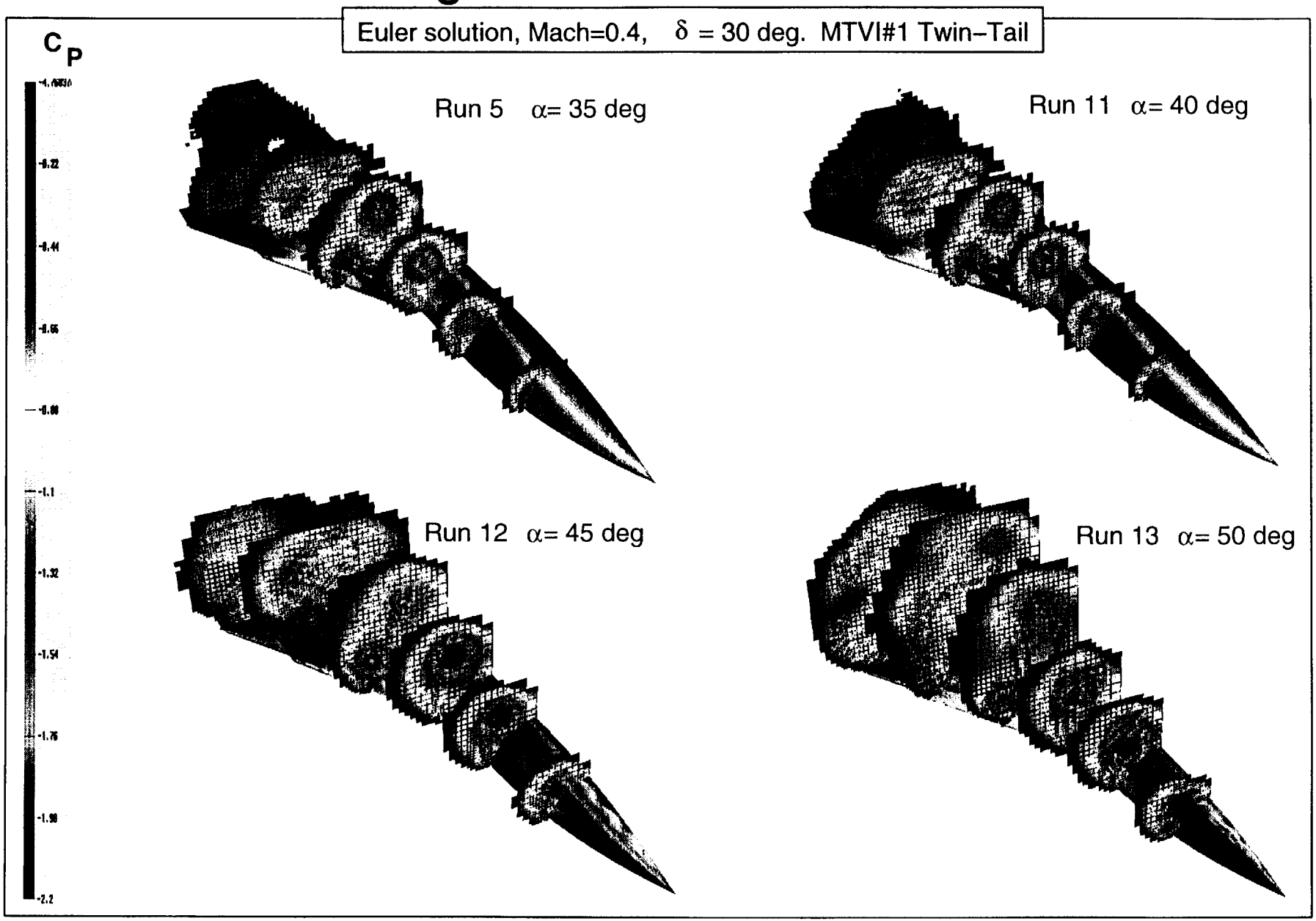

Figure 5.1. Effect of High AOA on Off-Body Pressure Coefficient

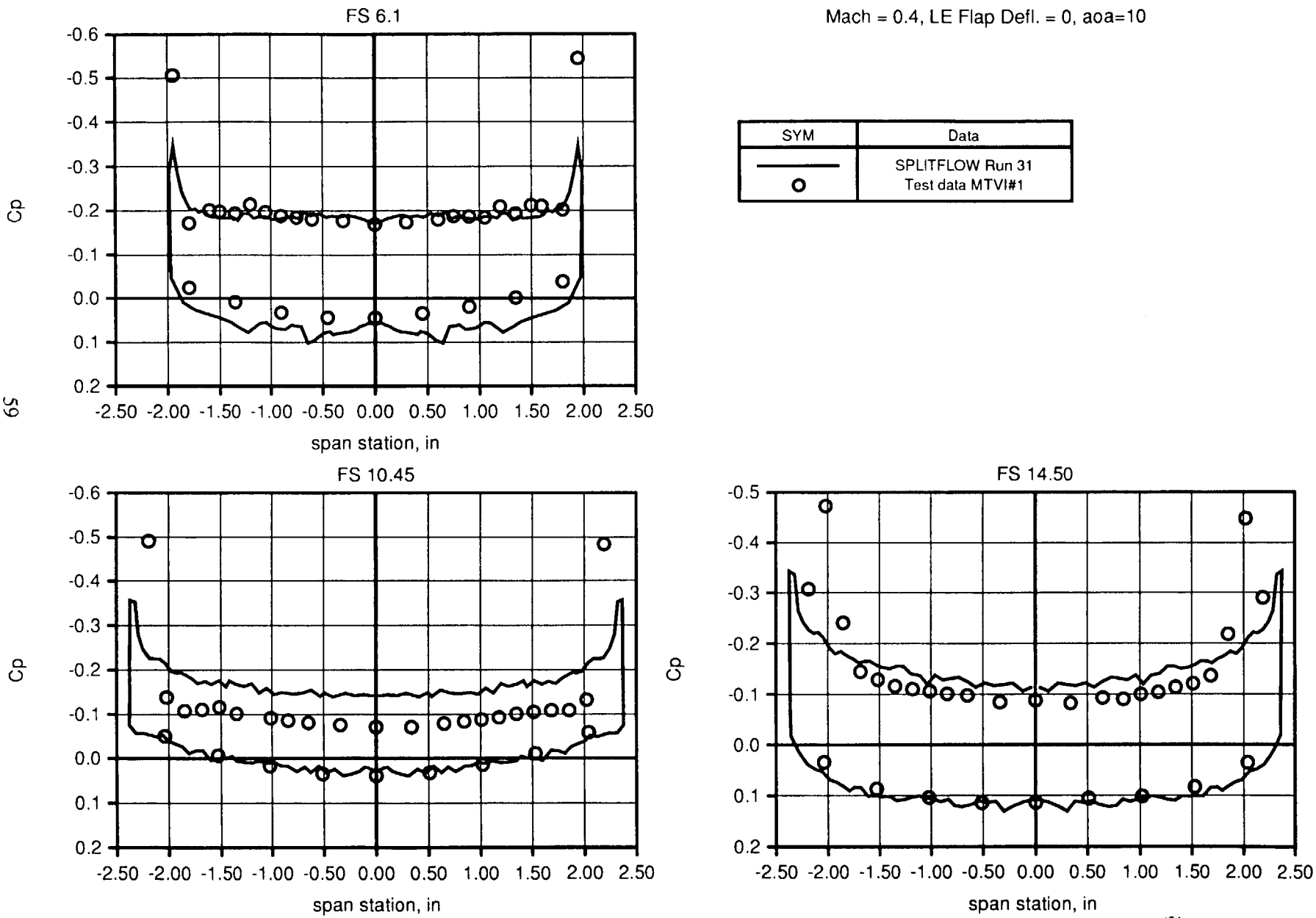

Figure 5.2. Forebody Pressures for MTVI#1 With Zero-LEF, Aoa=10

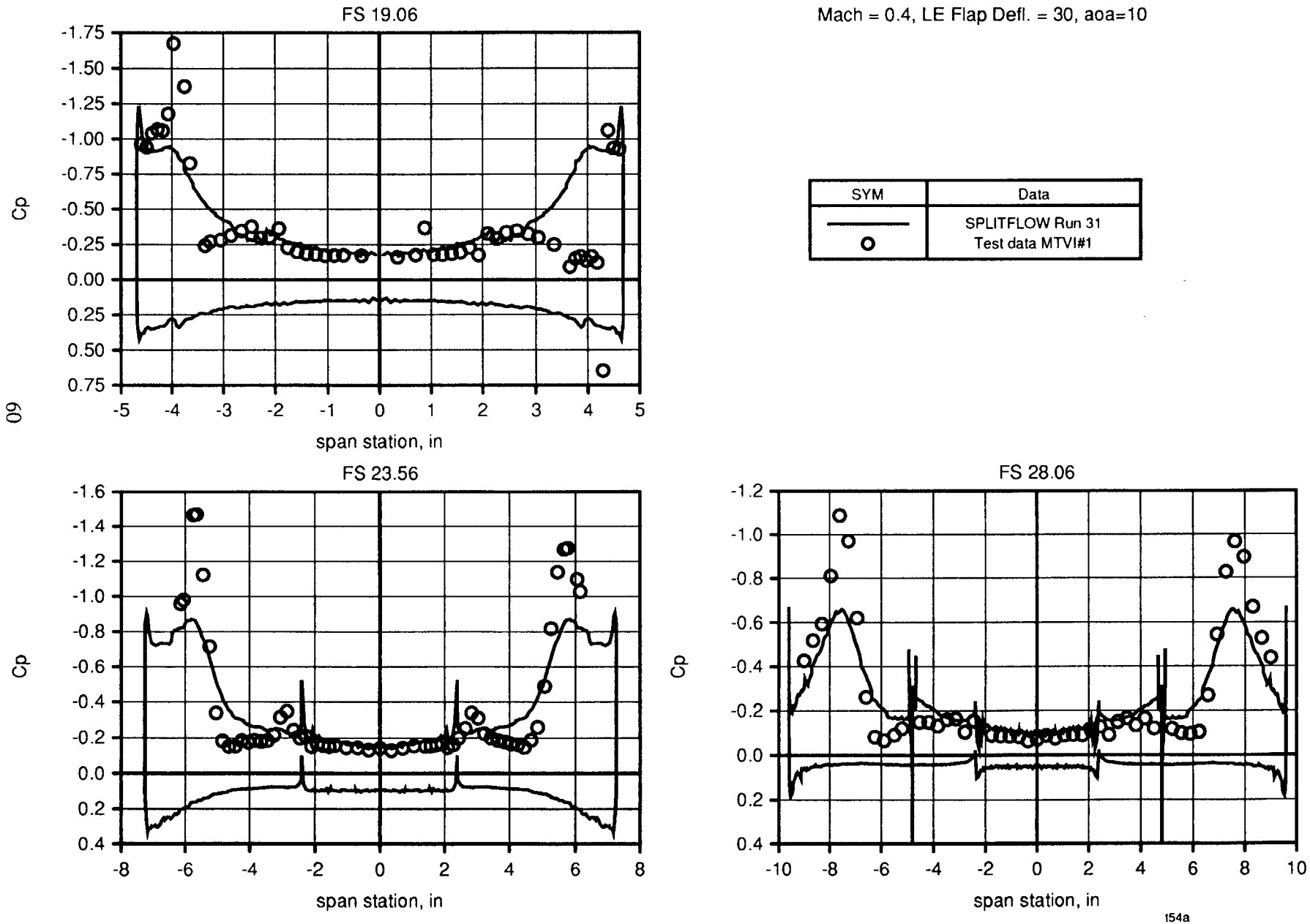

Figure 5.3. Wing Pressures for MTVI#1 With Zero-LEF, Aoa=10

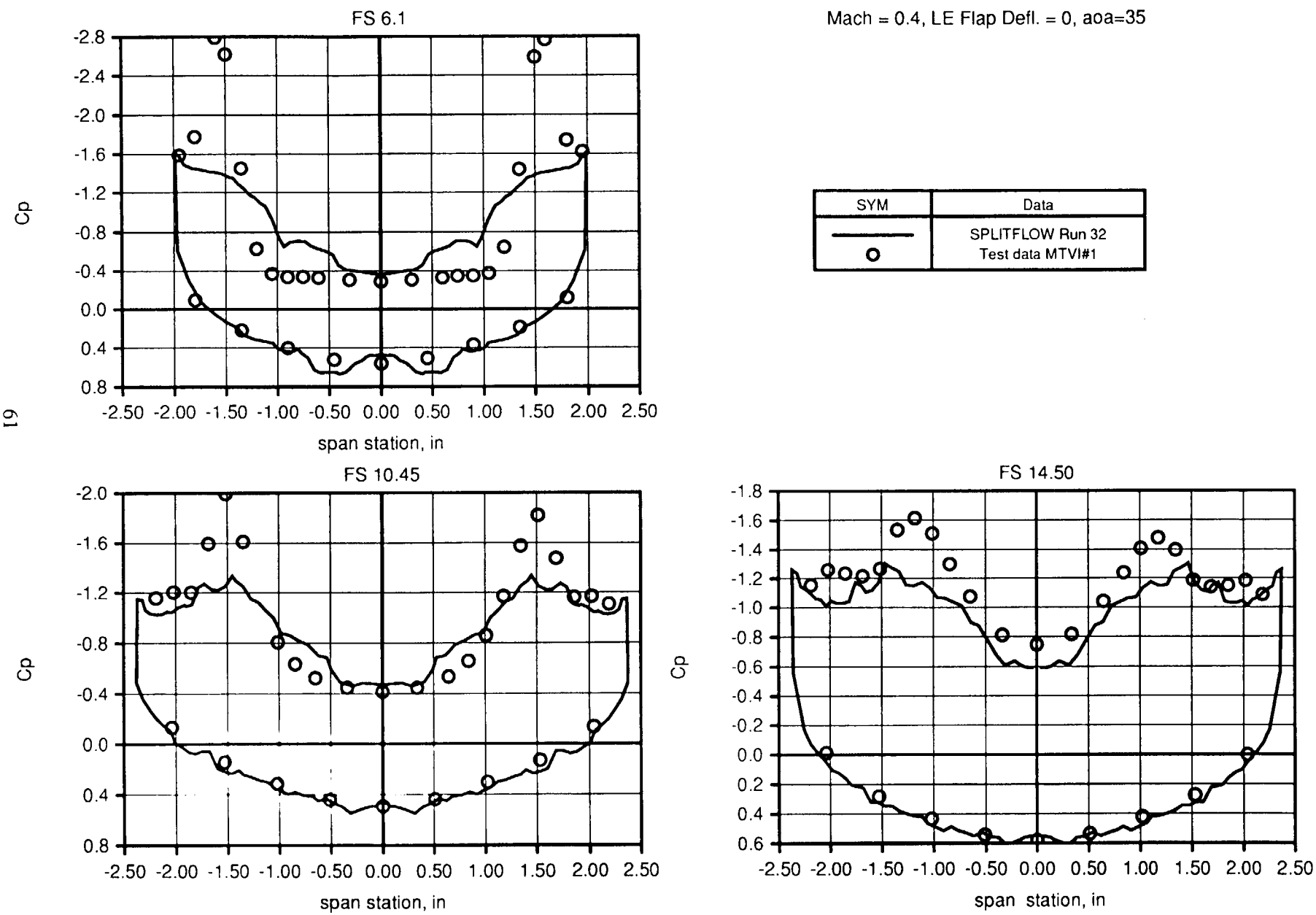

Figure 5.4. Forebody Pressures for MTVI#1 With Zero-LEF, Aoa=35

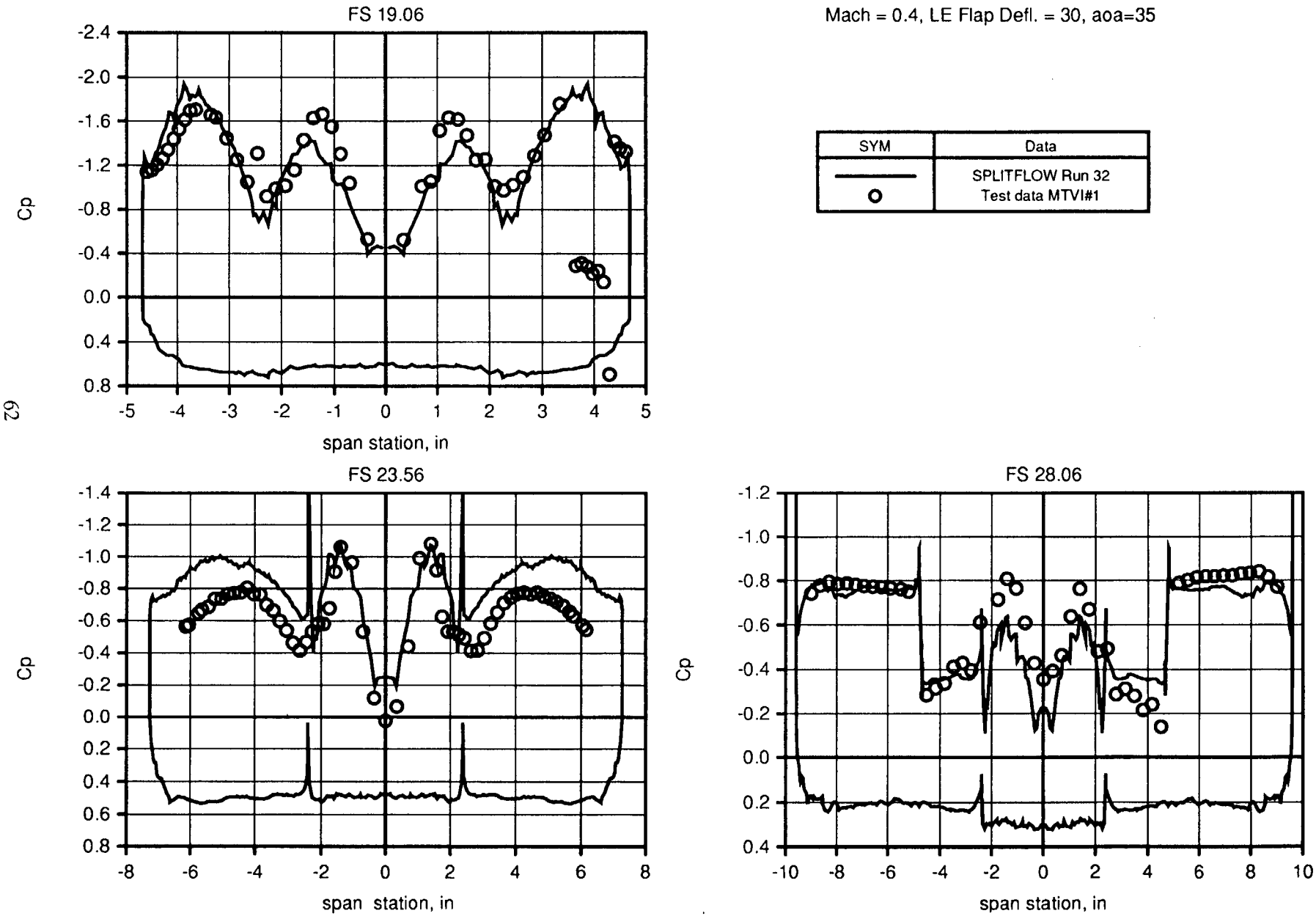

Figure 5.5. Wing Pressures for MTVI#1 With Zero-LEF, Aoa=35

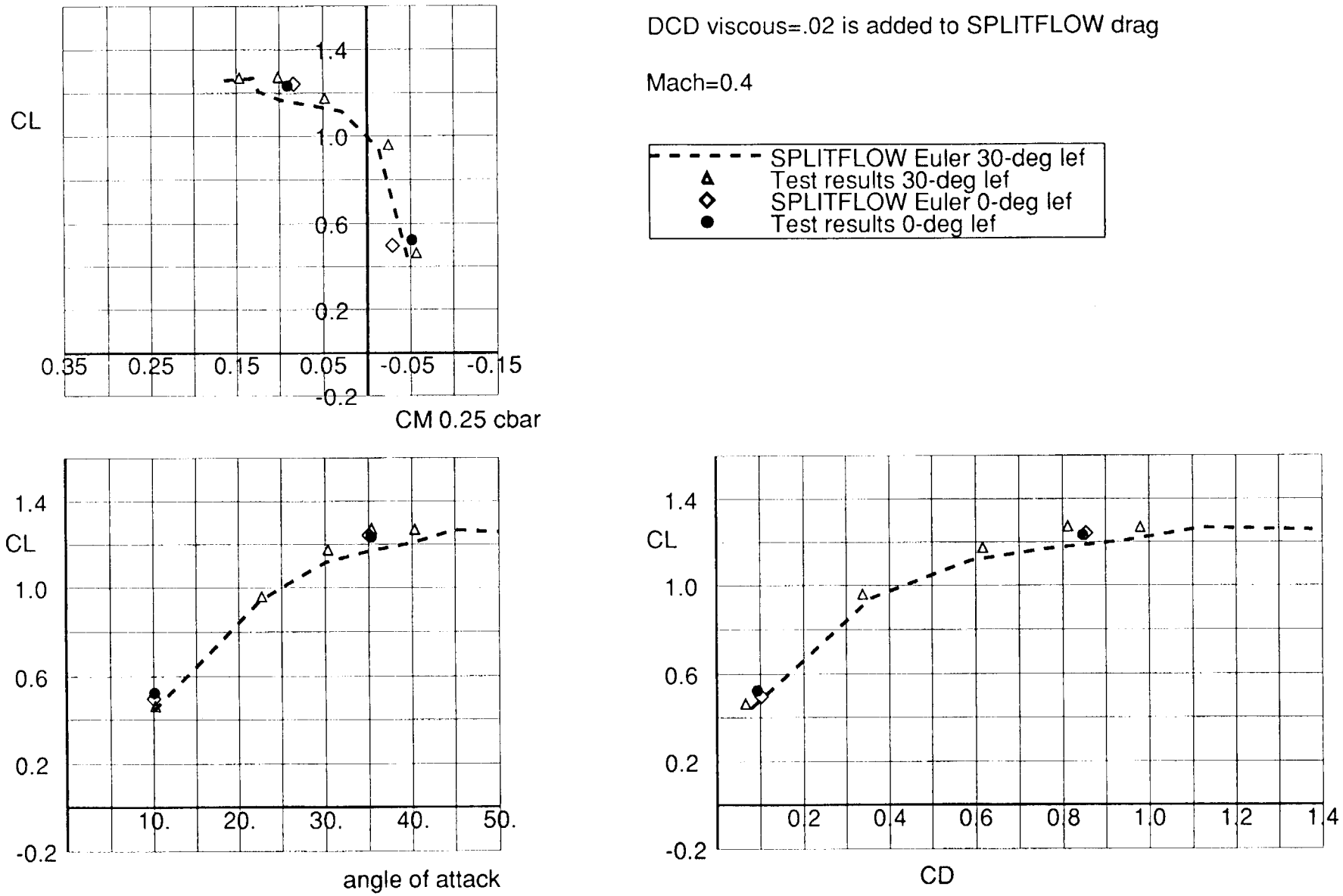

Figure 5.6. Aerodynamic Coefficients vs Test data for Zero-LEF

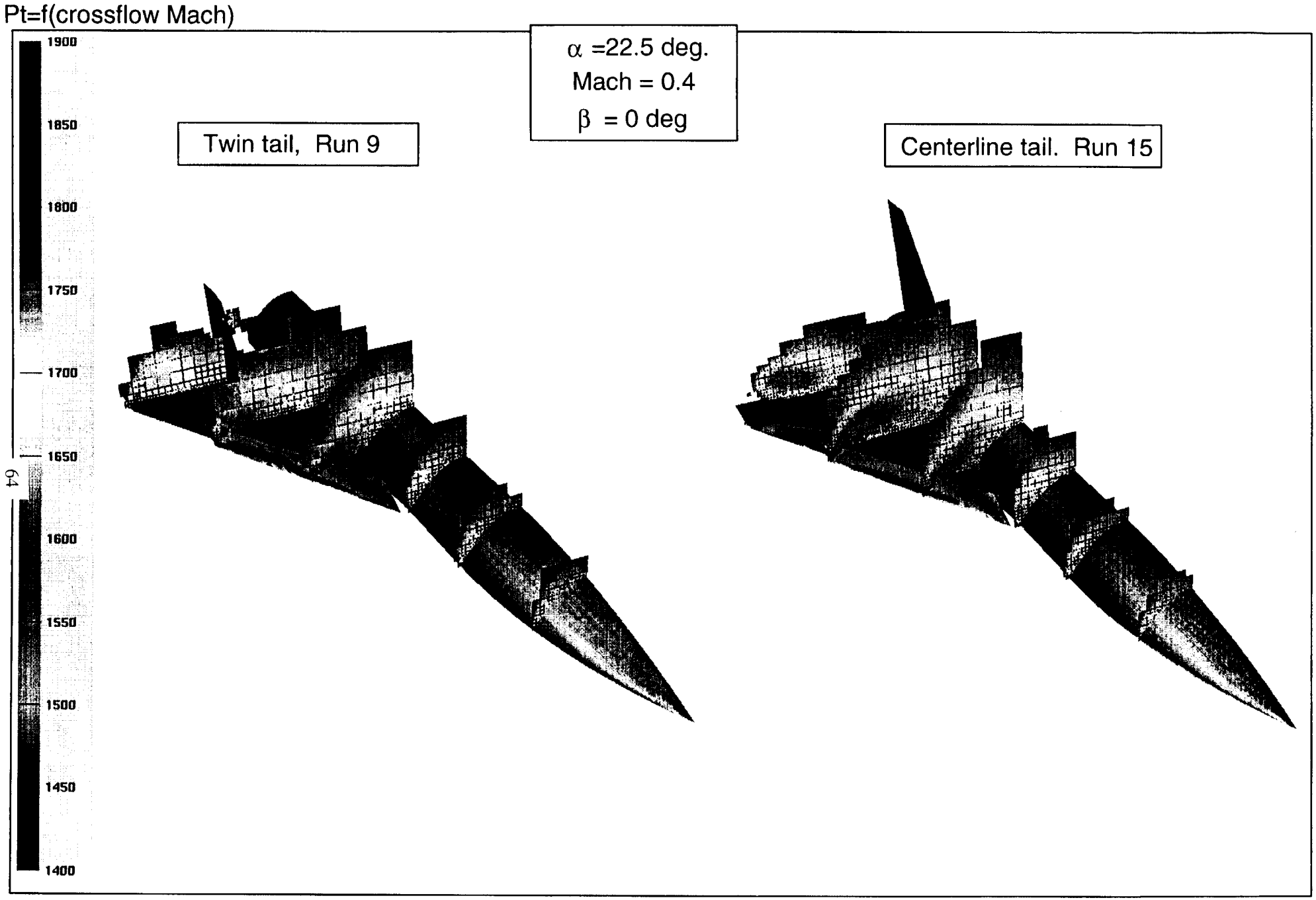

Figure 5.7. Effect of Tail Arrangement on X-Crossflow Total Pressure, Aoa=22.5

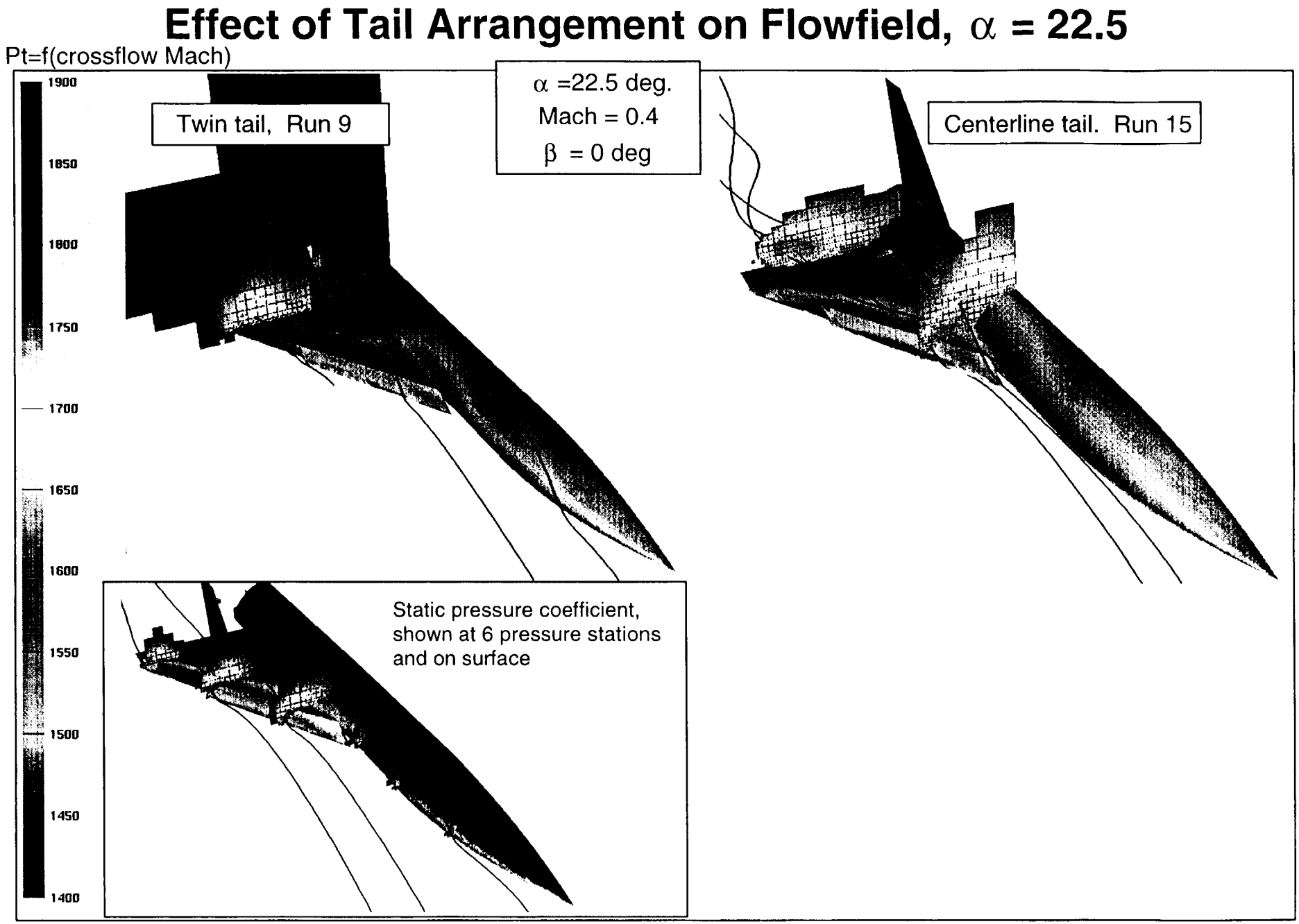

Figure 5.8. Effect of Tail Arrangement on Flowfield, Aoa=22.5

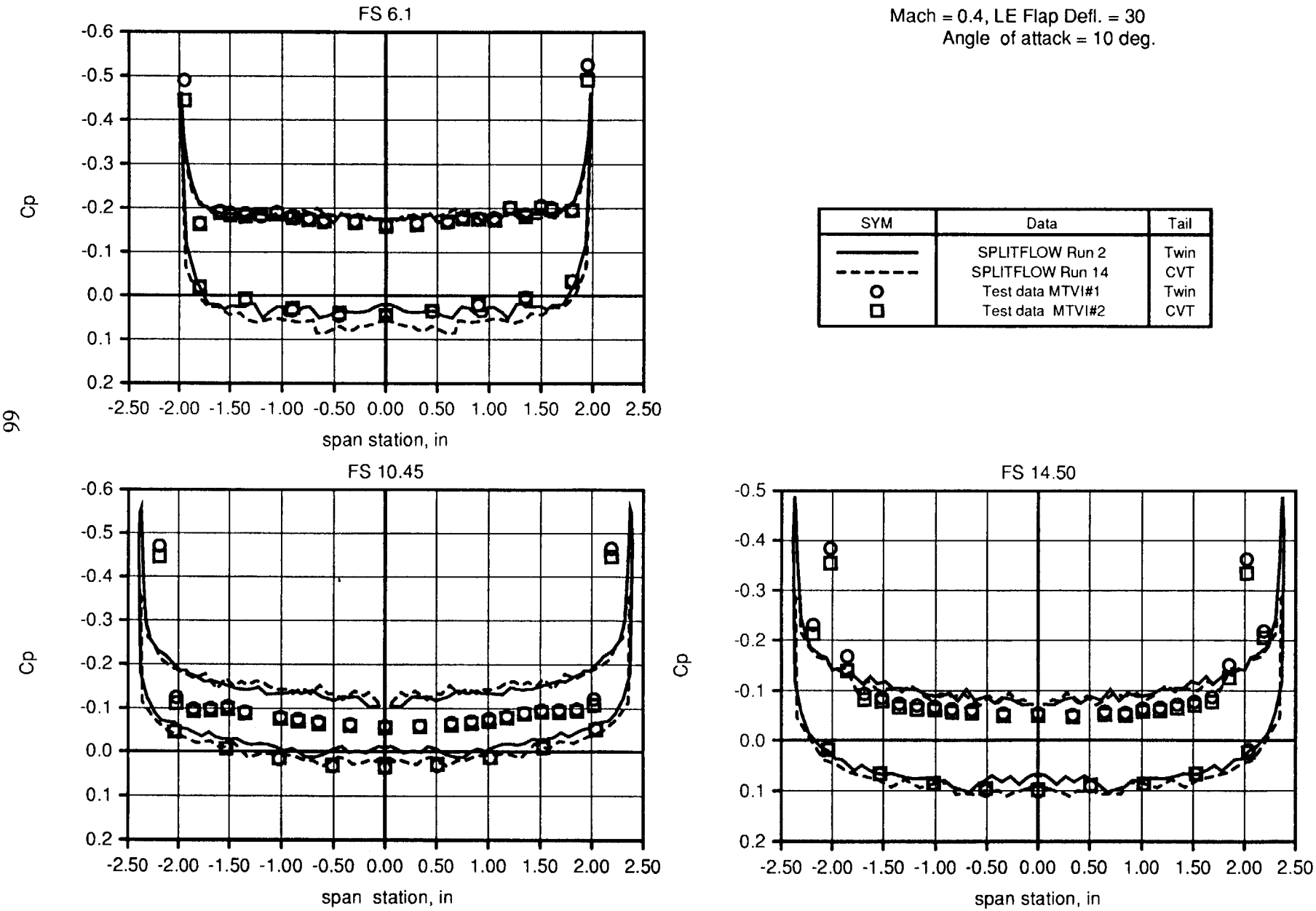

Figure 5.9. Forebody Pressures for Tail Placement, Aoa=10

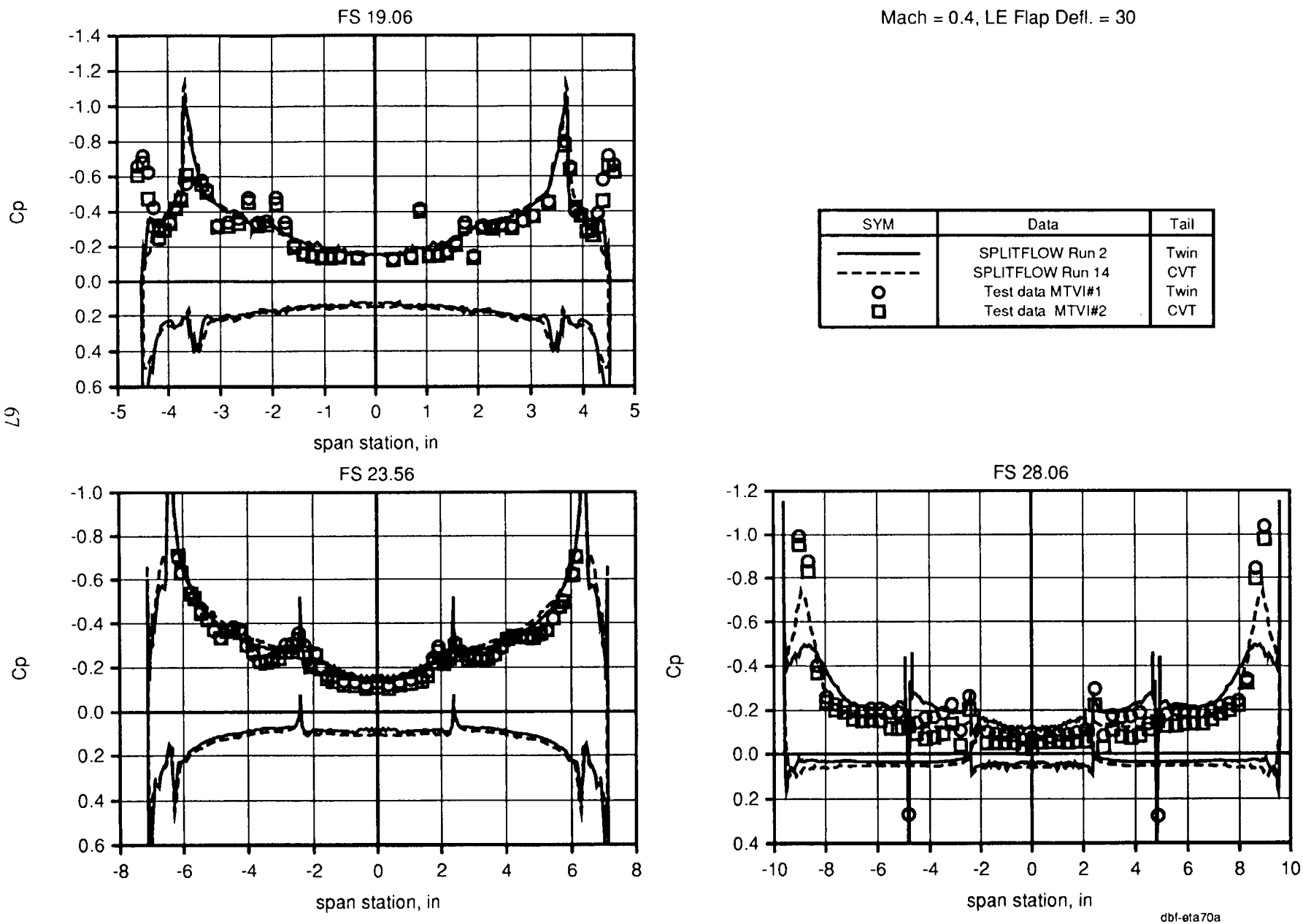

Figure 5.10. Wing Pressures for Tail Placement, Aoa=10

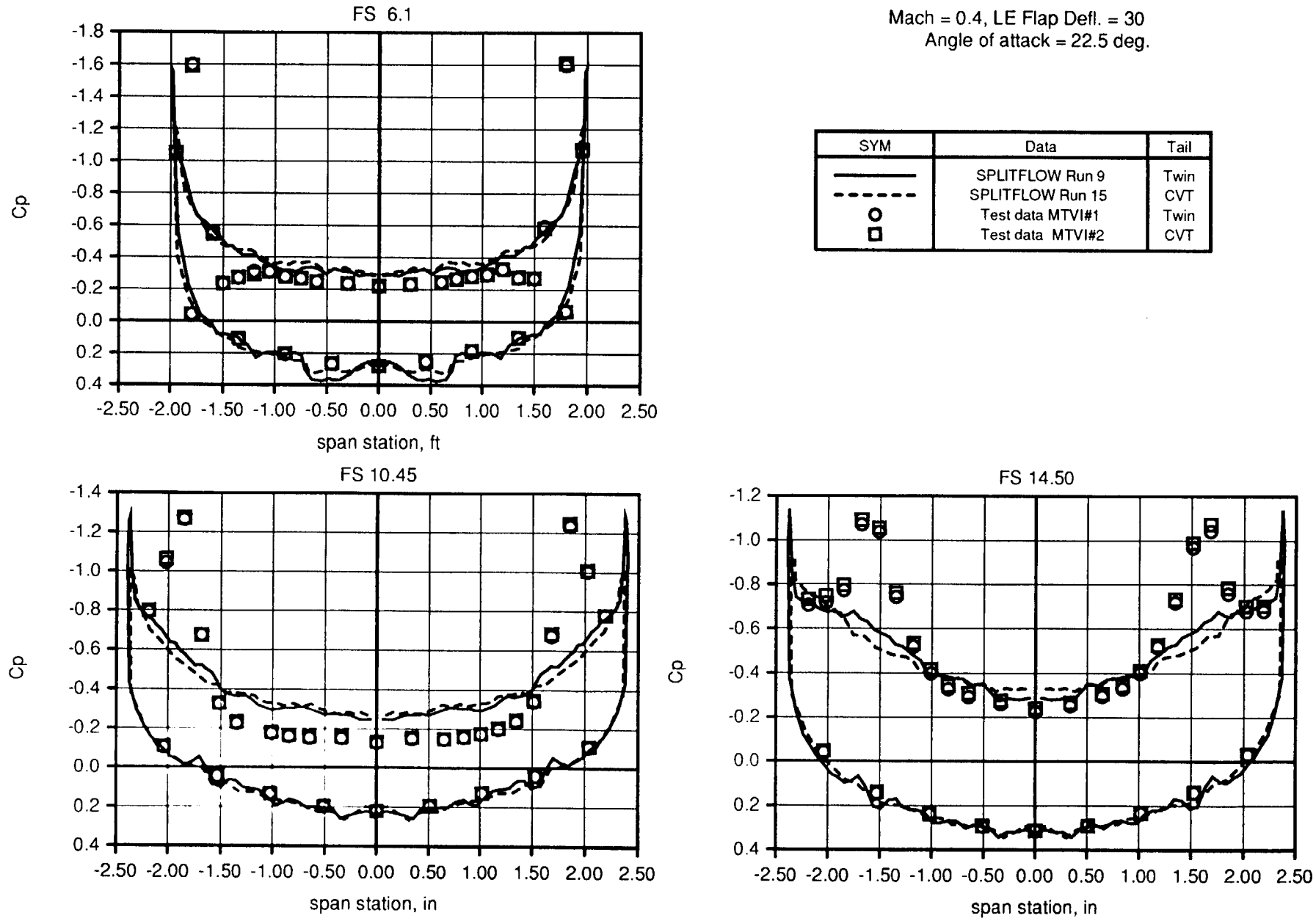

Figure 5.11. Forebody Pressures for Tail Placement, Aoa=22.5

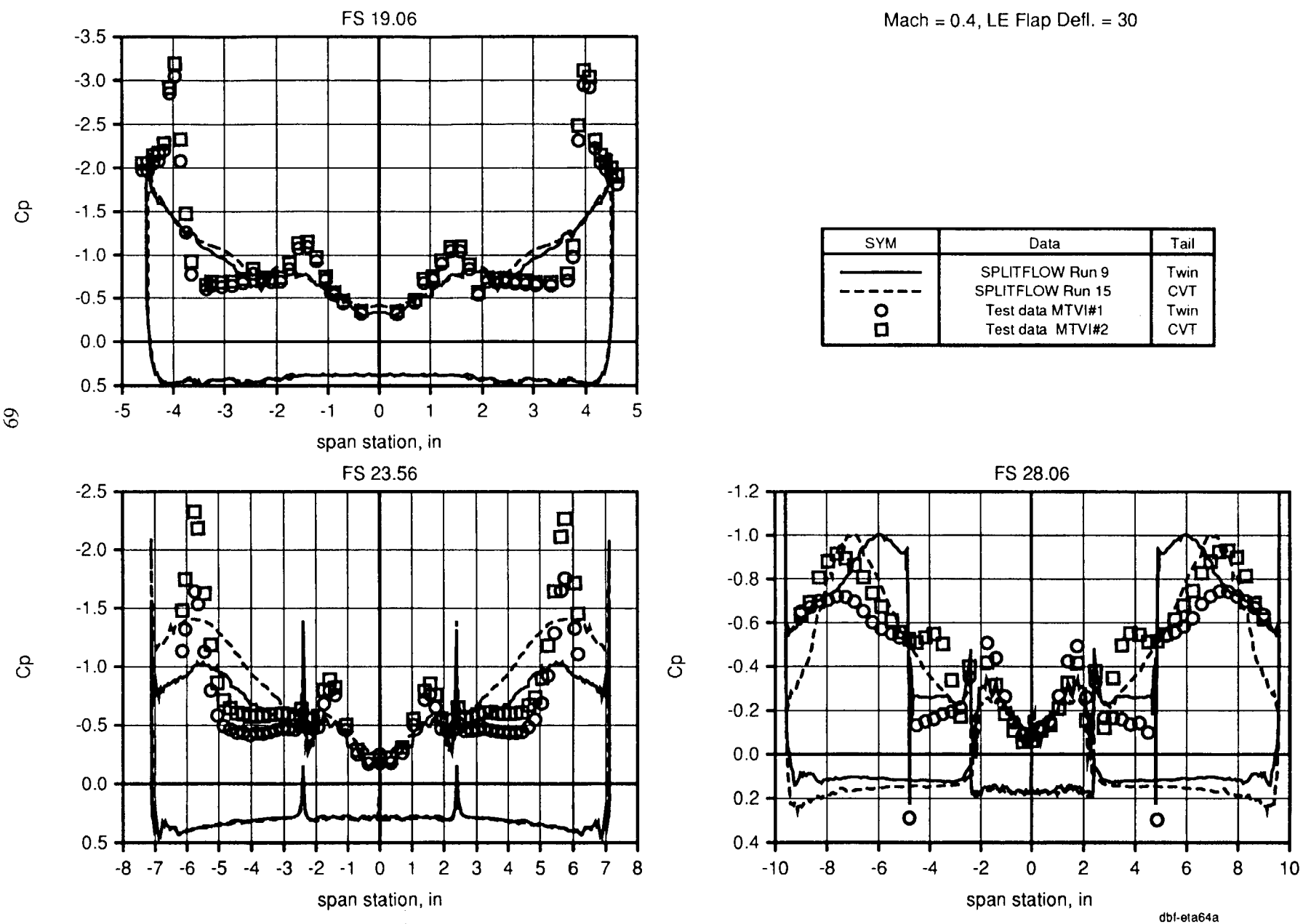

Figure 5.12. Wing Pressures for Tail Placement, Aoa=22.5

Effect of Tail Arrangement on X crossflow Pt, α = 35

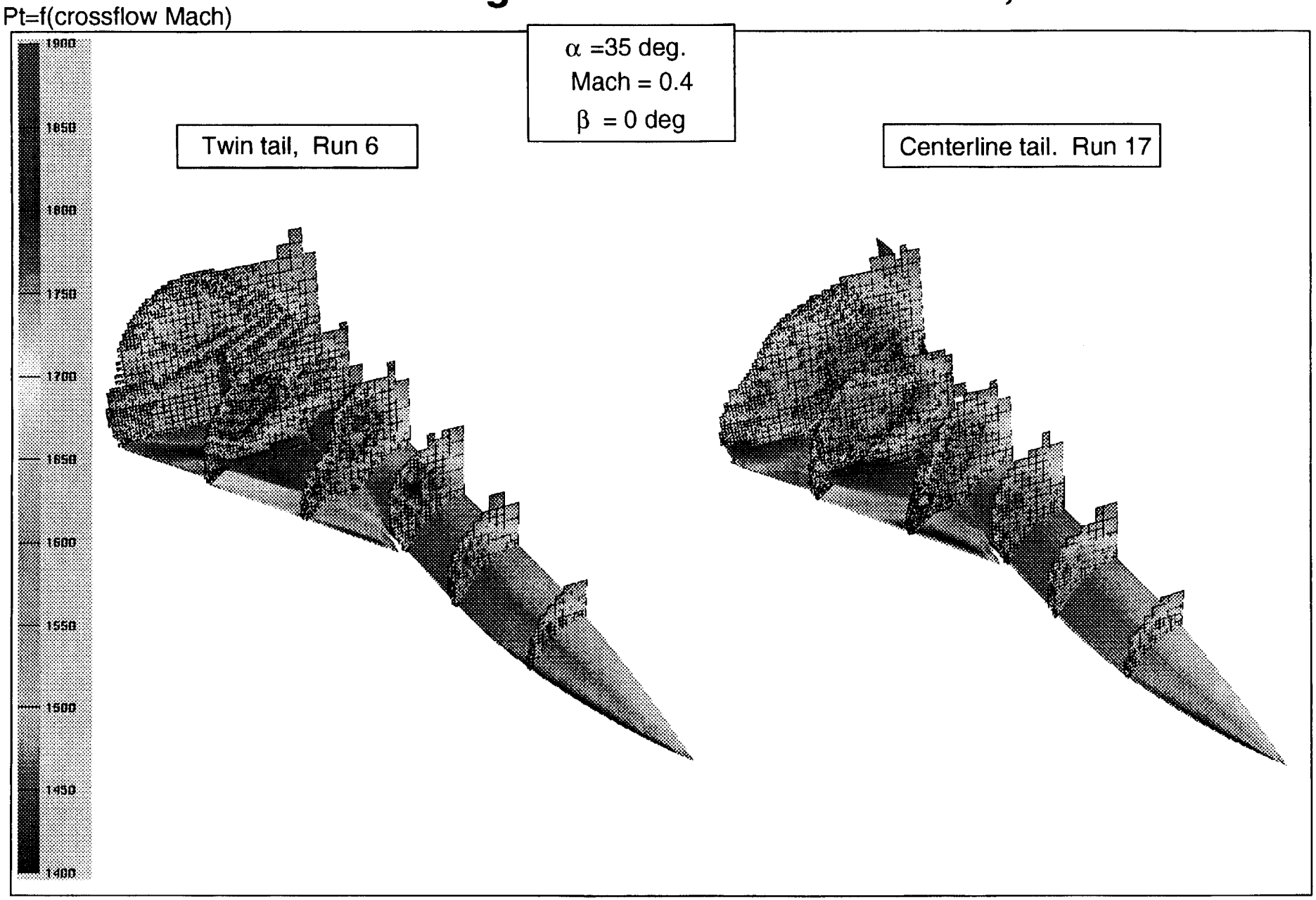

Figure 5.13. Effect of Tail Arrangement on Flowfield, Aoa=35

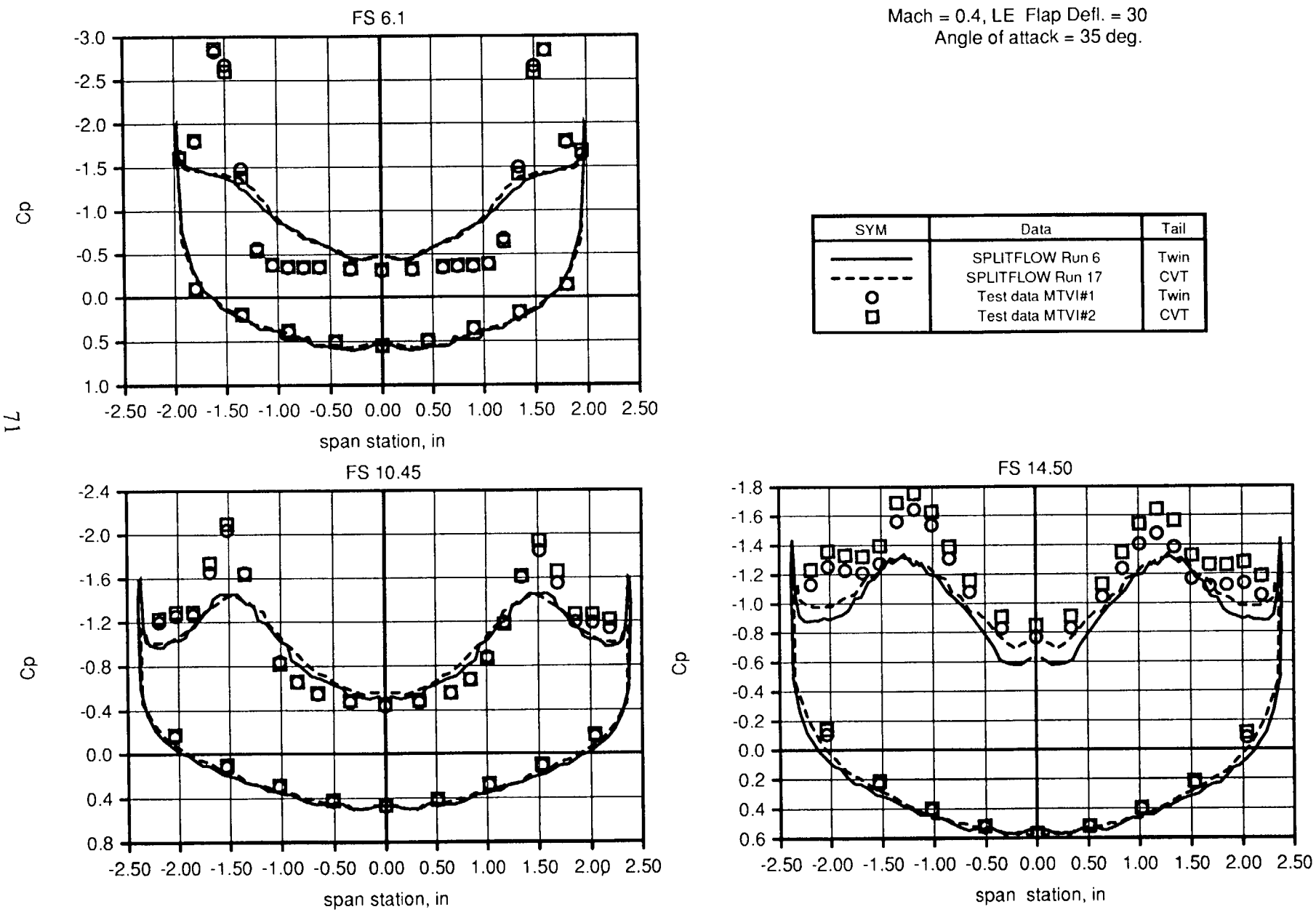

Figure 5.14. Forebody Pressures for Tail Placement, Aoa=35

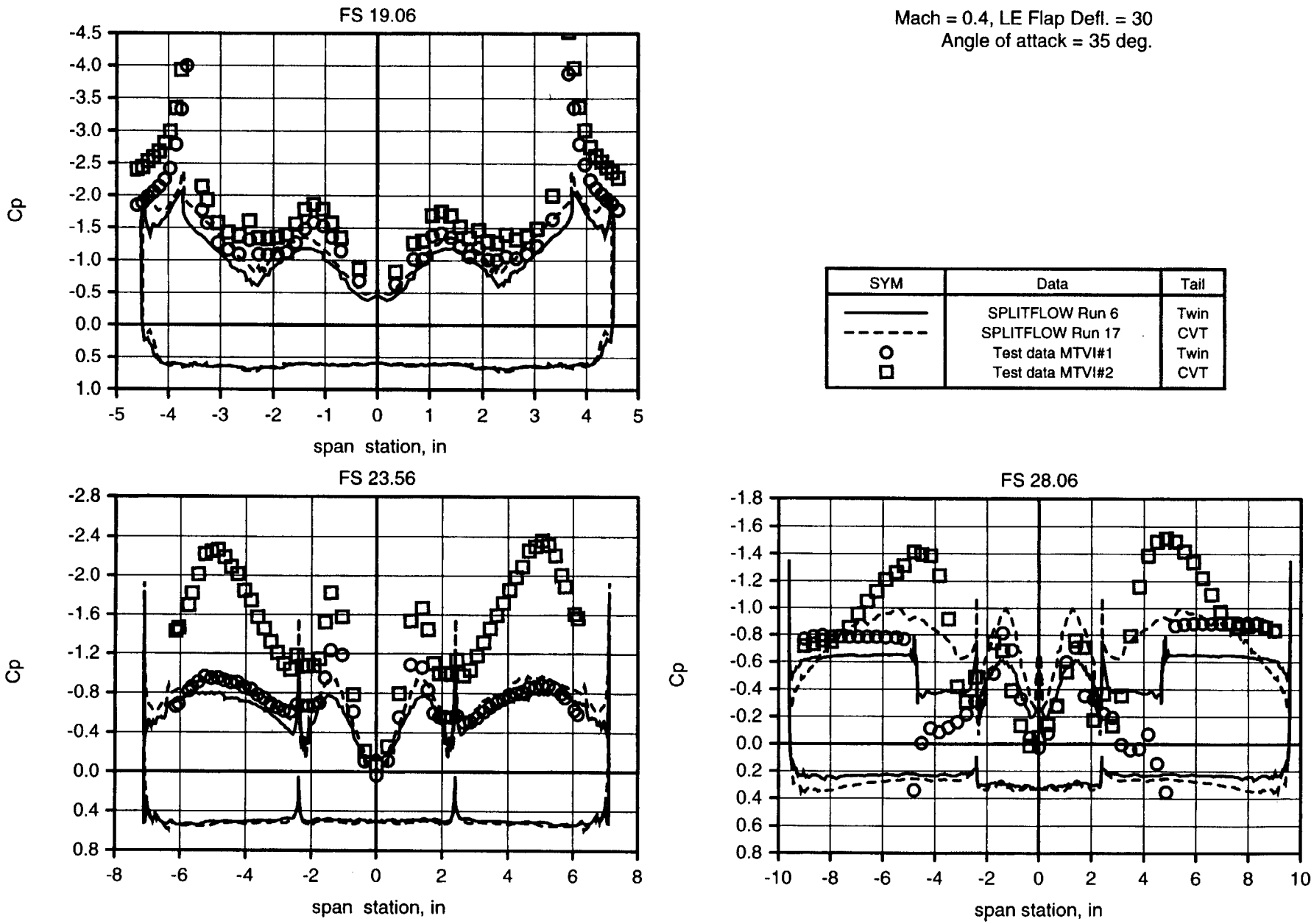

Figure 5.15. Wing Pressures for Tail Placement, Aoa=35

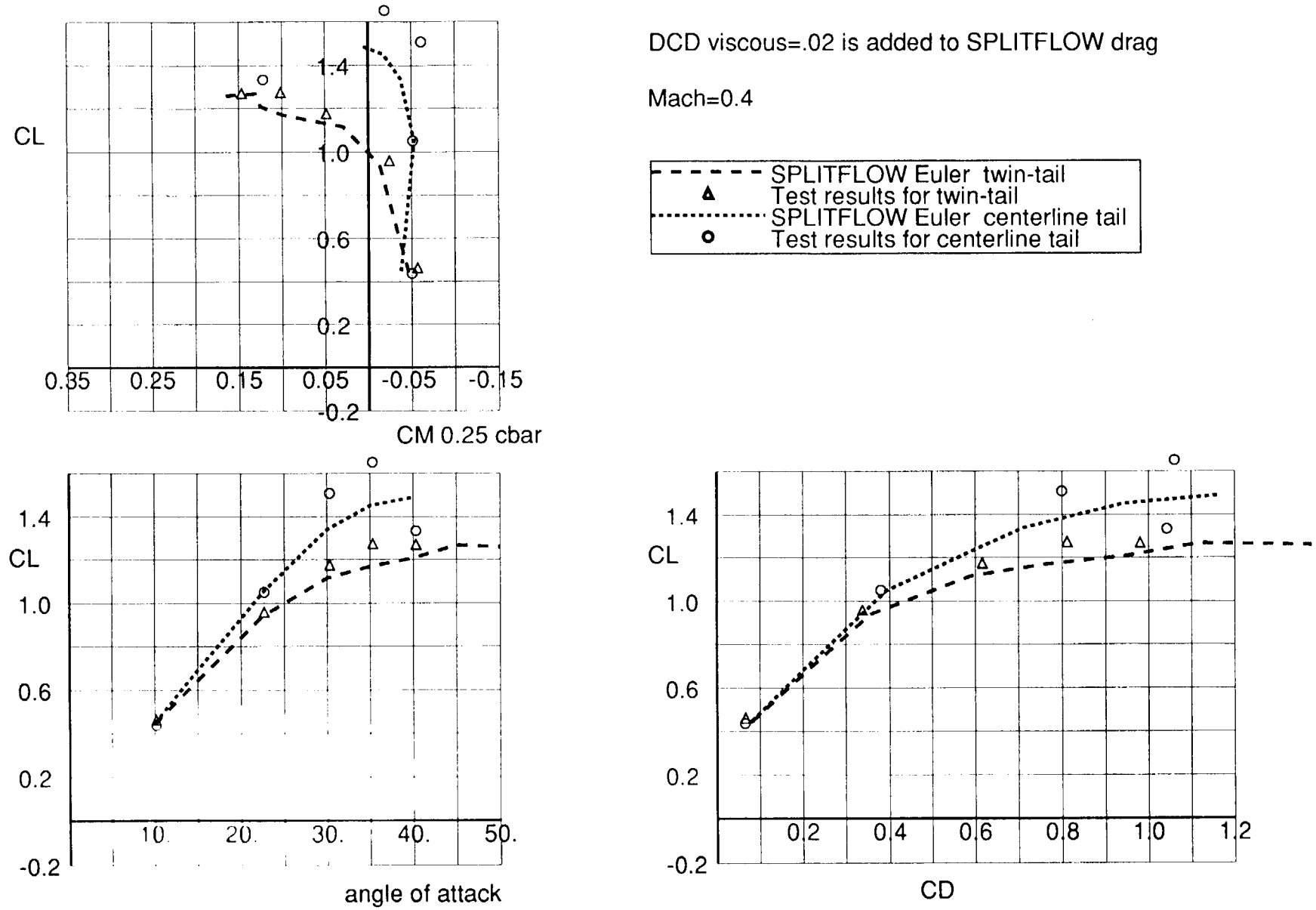

Figure 5.16. Aerodynamic Coefficients vs Test data for MTVI#2

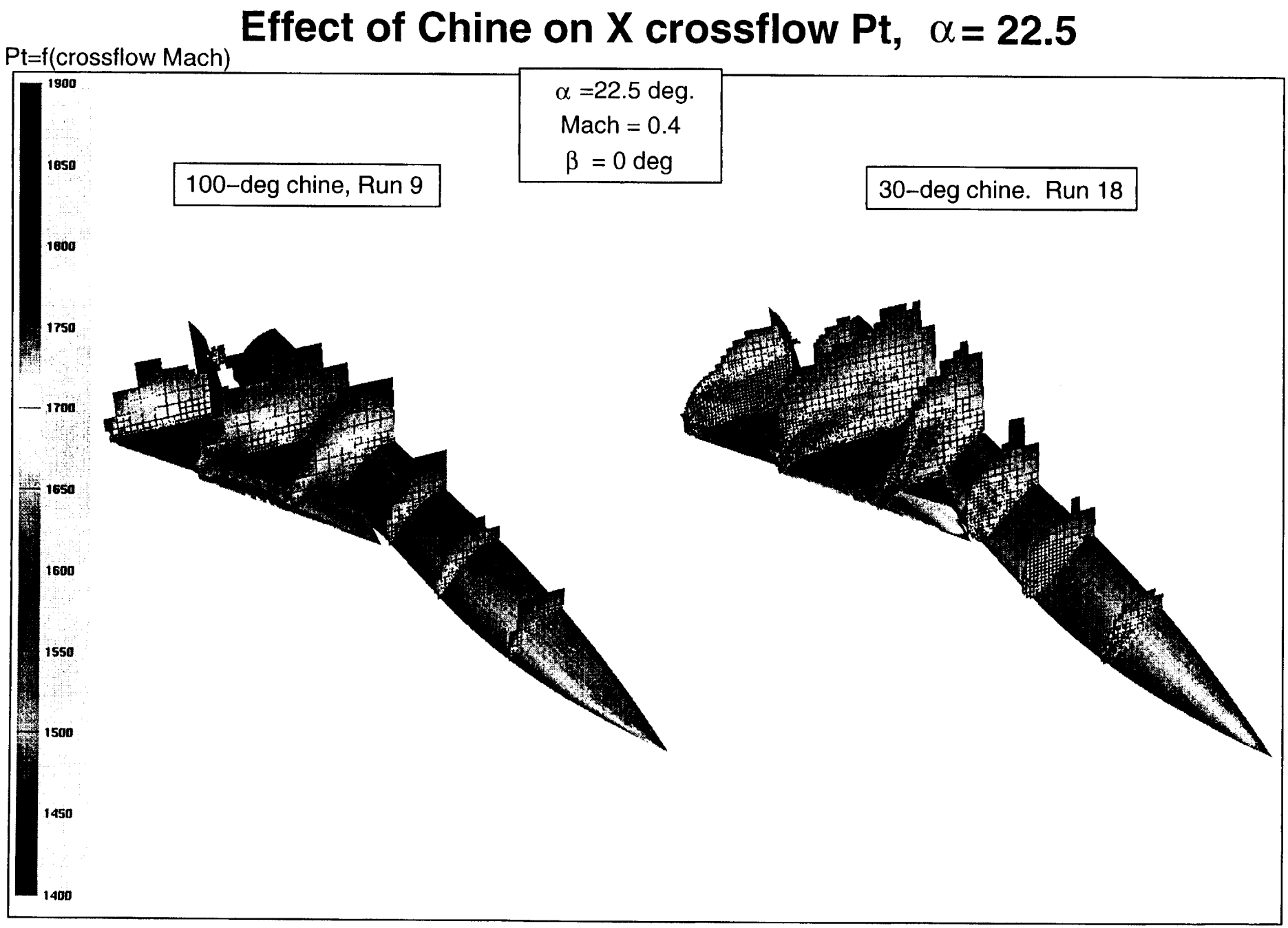

Figure 5.17. Effect of Chine on X-Crossflow Total Pressure, Aoa=22.5

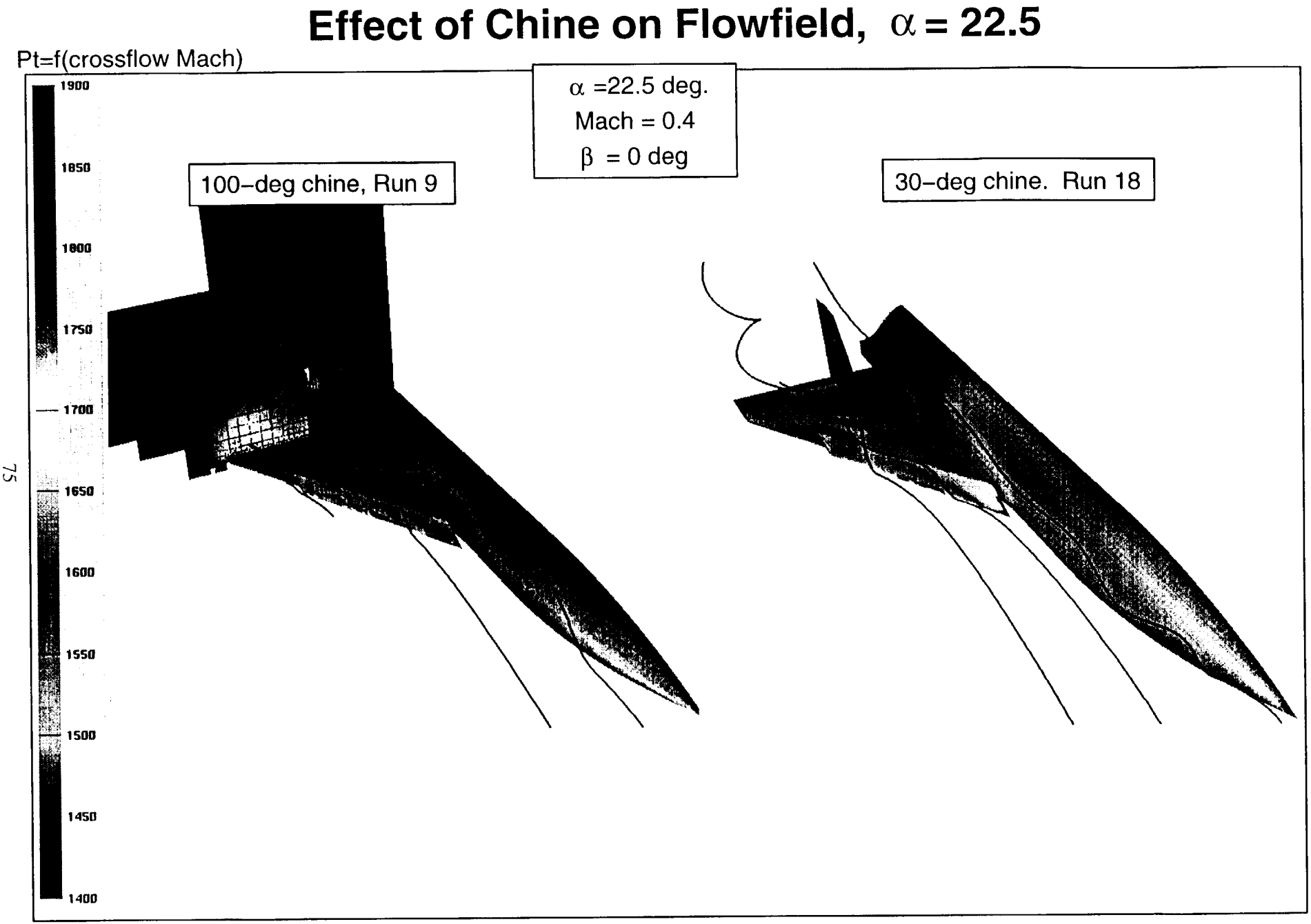

Figure 5.18. Effect of Chine on Flowfield, Aoa=22.5

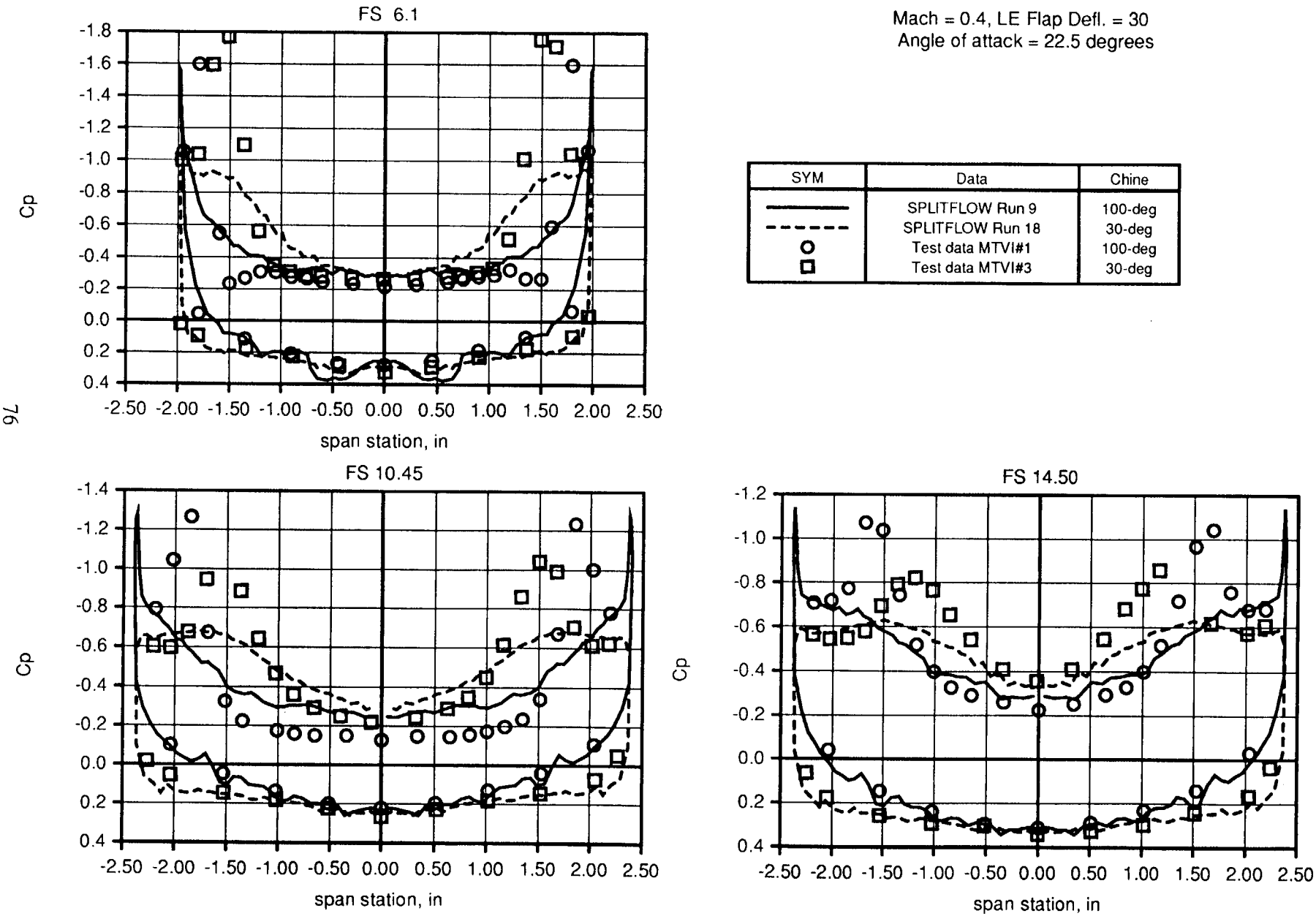

Figure 5.19. Forebody Pressures for Chine Shaping, Aoa=22.5

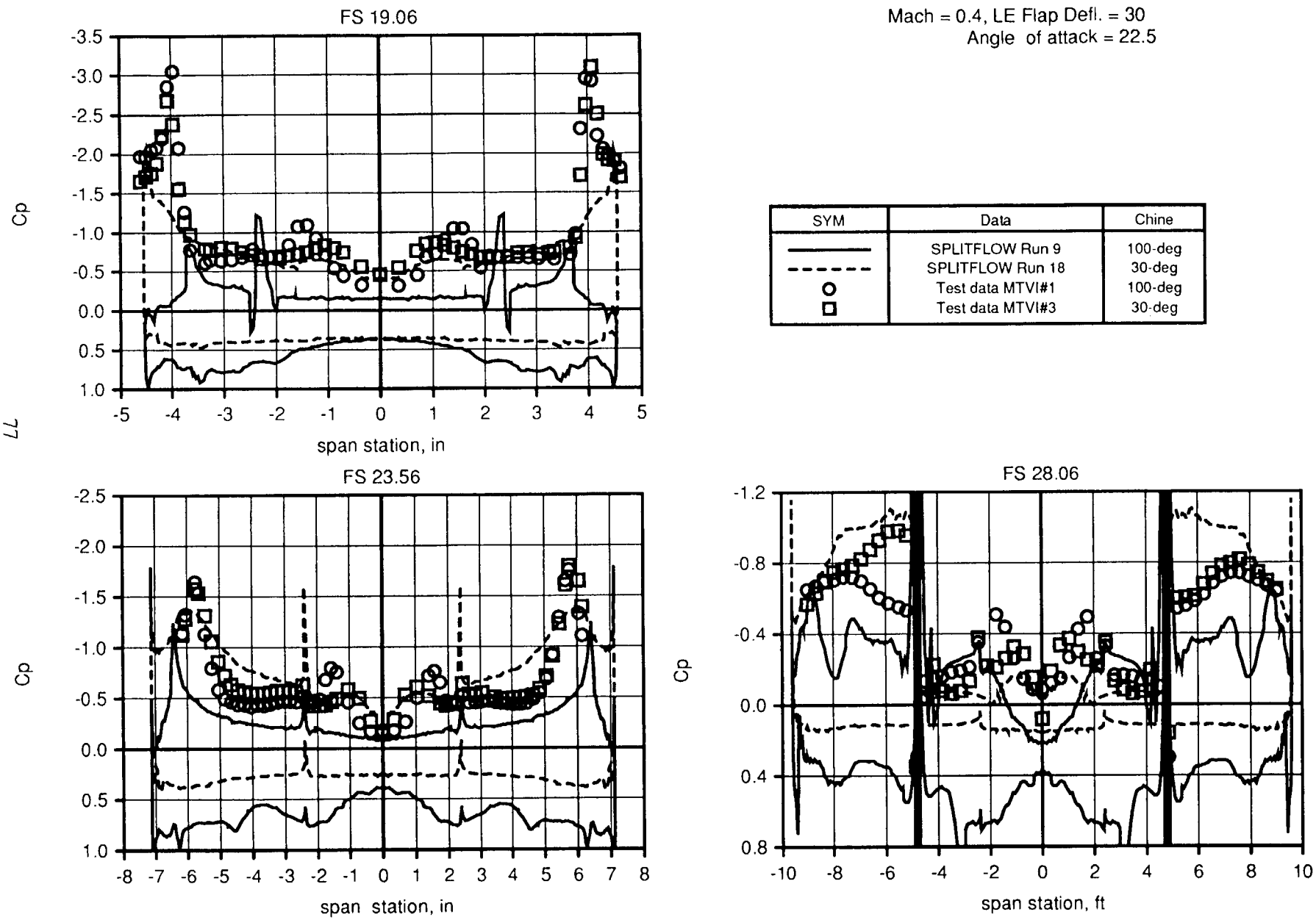

Figure 5.20. Wing Pressures for Chine Shaping, Aoa=22.5

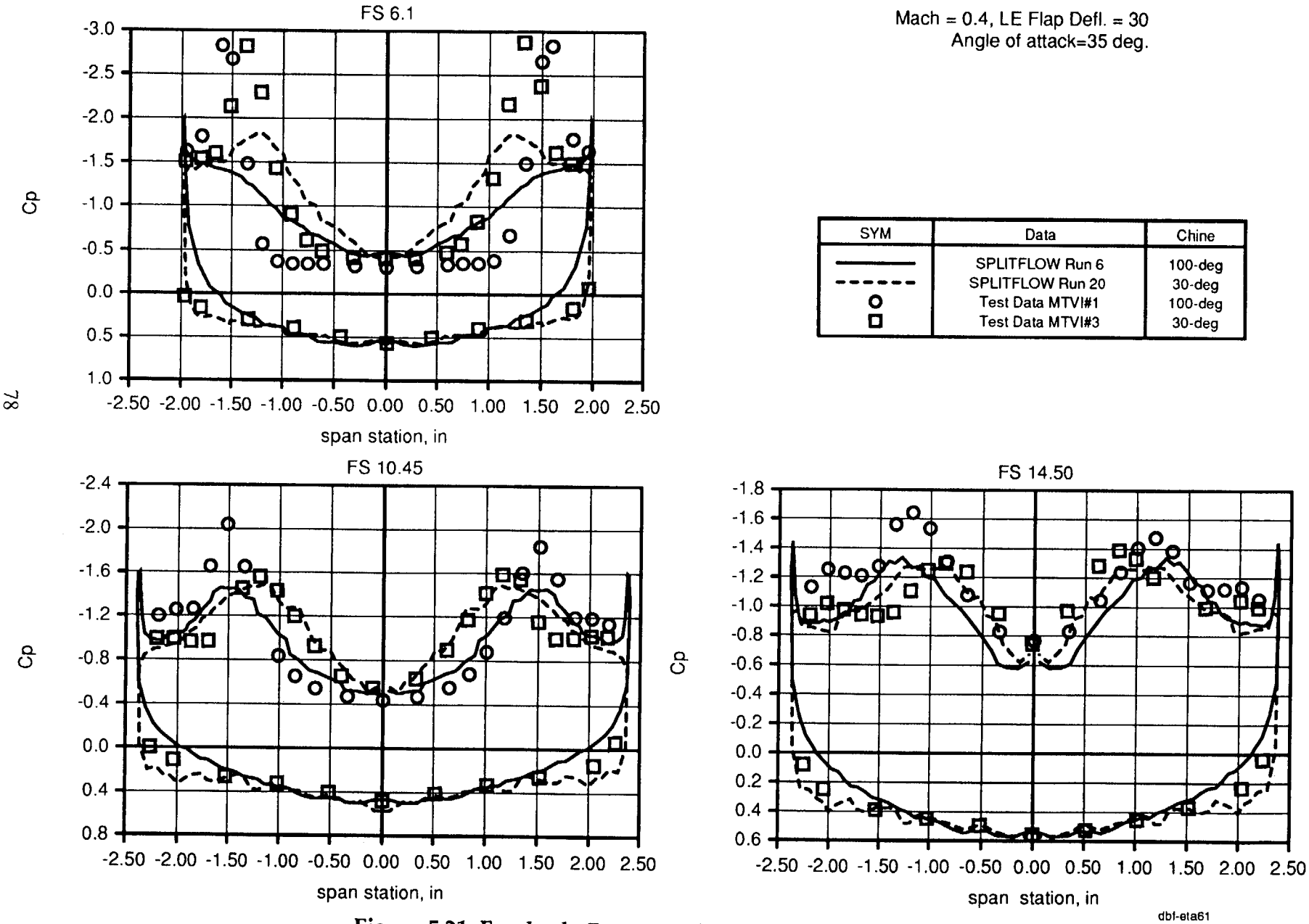

Figure 5.21. Forebody Pressures for Chine Shaping, Aoa=35

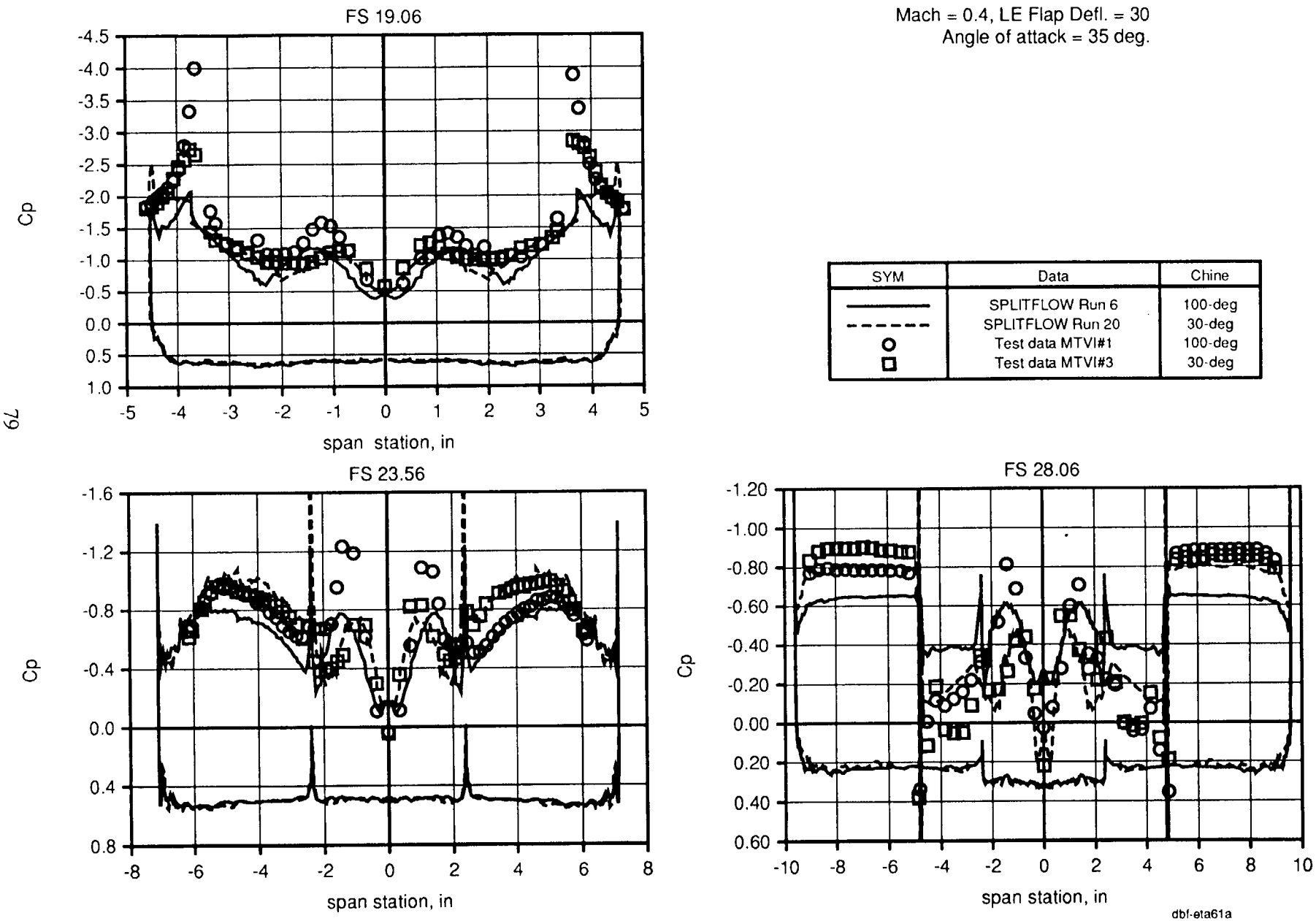

Figure 5.22. Wing Pressures for Chine Shaping, Aoa=35

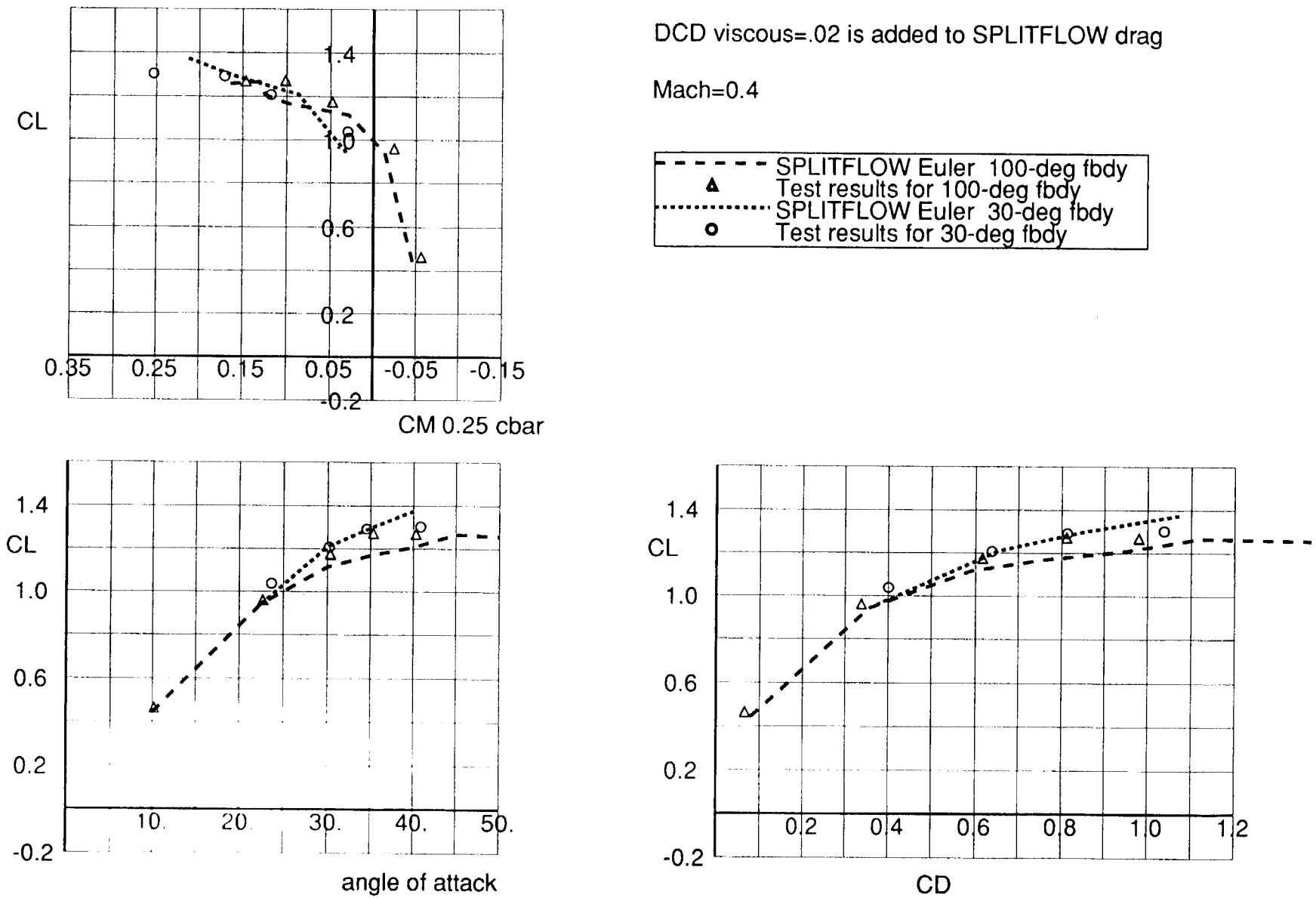

Figure 5.23. Aerodynamic Coefficients vs Test data for Sharp 30-Degree Chine

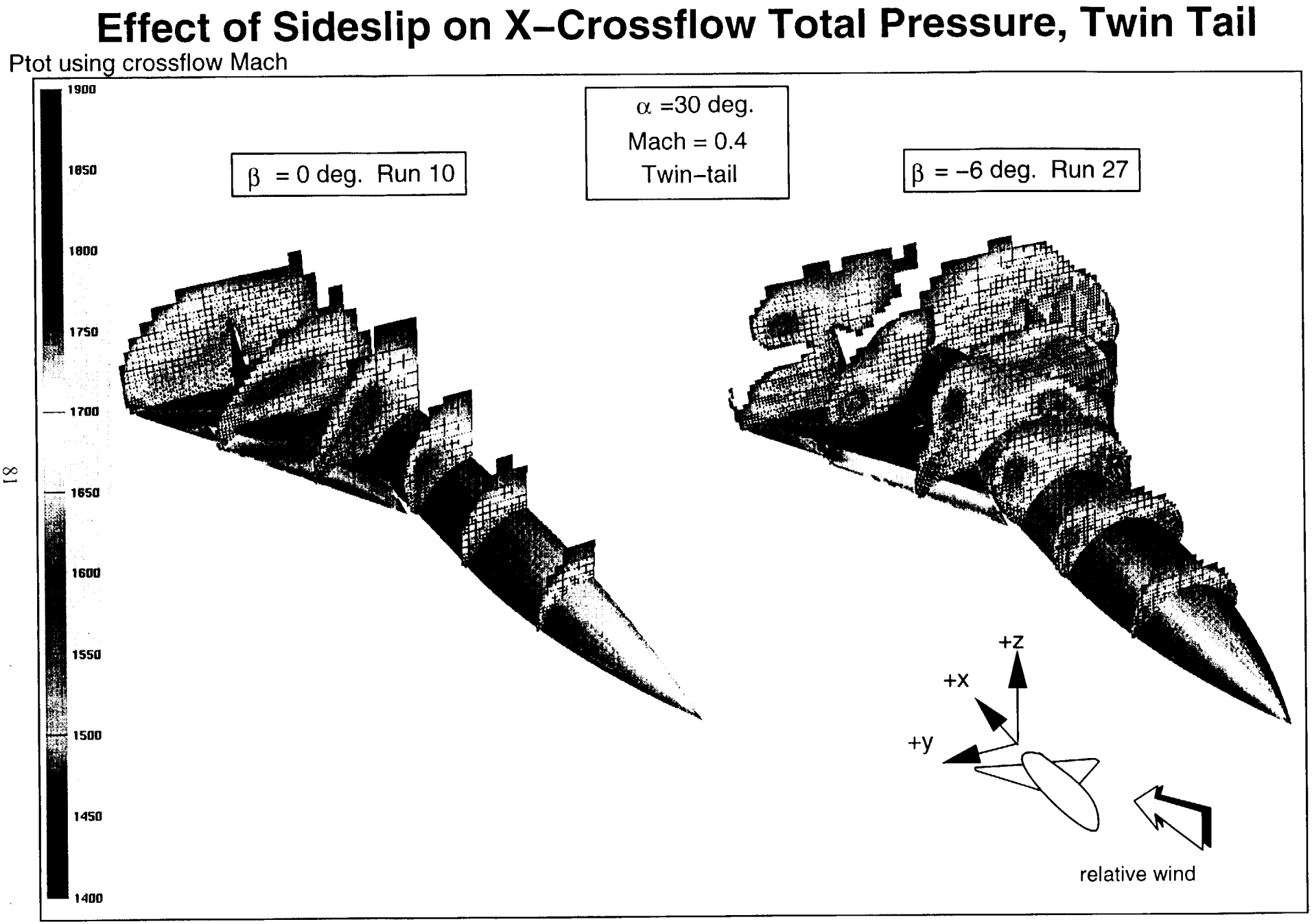

Figure 5.24. Effect of Sideslip on X-Crossflow Total Pressure, Twin Tail

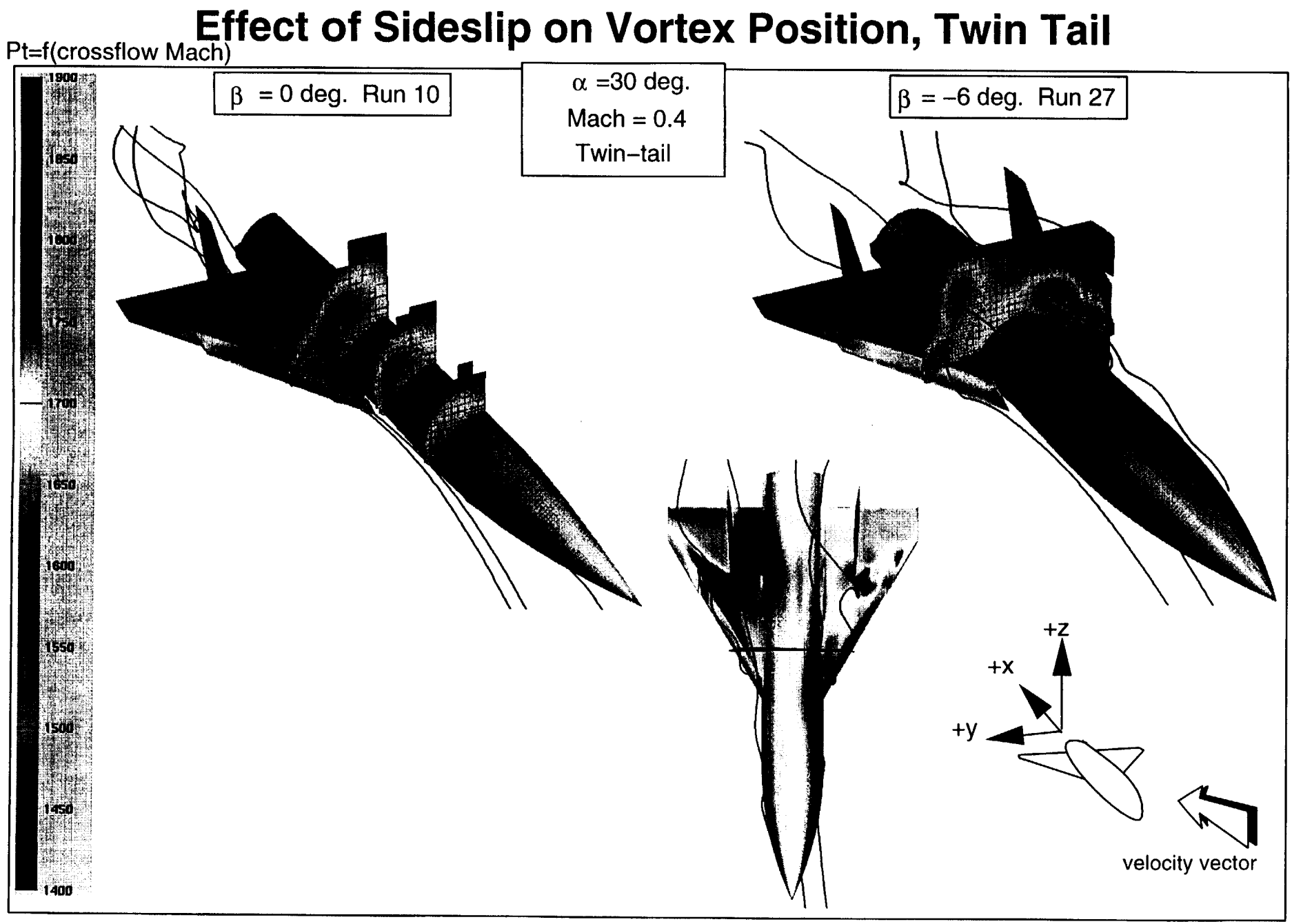

Figure 5.25. Effect of Sideslip on Vortex Position, Twin Tail

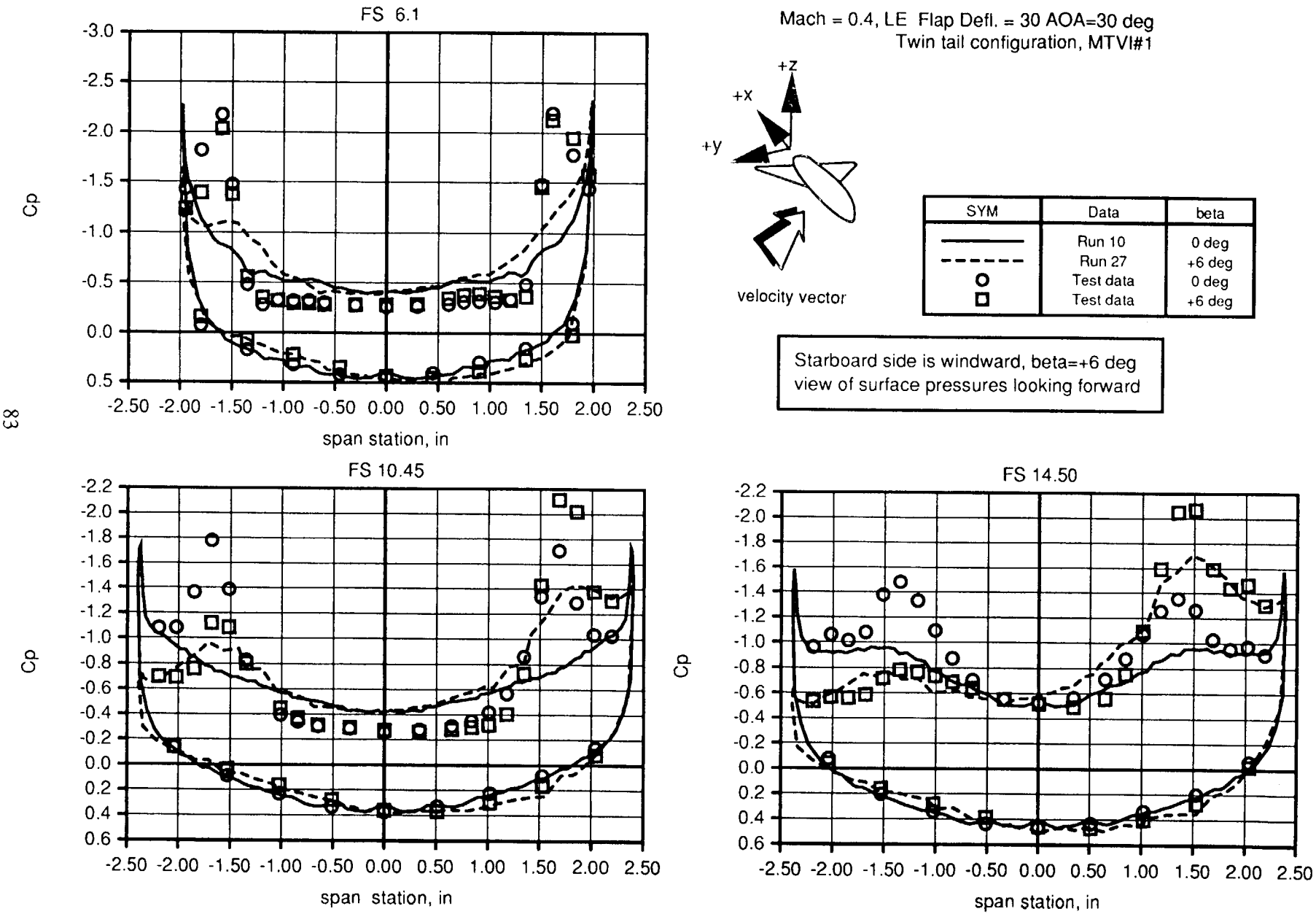

Figure 5.26. Forebody Pressures for Twin Tail in Sideslip

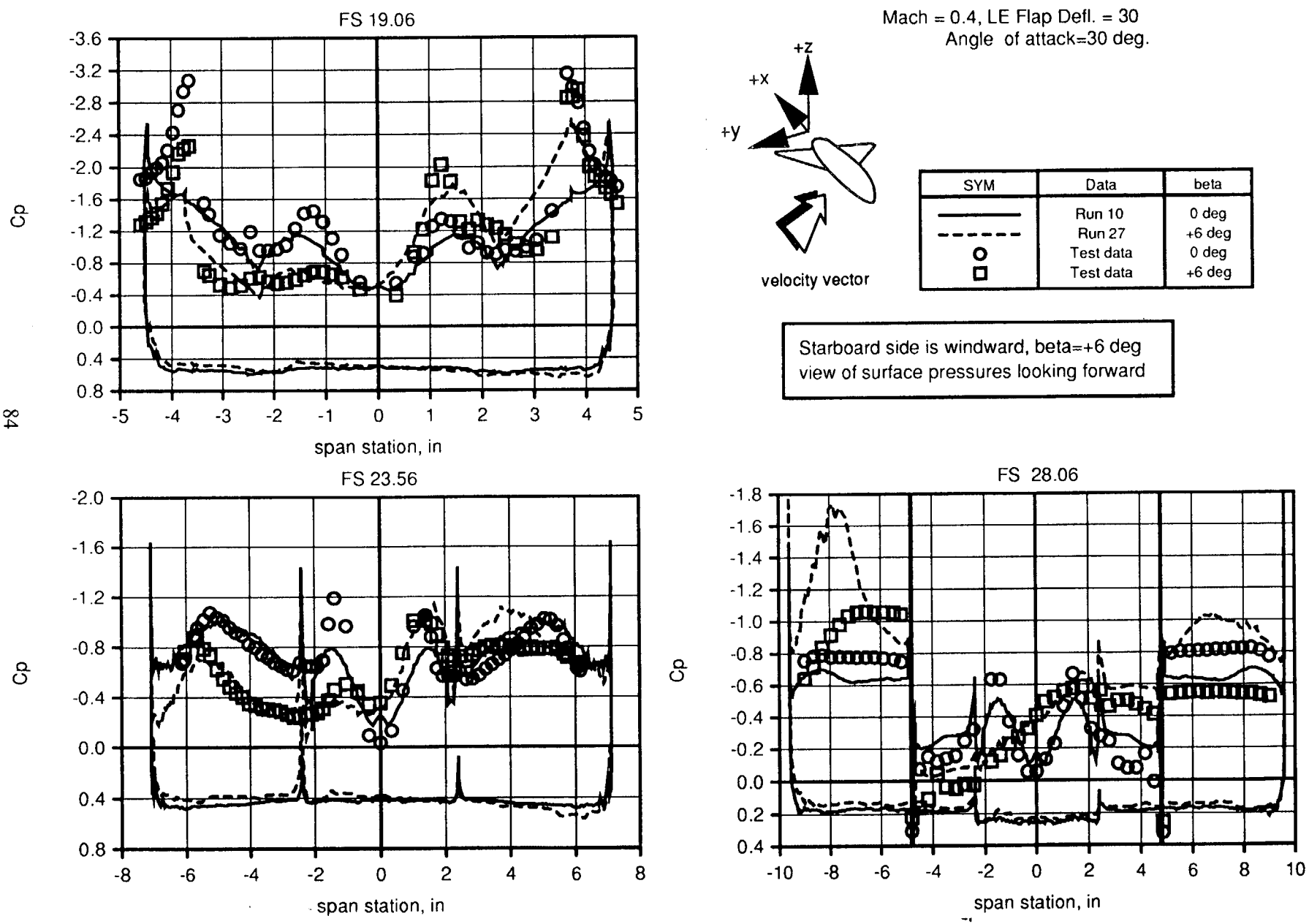

Figure 5.27. Wing Pressures for Twin Tail in Sideslip

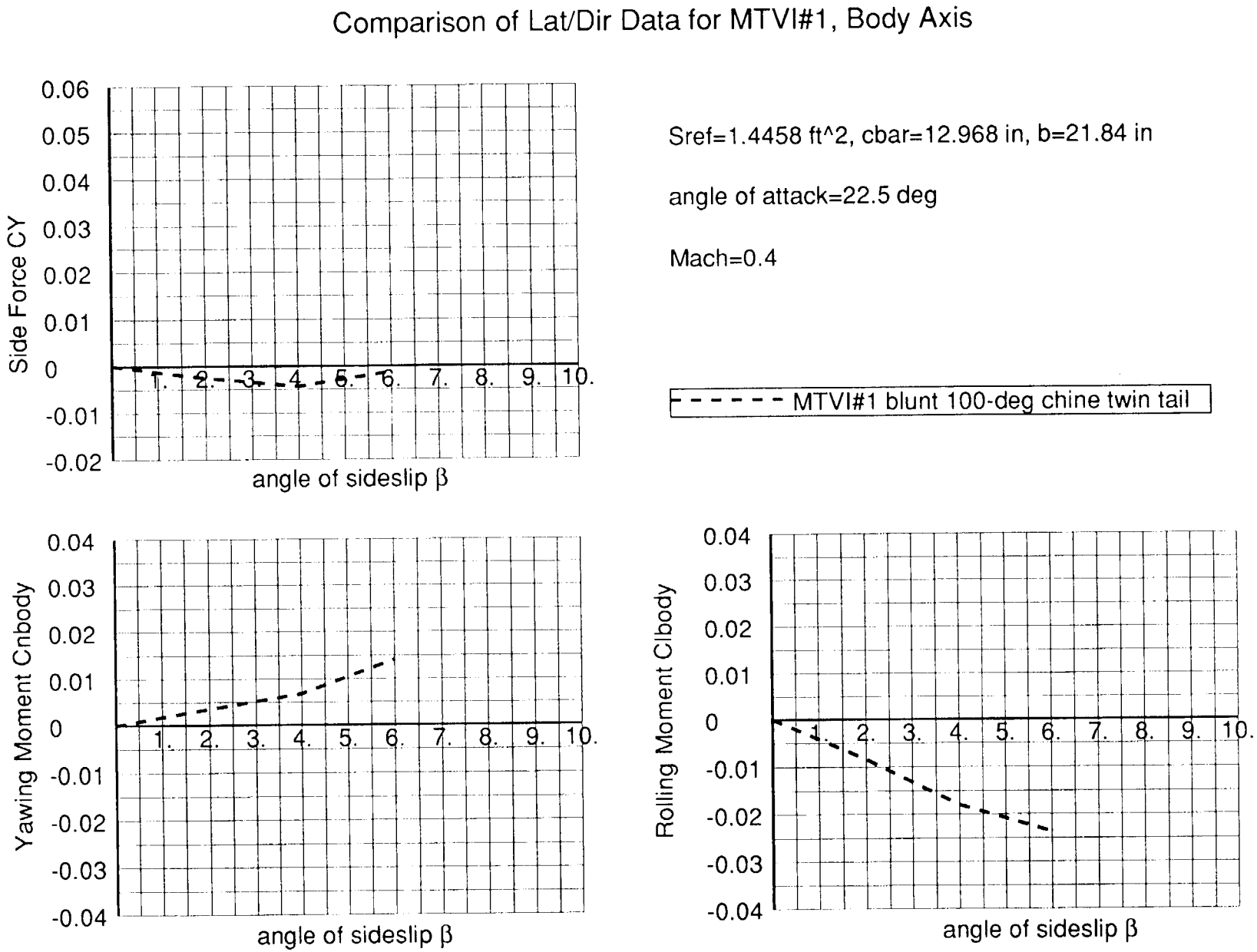

Figure 5.28. Comparison of Lateral/Directional Data for Twin Tail, Aoa=22.5

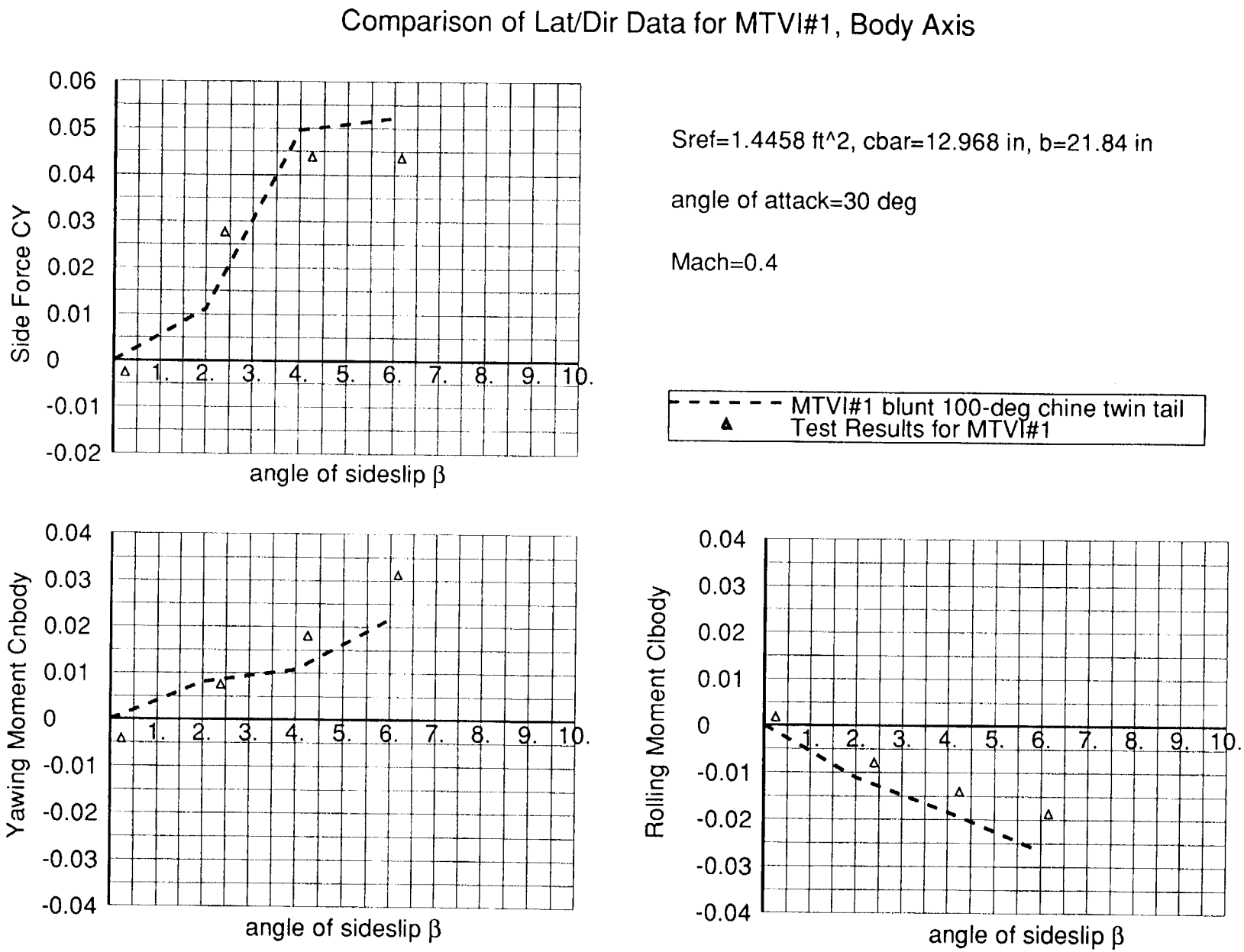

Figure 5.29. Comparison of Lateral/Directional Data for Twin Tail, Aoa=30

Effect of Sideslip on X–Crossflow Total Pressure, Centerline Tail

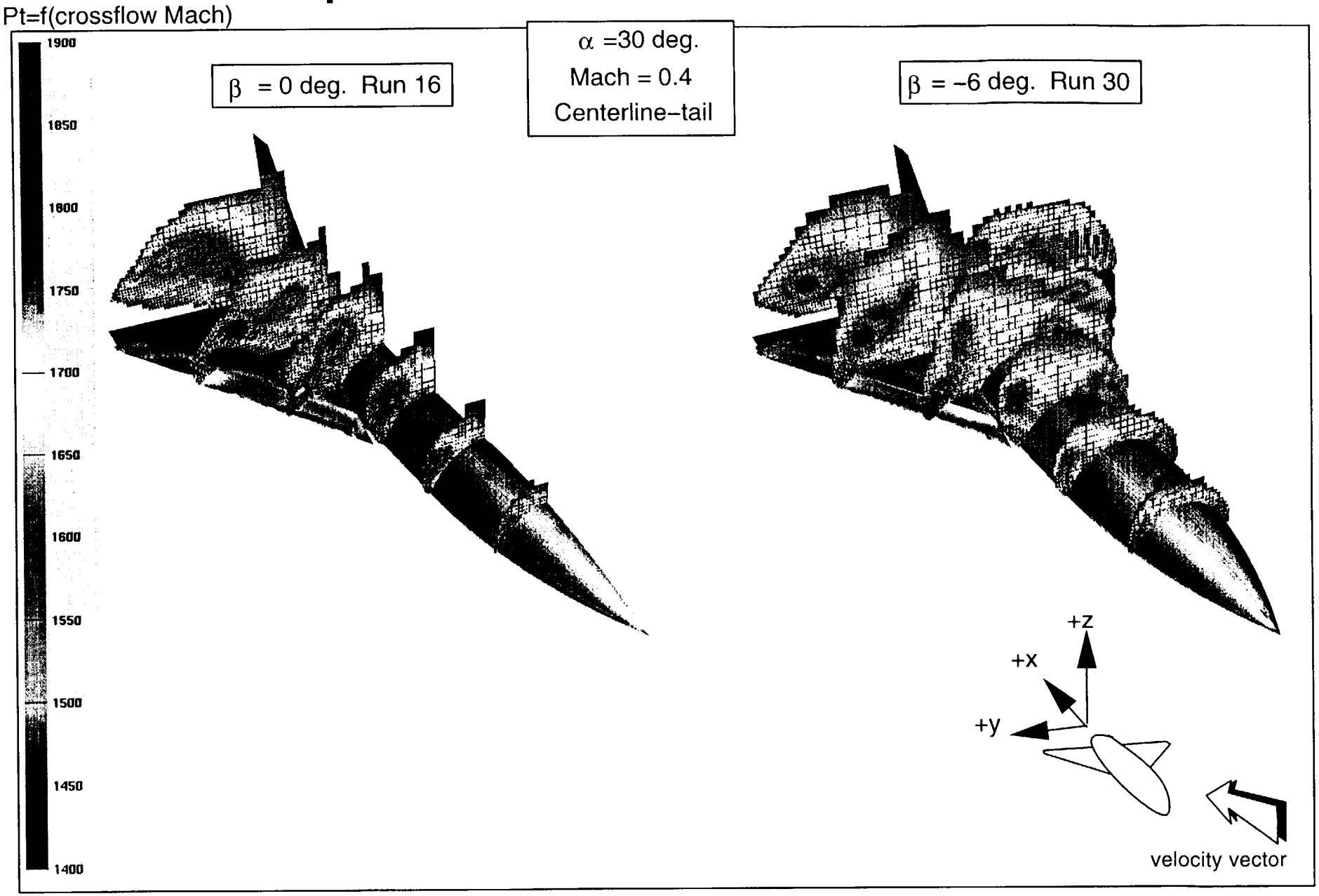

Figure 5.30. Effect of Sideslip on X-Crossflow Total Pressure, Centerline Tail

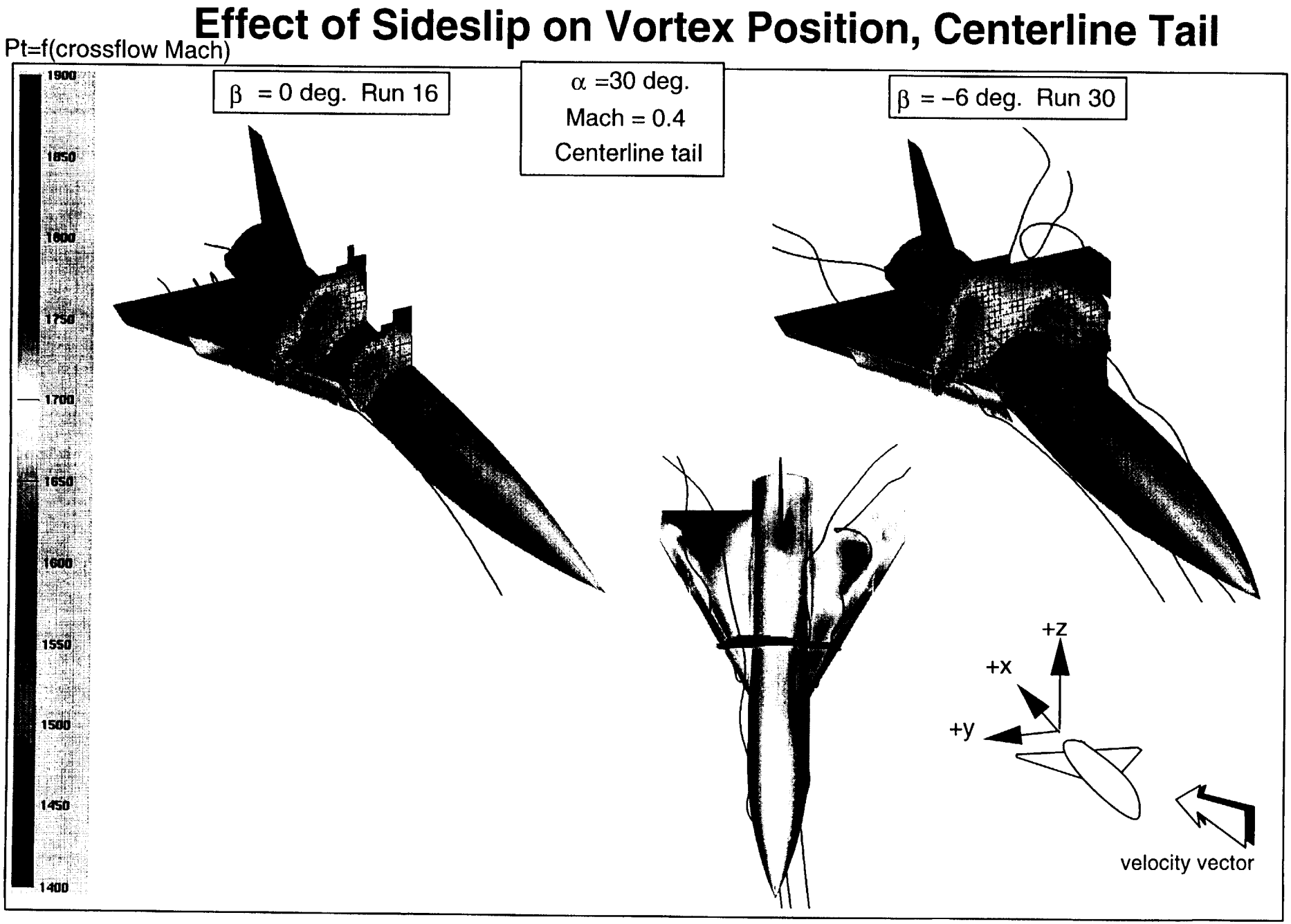

Figure 5.31. Effect of Sideslip on Vortex Position, Centerline Tail

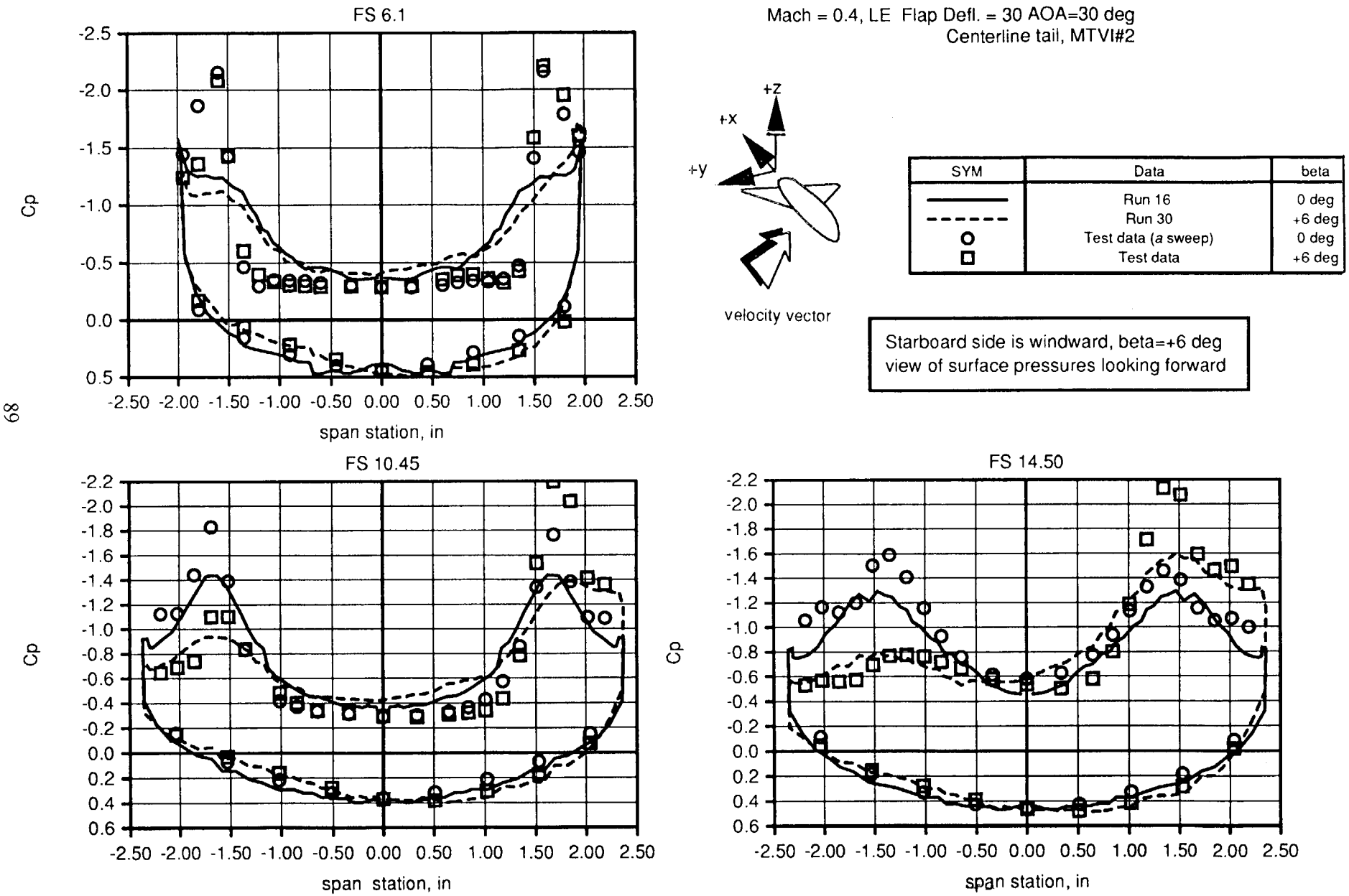

Figure 5.32. Forebody Pressures for Centerline Tail in Sideslip

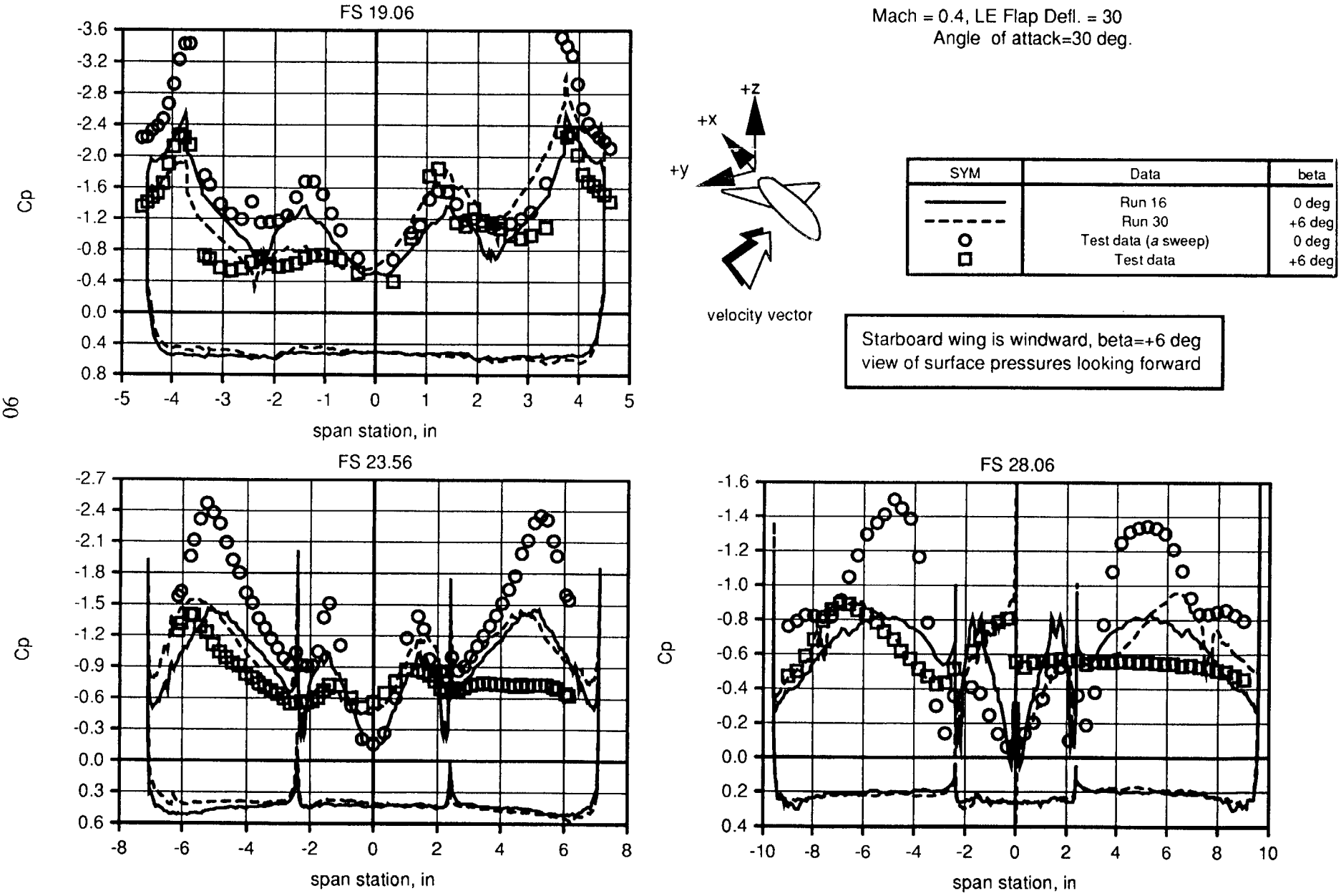

Figure 5.33. Wing Pressures for Centerline Tail in Sideslip

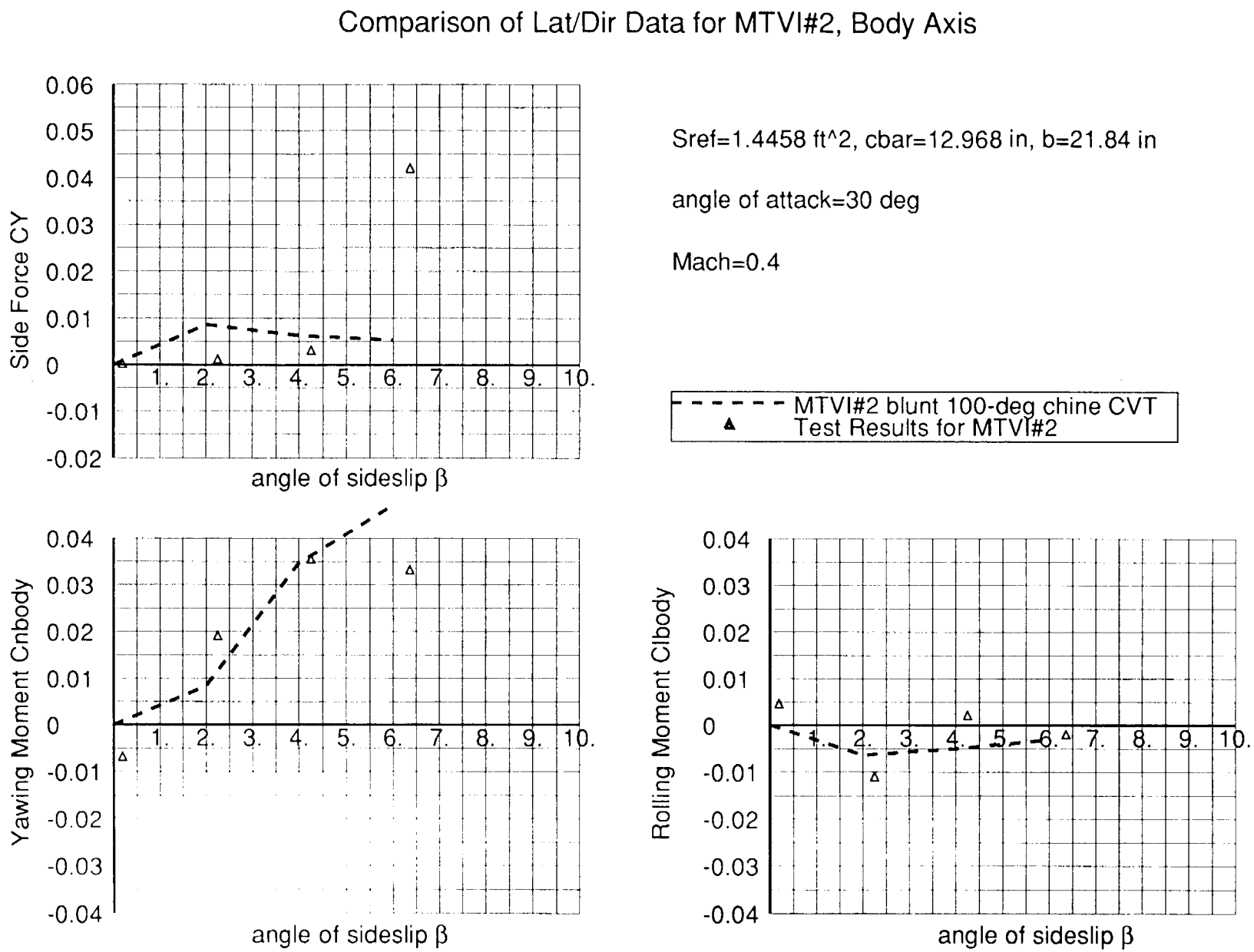

Figure 5.34. Comparison of Lateral/Directional Data for Centerline Tail, Aoa=30

C-2.

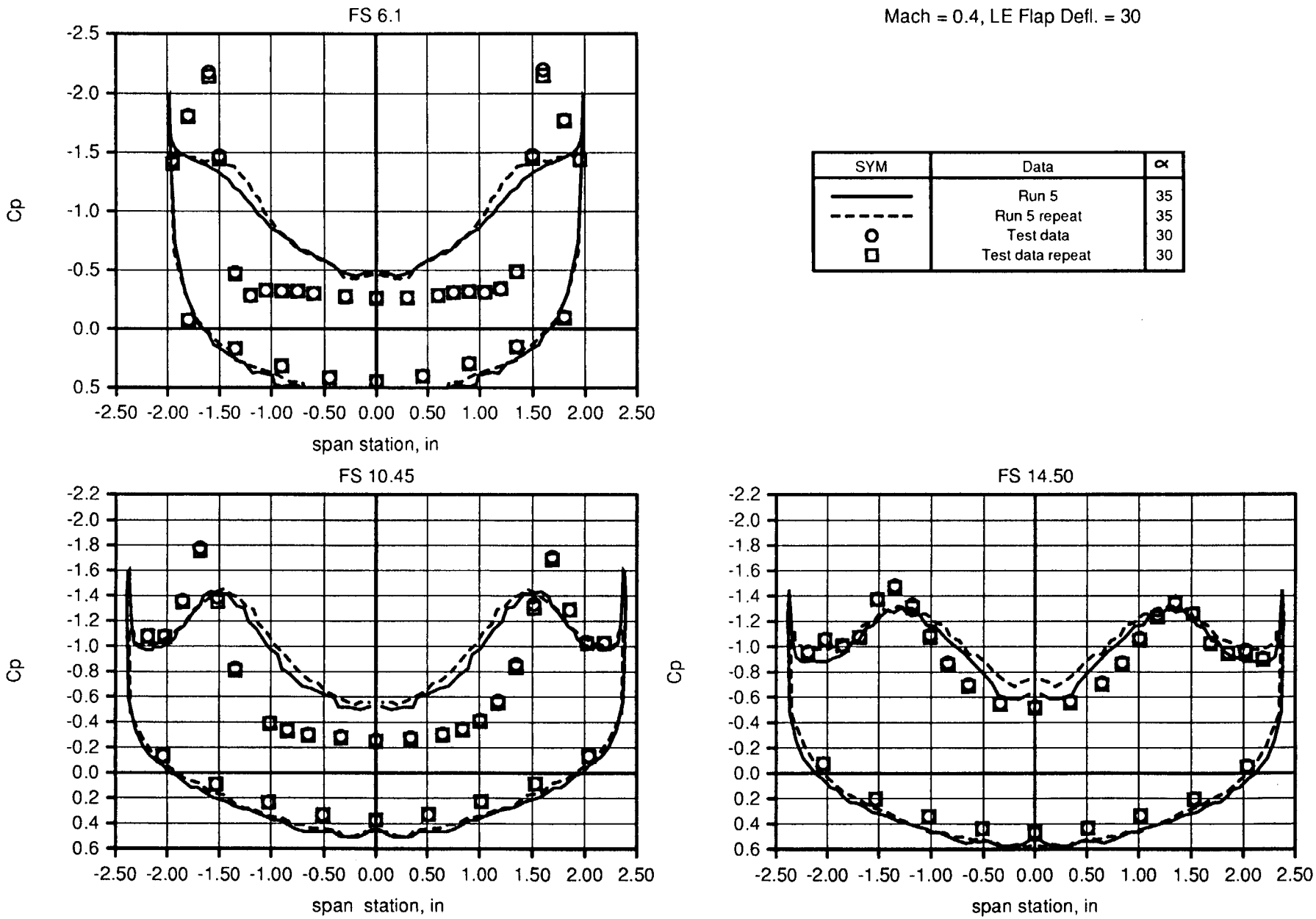

Figure 5.35. Uncertainty in Surface Pressures for Test and CFD

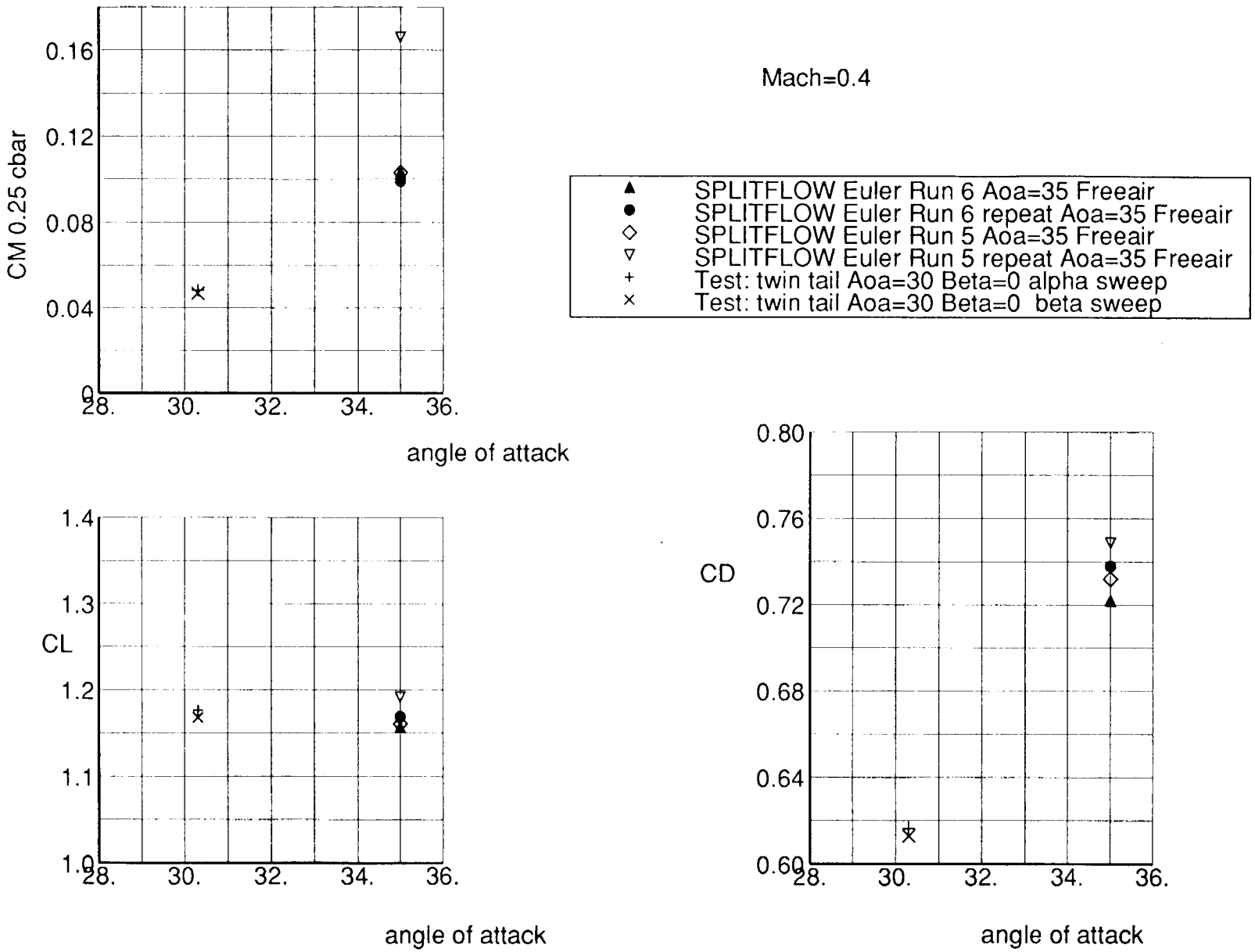

Figure 5.36. Uncertainty in Forces for Test and CFD

REPORT DOCUMENTATION PAGE

Form Approved
OMB No. 0704-0188

Public reporting burden for this collection of information is estimated to average 1 hour per response, including the time for reviewing instructions, searching existing data sources, gathering and maintaining the data needed, and completing and reviewing the collection of information. Send comments regarding this burden estimate or any other aspect of this collection of information, including suggestions for reducing this burden, to Washington Headquarters Services, Directorate for Information Operations and Reports, 1215 Jefferson Davis Highway, Suite 1204, Arlington, VA 22202-4302, and to the Office of Management and Budget, Paperwork Reduction Project (0704-0188), Washington, DC 20503.

1. AGENCY USE ONLY *(Leave blank)*

2. REPORT DATE
March 1995

3. REPORT TYPE AND DATES COVERED
Contractor Report (2/1/94 to 8/1/94)

4. TITLE AND SUBTITLE
Euler Technology Assessment Program for Preliminary Aircraft Design Employing SPLITFLOW Code with Cartesian Unstructured Grid Method

5. FUNDING NUMBERS
C NAS1-19000, Task T017

WU 505-68-30-03

6. AUTHOR(S)
Dennis B. Finley

7. PERFORMING ORGANIZATION NAME(S) AND ADDRESS(ES)
Lockheed Fort Worth Company
Fort Worth, TX 76101

8. PERFORMING ORGANIZATION REPORT NUMBER

9. SPONSORING/MONITORING AGENCY NAME(S) AND ADDRESS(ES)
National Aeronautics and Space Administration
Langley Research Center
Hampton, VA 23681-0001

10. SPONSORING/MONITORING AGENCY REPORT NUMBER
NASA CR-4649

11. SUPPLEMENTARY NOTES
Technical Monitor: Mr. Farhad Ghaffari
NASA Langley Research Center
Hampton VA 23681-0001

12a. DISTRIBUTION/AVAILABILITY STATEMENT
Unclassified-Unlimited
Subject Category 02

12b. DISTRIBUTION CODE

13. ABSTRACT *(Maximum 200 words)*

This report documents results from the Euler Technology Assessment program. The objective was to evaluate the efficacy of Euler Computational Fluid Dynamics (CFD) codes for use in preliminary aircraft design. Both the accuracy of the predictions and the rapidity of calculations were to be assessed. This portion of the study was conducted by Lockheed Fort Worth Company, using a recently developed in-house Cartesian-grid code called SPLITFLOW. The Cartesian grid technique offers several advantages for this study, including ease of volume grid generation and reduced number of cells compared to other grid schemes. SPLITFLOW also includes grid adaption of the volume grid during the solution convergence to resolve high-gradient flow regions. This proved beneficial in resolving the large vortical structures in the flow for several configurations examined in the present study. The SPLITFLOW code predictions of the configuration forces and moments are shown to be adequate for preliminary design analysis, including predictions of sideslip effects and the effects of geometry variations at low and high angles of attack. The time required to generate the results from initial surface definition is on the order of several hours, including grid generation, which is compatible with the needs of the design environment.

14. SUBJECT TERMS
Computational Fluid Dynamics, Euler formulation, Preliminary aircraft design, Sharp-edge flow separation, Vortex flow, Vortex burst, Sideslip angle, SPLITFLOW

15. NUMBER OF PAGES
100

16. PRICE CODE
A05

17. SECURITY CLASSIFICATION OF REPORT
Unclassified

18. SECURITY CLASSIFICATION OF THIS PAGE
Unclassified

19. SECURITY CLASSIFICATION OF ABSTRACT
Unclassified

20. LIMITATION OF ABSTRACT